Ca' Foscari University of Venice

Department of Molecular Sciences and Nanosystems

Science and Technology of Bio and Nanomaterials

Master Thesis

New Alkaline-based Fluoride Host Materials for Luminescent Transition Metal and Lanthanide Ions

Emily Andreato

Supervisor:
Prof. Canton Patrizia,
Ca' Foscari University of Venice

Co-supervisor:
Prof. Riccardo Marin,
Autonomous University of Madrid

Academic year 2022/2023

Ca' Foscari University of Venice

Department of Molecular Sciences and Nanosystems

Science and Technology of Bio and Nanomaterials

Master Thesis

New Alkaline-based Fluoride Host Materials for Luminescent Transition Metal and Lanthanide Ions

Emily Andreato

Supervisor:
Prof. Canton Patrizia,
Ca' Foscari University of Venice

Co-supervisor:
Prof. Riccardo Marin,
Autonomous University of Madrid

Academic year 2022/2023

Acknowledgements

I would like to devote this space to those who, with dedication and patience, made this work possible.
I would like to acknowledge my supervisor Prof. Canton who in these months of work, with her guidance, support and experience enabled me to broaden my perspectives and knowledge. I would also like to acknowledge my co-supervisor Dr. Marin for his infinite availability and promptness to all my requests. A sincere thank you for making me even more passionate about the world of research. I thank them both for their indispensable advice and suggestions during the writing of this final thesis. I thank all the people of Nanomaterials for Bioimaging Group (NanoBIG), where I carried out the internship complementary to the writing of the thesis, for their warm welcome and help.
I can not mention two people, my mother and my sister, who have always supported me in the realisation of my projects. I will never stop thanking you for letting me get here and making me the woman I am today. I thank my boyfriend for his infinite patience and for always believing in me. Thank you for always being there especially in moments of discouragement and for making my life full of love. Thanks also to my grandparents, those who are here and those who can not be here to rejoice with me. I thank my colleague Anna who shared joys and difficulties with me in the months spent together in Spain. Thank you for making this path special. Thanks also to my friends and fellow students for listening to my outbursts, thanks for all the carefree moments. Thanks to all the people who have dedicated time and kind words to me over the years.

Abstract

The past decades have witnessed an increased interest in luminescent nanomaterials because of their broad application prospects, among which luminescence sensing. From this perspective, luminescent nanomaterials made of wide band-gap inorganic materials doped with lanthanide and transition metal ions offer unique advantages, including high sensitivity and physicochemical stability. The optical properties of these two types of ions differ considerably, making them suitable for different sensing purposes. Lanthanide ions have narrow emission lines whose energy is minimally affected by the host material, while transition metal ions feature broader emission bands whose energy depends on the crystalline environment. A luminescent nanomaterial containing both types of ions would feature novel, exciting optical properties. However, the preparation of such a nanomaterial is not trivial, because of differences in ionic radius and favoured coordination number.

Herein, a strategy for achieving these nanomaterials is reported. A synthesis protocol was developed, which affords alkaline-based fluoride nanoparticles that can be doped with lanthanide and transition metal ions. A thorough optimization of the synthesis parameter was performed, varying reaction time, temperature, and concentration of chemical precursors. The obtained oleate-capped nanocrystals are readily dispersible in non-polar solvents and, when doped with Nd(III) and/or Cr(III) show the typical emission of these ions.

Contents

Introduction

1.1 Luminescence in Solids

The term "luminescenz" (luminescence) was coined by German physicist Eilhard Wiedemann in 1888 for all phenomena of light that were not solely conditioned by the rise in temperature - that is, incandescence. However, luminescent phenomena have fascinated mankind since antiquity, just think of glow worms, the Aurora Borealis, Bologna stone, as examples.[1]

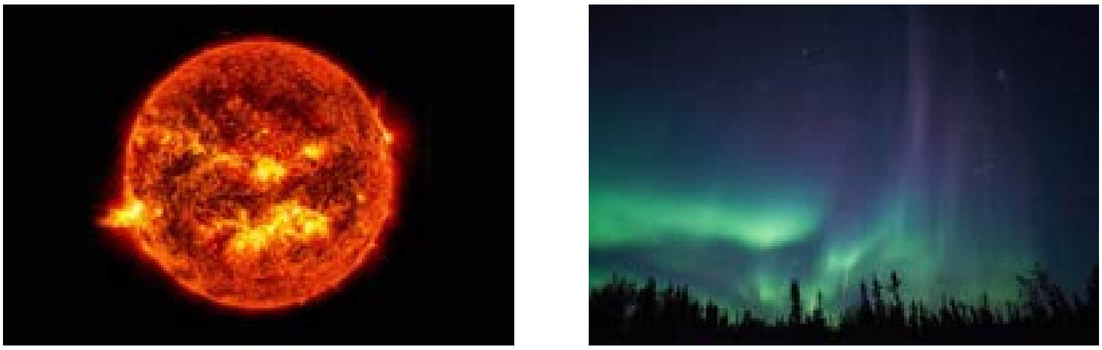

(a) Solar flare on the left side of the Sun, incandescence.

(b) Aurora borealis in Alaska, luminescence.

Figure 1.1: Two natural examples of light emission by incandescence or luminescence.

Luminescence is an electronic de–excitation phenomenon that results in the spontaneous emission of ultraviolet, visible, and near–infrared photons.

Luminescence is classified into several classes depending on the type of energy used to excite the electronic transitions, such as light (photoluminescence), heat (thermoluminescence), mechanical energy (mechano and triboluminescence). In the case of photoluminescence, the photon's electromagnetic radiation is absorbed by providing the required energy to electrons to move from the ground state to higher energy states.

Since the electronic structure of a material strongly depends on the state of matter, it should be stressed that this thesis is limited to solid–state materials with a particular concern for inorganic nanomaterials. Unlike liquids and gases, the fundamental units of inorganic solids (atoms or ions) are closely packed and periodically arranged

in long–range (crystals) or short–range (amorphous solids) order. Consequently, in a crystal, electrons are subjected to a periodic potential (a perturbation) which originates from the ions in the lattice and from electron–electron interactions.
The behavior of electrons in a crystalline solid can be modelled by using the time –independent Schrödinger equations, whose solutions are spatial wave functions for states of definite energy (stationary states). When the periodic potential is set equal to zero, the solutions of such equations are plane waves, mathematically described in exponential form as $\psi = e^{i\vec{k}\vec{r}}$. Solving the equation, considering the wave function to be a plane wave, it is obtained that the electronic energy is proportional to the square magnitude of the wavevector $\vec{k}$. Hence if there is no perturbation, a parabolic relationship between electronic energy and $\vec{k}$ is achieved, shown in Figure 1.2. When the perturbation is taken into account, the Hamiltonian operator in the Schrödinger equation also contains the potential operator, which describes both the interaction of an electron with massive atomic nuclei and the electron–electron interaction. The presence of the electrostatic potential affects appreciably only outer–shell electrons (conduction electrons), which are called Bloch electrons.

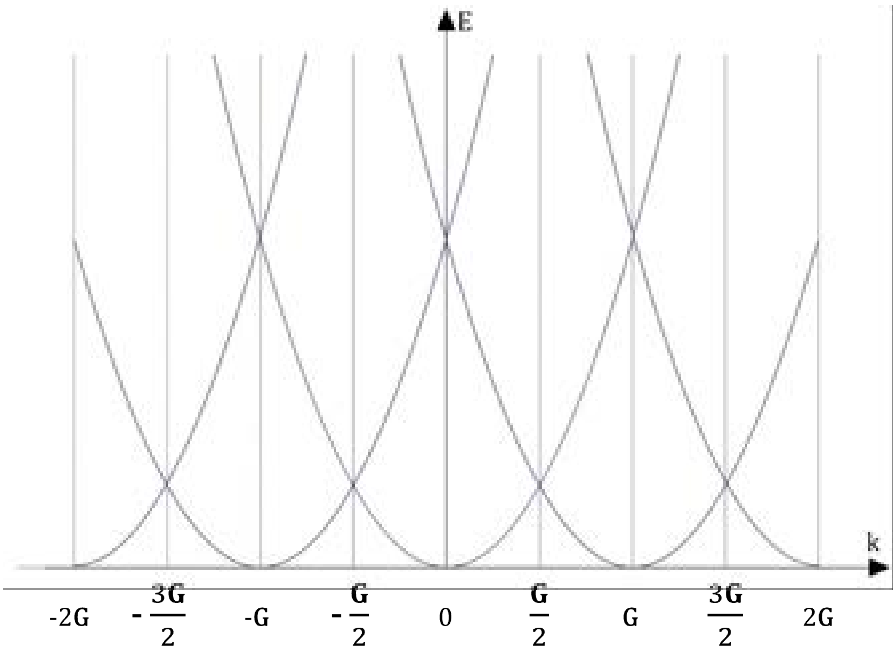

Figure 1.2: Free-electron energy parabola versus k in a one dimensional lattice. Ions lie in crystal planes (dashed lines) which are determined by the reciprocal lattice vector $\vec{G}$.

The wavefunction of a Bloch electron can be expressed according to Bloch's theorem as the product of a plane wave ($e^{i\vec{k}\vec{r}}$) and a function which has the same periodicity as the lattice ($u_{\vec{k}}(\vec{r})$):

$$\psi_{\vec{k}}(\vec{r}) \;=\; e^{i\vec{k}\vec{r}} \;\; u_{\vec{k}}(\vec{r}) \tag{1.1}$$

To impose that a wave function is periodic on the Bravais lattice it is necessary that it obeys periodic boundary conditions, called Born-Von Karman. Establishing $\vec{a}_i$ the i-th primitive basis vector of the real lattice and N_i the number of primitive cells along such direction, the Born-von Karman conditions can be written as

$$\psi(\vec{r}) \; = \; \psi(\vec{r} \; + \; N_i \vec{a_i}) \quad i = 1, 2, 3 \tag{1.2}$$

Applying Bloch's theorem to these conditions, a connection between the wavevector $\vec{k}$ and the reciprocal lattice is found. The wavevector $\vec{k}$ is also a reciprocal lattice vector, and therefore

$$\vec{k} = \sum_{i=1}^{3} \frac{m_i}{N_i} \, \vec{a}_i^* \; \rightarrow \; \vec{k} = \sum_{i=1}^{3} \chi_i \, \vec{a}_i^* \qquad m_i, \chi_i \in \mathbb{N} \tag{1.3}$$

The a_i^* are the basis vectors of the reciprocal lattice. It is important here to recall the correspondence between lattice planes and reciprocal lattice vectors. Given a set of real lattice planes equidistant and parallel to each other, their orientation in space can be described using a vector normal to them. By construction, the reciprocal lattice vector is collinear with this normal vector, and the interplanar spacing corresponds to the magnitude of the reciprocal lattice vector. The number of allowed wave vectors $\vec{k}$ in a primitive cell of the reciprocal lattice is so equal to the number of atomic sites in the crystal.

The periodic potential $u_{\vec{k}}(\vec{r})$ in the Bloch theorem can be developed into a Fourier series in the reciprocal space:

$$u_{\vec{k}}(\vec{r}) = \sum_{\vec{G}} \; C_{\vec{k}-\vec{G}} \;\; e^{-i\vec{G}\vec{r}} \tag{1.4}$$

with $\vec{G}$ a generic reciprocal lattice vector. Any reciprocal lattice wavevector $\vec{k}$ can be confined to the first Brillouin zone, the set of points reached from the origin without crossing any Bragg plane in the reciprocal space, shown in Figure 1.3 for a two-dimensional oblique lattice.

It is to be stressed that electronic states in amorphous materials can not be characterized by a wave vector $\vec{k}$ confined to a single Brillouin zone, so the Bloch's theorem is no valid in them.

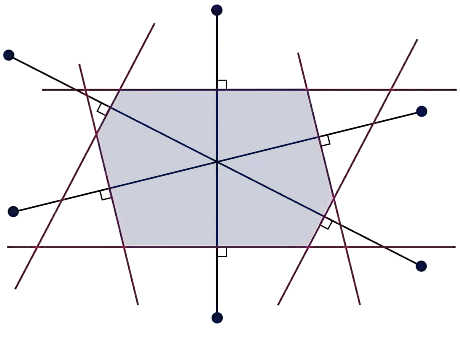

Figure 1.3: The first Brillouin zone for an oblique lattice in two dimensions (light blue area). Blue dots are reciprocal lattice point, pink lines are perpendicular to lines that connect the points to each other (black lines).

The value of the wavevector $\vec{k}$ is chosen so that:

$$-\frac{\pi}{|\vec{R}|} \leq |\vec{k}| \leq \frac{\pi}{|\vec{R}|} \tag{1.5}$$

where $\vec{R}$ is the direct Bravais lattice vector. This restriction is always possible because a vector in the first Brillouin zone can always be written as the difference between a vector that is not in the zone and another generic reciprocal lattice vector. Hence, from here on, when referring to the wavevector $\vec{k}$, it is restricted to the first Brillouin zone.

The condition that $\vec{k}$ belongs the first Brillouin zone is useful since it implies that every Bloch state has an unique $\vec{k}$. For a fixed wavevector $\vec{k}$, there are a set of Schrödinger equations, one for each generic reciprocal lattice vector $\vec{G}$. Solutions of all these Schrödinger equations can still be expressed as periodic functions of the wavevector $\vec{k}$:

$$\psi_n(\vec{k}) = e^{i\vec{k}\vec{r}} \quad u_{n,\vec{k}}(\vec{r}) \tag{1.6}$$

where n is a positive integer, called band index. The many different solutions of the Schrödinger equation for a given k value are identified by such index. For each n, there is a large number of discrete but closely spaced energy levels (eigenvalues), which is called energy band. Therefore, the energy levels lie in allowed energy bands, with an energy gap in between where such energy levels are not present.

The energy gap between two allowed bands, also known as forbidden band, decreases as the atomic spacing decreases, so for small enough distances such bands overlap. Bloch's theorem hence describes the electronic bands and how the geometrical properties of a crystal are reflected on the electronic properties. In Figure 1.4 it is shown the energy band diagram in a bulk material.

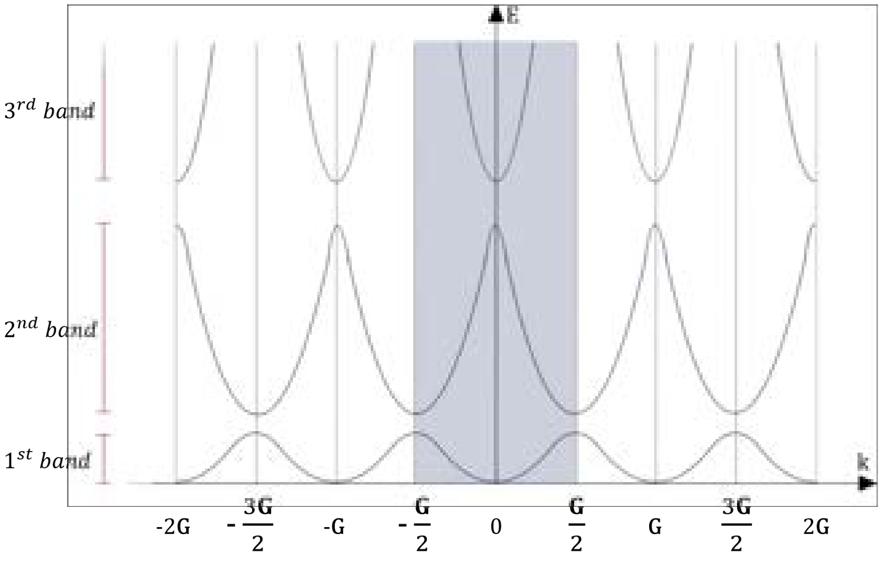

Figure 1.4: Plot of energy versus wave vector $\vec{k}$ for electrons in a lattice in one dimension. Ions lie in crystal planes (dashed lines) determined by the reciprocal lattice vector $\vec{G}$. The light blue area is the first Brillouin zone.

The partially or fully occupied band of highest energy is called the valence band. The empty band which is immediately above the valence band is called conduction band.

Solids can be classified as conductors, semiconductors, and insulators based on the relative position of these two bands:

i) In a conductor, the conduction band and the valence band overlap each other. Since electrons can readily pass into the conduction band these materials are characterized by high electrical conductivity.

ii) In a semiconductor, the empty conduction band is separated by a narrower energy gap from the almost filled valence band. Semiconductors are characterized by low electrical conductivity at room temperature.

iii) In an insulator, the energy gap between the valence band and conduction band is very large. Insulators are poor conductor of electricity.

Actually, semiconductors can be defined as materials that are insulators at absolute zero, but whose energy gaps are such that thermal excitation can lead to observable conductivity at temperatures below their melting point. Thermal energy is one of the main mechanisms to excite electrons to the conduction band. The electrical conductivity is so strongly dependent on the temperature of the material. Semiconductors are further split in two categories: direct–band–gap and indirect–band–gap materials. If the valence band maximum and the conduction band minimum have different wave vectors $\vec{k}$, the material is defined as indirect–band–gap semiconductor.[2, 3]

Bloch's theorem is typically the most important mathematical tool to describe the electronic band structures of crystalline solid. This interpretation affords the basis to explain the optical properties of solid, as they are mainly determined by the electronic structure of the material. However, real crystals deviate from the ideal model that assumes a perfect periodic crystal. Crystal defects, like foreign atoms and vacancies, are unavoidable imperfections in real materials that strongly affect the physical properties of the material because in the neighborhood of such defects the solid is not the same as elsewhere in the crystal. Impurities and defect centres in real crystals often have energy levels within the bandgap. Hence, alongside interband transitions, electronic transitions may take place either between the localised energy levels of the specific centre, or between these levels and the valence and/or conduction band. The result is that defects and impurities also participate in determining the optical properties of a material.

In addition, the electronic/optical properties of luminescent *nano*materials are different from those of their bulk counterparts, since the reduced dimensionality in nanocrystalline domains generates sizable changes in the energies of the electronic band and introduces strong surface effects. Objects of nanoscale dimensions thus show unusual and unique optical properties that can be also tuned by changing the size, shape, composition and surface chemistry, to make them amenable to application in an array of fields. For these reasons, in recent decades, photoluminescent inorganic nanomaterials have attracted the interest of the scientific community.

1.1.1 Optical spectroscopy

Photoluminescence (PL), as aforementioned, is a radiative decay of excited electrons featured by a wide variety of inorganic materials both in bulk and at the nanoscale. It can be classified as intrinsic luminescence and extrinsic luminescence depending on whether the emission of light derives from electronic transitions of ions introduced voluntarily (doping) or whether it derives from intrinsic defects in the material itself.

Intrinsic PL occurs in pure (undoped) inorganic nanomaterials due to interband transitions or due to transitions at energies below the band gap. The latter are enabled by the presence of additional energy levels generated by intrinsic material defects such as vacancies and interstitial ions (e.g., F-centers in ionic crystals).

Extrinsic PL is related to impurity–induced defects, it occurs in nanomaterials intentionally doped with luminescent ions. In this context, typical photoluminescent inorganic materials are crystalline hosts (dielectrics or semiconductors) doped with a generally small amount of lanthanide or transition metal ions.

To obtain information on both intrinsic and extrinsic transitions it is necessary to use an optical characterization technique, in particular PL spectroscopy. Spectroscopy is basically an experimental science that deals with the absorption, emission, or scattering of electromagnetic (EM) radiation from atoms, ions, and molecules. It can also concern the emission of other types of particles following the bombardment of photons, such as neutrons, electrons and protons.

The electromagnetic spectrum is the classification of EM waves according to their various wavelengths/frequencies. It includes wavelengths of electromagnetic radiation ranging from short–wavelength gamma rays to long –wavelength radio waves. It is divided by convention into seven spectral regions; radio waves, microwaves, infrared, visible and ultraviolet light, X–rays, and γ–rays. Each portion of the spectrum has quantum energies appropriate for the excitation of certain types of physical processes. Optical spectroscopy mainly concerns itself with the region in the electromagnetic spectrum starting in the ultraviolet (at $\lambda \sim 200$ nm, E$\sim$ 6 eV) and continuing until the near–infrared (at $\lambda \sim 3000$ nm, E$\sim$ 0.4 eV), see Figure 1.5. Such wavelength range is called optical range.

When impinging on matter, electromagnetic waves spanning in the wavelength range from 200 to 30,000 nm may undergo several fundamental interactions, like absorption, reflection, refraction, transmission, luminescence, elastic and inelastic scattering.

Reflection is the physical phenomenon in which the incident waves bounce back after interacting with external (surface reflection) or internal surfaces (volume reflection), resulting in reflected waves.

Refraction is when part of the incident waves change their direction of propagation inside the matter. While propagating through the material, such refracted waves can be transmitted, scattered or absorbed.

Transmission is when the EM waves pass and leave the material, the intensity of the transmitted beam is lower than the incident radiation due to reflection, scattering and absorbance.

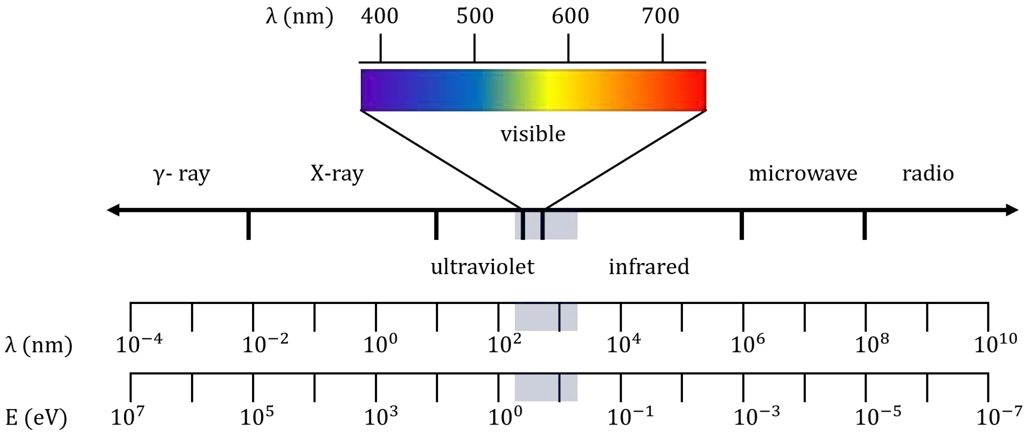

Figure 1.5: Electromagnetic spectrum showing the energy of one photon and wavelength. The blue rectangles highlight the portion of the EM spectrum relevant to optical spectroscopy.

Scattering, also known as diffusion, is a physical phenomenon in which the refracted waves spread in several directions due to elastic or inelastic processes. Elastic scattering, also called Rayleigh scattering, is the process in which the loss of energy is negligible, so diffused waves have the same frequency of the incident ones. In inelastic scattering, usually called Raman scattering, the scattered photons have a different energy compared to the incident ones due to a frequency shift.
Finally, absorption occurs when the energy of the electromagnetic radiation is high enough to allow an electronic transition from the ground to the excited state.

A brief explanation of how electrons are distributed within atoms is necessary to describe an electronic transition and the different transitions that can occur in transition metals and in lanthanides. For this purpose, a quantum mechanical approach has to be used. A multi-electron ion is treated as a system of Z electrons moving independently to each other, so the overall time-independent Schröedinger equation can be split into a set of Z equations with the same form. From the resolution of the various eigenproblems, it can be concluded that the energy of electrons depends on the number of subshells (angular quantum number ℓ) as well as on principal quantum number (n).
In the ground state, electrons must fill all subshells in such a way as to minimize the total energy of the atom, but not exceed the capacity $2(2\ell + 1)$ of any subshell. Each value of ℓ describes the shape of the orbital, and there are four subshell: s (ℓ=0), p (ℓ=1), d (ℓ=2) and f (ℓ=3). The number of orbitals and their orientation within a subshell is defined by the magnetic quantum number, denoted by the symbol m_ℓ. The orientation of the spin axis of a single electron is specified by the spin quantum number m_s. For a multi-electron atom, the total spin quantum number S can be also defined, viz. some of all m_s number.
The orbitals of a given set p, d or f of an isolated atom are treated as having equal energy, i.e., they are degenerate. However, degeneracy is not a valid approximation when the atom is in an asymmetric field. Hence, five d orbitals (in d-block elements)

as well as seven f orbitals (in f-block elements) are not degenerate when ions are not isolated.

Absorption

Now that distribution of electrons within an atom in the stationary state has been clarified, it is possible to properly describe the processes that are involved in photon absorption. Considering a two-state system m and n (non-degenerate stationary states) and an electromagnetic wave of frequency ν, absorption consists in the promotion of some electrons from m to n by absorbing incident photons. It happens only if the energy separation between these states is equal to the energy of the incident photon.

$$\Delta E \; = \; E_n \; - \; E_m \; = \; h\nu \tag{1.7}$$

In some situations, multi–photon absorption can also occur, in which several photons are absorbed simultaneously to achieve the excited state.

Since the XVIII century the relation between the quantity of light absorbed with the thickness of a material has been empirically proven, first by Pierre Bouguer and then by Johann Heinrich Lambert. Over the following century this relationship was expanded by also demonstrating the correlation with the concentration of the absorbing substance by August Beer.[4]

This empirical law can be expressed as:

$$I(\nu) \; = I_0(\nu) \; e^{-\alpha(\nu) \; x} \tag{1.8}$$

Where $\alpha(\nu)$ is called extinction (or attenuation) coefficient at specific frequency ν and x is the thickness of the material, also called optical path length. The ratio between the intensity of transmitted radiation (I) and that of incident beam minus the reflection losses (I_0) is termed transmittance, and its negative natural logarithm is defined as absorbance. In Beer–Lambert law, scattering is implicitly considered negligible, the attenuation of the incident intensity (removed the part lost as reflection) is only associated to absorption phenomenon.

The attenuation coefficient $\alpha(\nu)$ is associated to the maximum value of absorbance, but it does not give any information about the width of the absorbance band. It is to be stressed that this experimental factor is characteristic of the material. To understand the origin of $\alpha(\nu)$, the probability that an electronic transition occurs has to be introduced.

The selection rules

The probability of an electronic transition between two states can be expressed in term of transition dipole moment $\vec{R}^{nm}$. It is a transient dipolar polarization created by the interaction of photons with the ion. The transition dipole moment involves an integral over all three Cartesian coordinates

$$\vec{R}^{nm} \; = \; \int \; \psi_n^* \; \vec{\mu} \; \psi_m \; d\tau \tag{1.9}$$

The square of the magnitude of $\vec{R}^{nm}$ corresponds to the transition probability of exciting an electron from ψ_m to ψ_n. Hence, a transition is considered allowed when

$\vec{R}^{nm}$ is different from zero.
Some rules governing transitions can be formulated by analyzing the transition dipole moment, the so-called selection rules. They formally constrain the transition of a quantum mechanical system from one state to another.
Electronic transitions obey two selection rules: the spin rule and the Laporte rule. The first states that a change in spin multiplicity is forbidden, concisely ΔS=0. Some deviations of the spin rule can happen. They are caused by the spin –orbit coupling, the interaction between the electron's spin and its orbital motion around the nucleus. Spin-forbidden transitions are usually one to two order of magnitude weaker than the ones obeyed by the spin rule.

The Laporte selection rule states that a transition must involve a change in parity, $\Delta\ell=\pm\ell$. The transition dipole moment is non-zero only if two wavefunctions ψ_n and ψ_m are of opposite parity, and they can be either even-function (gerade, g) or odd-function (ungerade, u).
Deviations of the Laporte rule can happen due to some perturbations of the symmetry properties of the sites. The electronic transitions involved in emission of lanthanides and transition metals are exceptions to this rule, they are discussed in the paragraph 1.1.3.

Absorption cross section and attenuation coefficient
The intensity of absorbance bands arising from allowed- and forbidden- electronic transition at the same conditions (same length of light path and quantity of absorbing material) are different. This suggests that the empirical absorption coefficient is related to the probability of absorption occurring. The rate of change of population density in the lower state (m) due to the induced absorption can be written as:

$$\frac{\partial N_m}{\partial t} = -B_{mn}\ \varrho(\nu)\ N_m \tag{1.10}$$

B_{mn} is defined as Einstein coefficient, and $\varrho(\nu)$ as the energy density of the electromagnetic waves at given frequency ν, also termed as spectral radiation density. The Einstein coefficient is independent of properties of the electromagnetic radiation. B_{mn} is related to the wave functions ψ_m and ψ_n of the combining states through the magnitude of the transition dipole moment $\vec{R}^{nm}$, so that

$$B_{mn} = \frac{8k\pi^3}{3h^2}|\vec{R}^{nm}|^2 \tag{1.11}$$

where k is known as Coulomb's constant (intrinsic property of the material dependent on the relative permittivity) and h is the Planck's constant.
Einstein's coefficient is therefore proportional to the transition probability, and it can reasonably be related to the transition probability per unit time, called absorption cross-section $\sigma_A(\nu)$.

$$B_{mn} = \hbar\ \lambda\ \sigma_A(\nu) \tag{1.12}$$

where $\hbar$ is the reduced Planck's constant and λ is the wavelength associate to the wave frequency by the fundamental relationship $\lambda = \frac{c}{\nu}$ with c (speed of light). The change in the intensity of incident light due to absorption in terms of absorption cross-section $\sigma_A(\nu)$ can be calculated

$$\frac{dI}{I} = (N_m - N_n)\ \sigma_A(\nu)\ dx \tag{1.13}$$

Integrating the previous equation over I on the left and over the position on the right, then integrating also the attenuation coefficient over all possible frequencies ν, a relation between attenuation coefficient and absorption cross-section can be obtained:

$$\alpha_A(\nu)\ =\ N\sigma_A(\nu) \tag{1.14}$$

with N the number of ions/molecules per unit volume.[5–7]
If absorption is associated to absorbing atoms or ions, such as dopant ions in some transparent crystalline material, the absorption coefficient is the product of the doping density (number of ions per unit volume) and the absorption cross–section at the relevant optical wave frequency.[8]
Once the radiation is absorbed, the system is in an excited state and can release through different mechanisms the absorbed energy.

Relaxation mechanisms of a system after photoexcitation

The energy of an excited state is lost by a combination of radiative and nonradiative processes (i.e. loss of energy as thermal energy). When the system returns to the ground state by spontaneous emission of photons, the process is called photoluminescence (PL). Experimentally, the excitation photons are commonly converted into lower energy photons by the luminescent matter. The difference between the wavelength at which the ion emits light and that at which it was excited is referred as Stokes shift. This energy variation is associated to the nonradiative decay mechanisms and most of them result in the emission of phonons. Lattice vibrations have a key role in optical spectroscopy, and in particular in PL spectroscopy.
A powerful tool for visualising the different physical processes, radiative and nonradiative, that can occur after a material has been photoexcited, is the Jabłonski diagram, shown in Figure 1.6.

The non–radiatively loss of energy by electrons can happen before the PL, thereby reducing the number of emitted photons. It is known that each electronic energy level of an ion has a set of vibrational levels which are also quantised. The energy separation between the ground state and the next higher electronic level is on the order of the visible-ultraviolet light, while that between two vibrational levels is on the order of the IR waves.
Electrons can decay to lower either vibrational states or electronic states through vibrational relaxations, internal conversions, and quenching, for examples.

Vibrational relaxation can happen because excitation usually occurs to a higher vibrational level of the target excited state. So electrons are excited by incident radiation from the lowest vibrational level (vibrational quantum number v equal

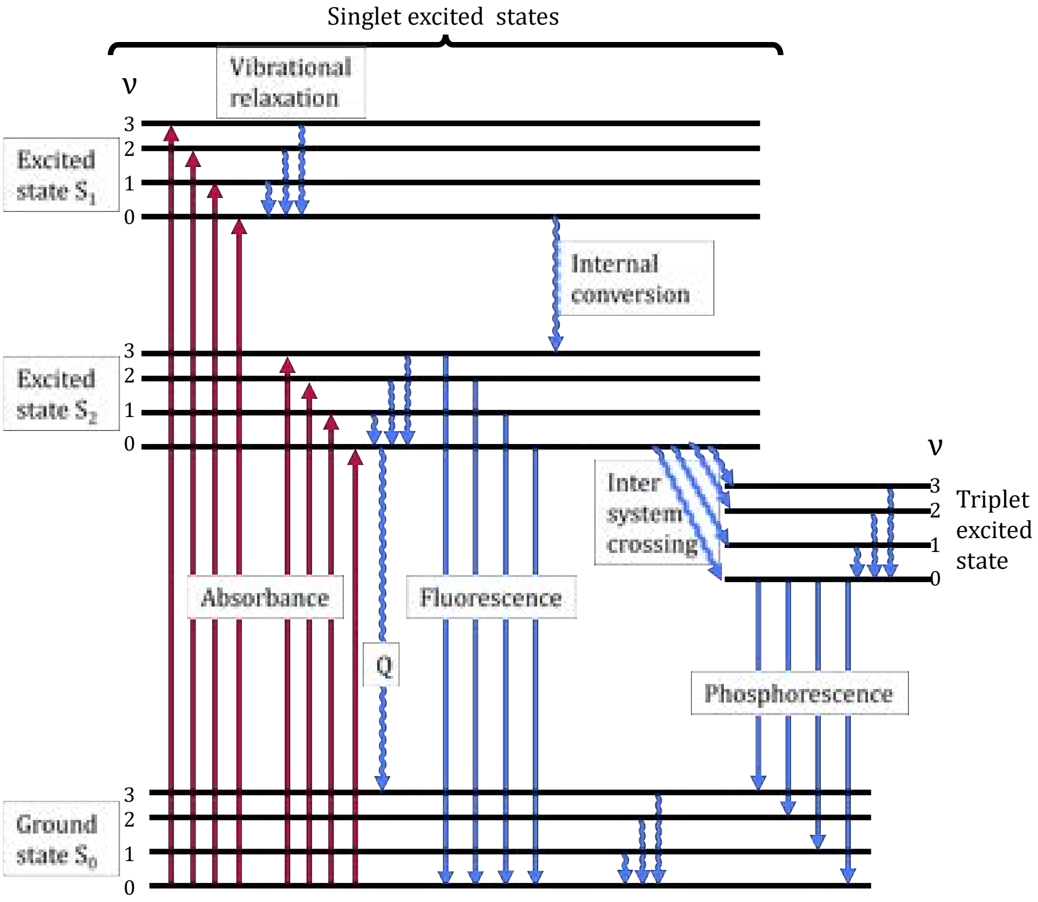

Figure 1.6: Jabłonski diagram. In pink the photoexcitation, in blue several decay pathways. Wavy lines represent non-radiative relaxations, and straight lines for two radiative processes. Q stands for thermal quenching.

to zero) embedded on the electronic ground state (label as S_0 with energy E_0) to an excited vibrational level ($v \neq 0$) within an excited electronic state. Vibrational relaxation consists in the decay by phonon emission (one or more) to the ground vibrational level. It takes place prior to luminescence since it occurs within 10^{-14} -10^{-12} s, a time shorter than typical luminescence lifetimes ($\sim 10^{-12}$ -10^{-10} s).

Internal conversion is another mechanism through which electrons can lose part of their absorbed energy. It happens when a vibrational state of an electronically excited state couples (interacts) to a vibrational state of a lower electronic state. The excited electron decays from a vibration level in one electronic state to another vibration level in a lower electronic state. It rarely implies transitions towards the vibrational ground state within S_0. The time period of this process is of the order of 10^{-12}. However, for this mechanism to be put in place, a requirement should be fulfilled: the vibrational energy levels should strongly overlap with the electronic energy levels. This condition usually appears at energy levels higher than the first excited state and/or when there is a strong electron –phonon coupling.

Non-radiative relaxation can also occur through thermal quenching, a phenomenon strictly related to the temperature. When the temperature is raised, the extinction of the luminescence is observed due to the thermal population of higher vibrational levels (v $\neq 0$) within the electronic ground state S_0. Electrons can so move from an excited electronic state to S_0 but in a vibrational level that is not the lowest one. This is the underlying phenomena of all luminescence thermometry measurement principles.

Another non-radiative decay can occur when an excited center, like a dopant ion, transmits its excitation energy without photon emission to a second nearby center, thus transferring energy. In that case, impurities that absorb excitation radiation and transfer their energy to other ions are called sensitisers (or donor), and those that accept such energy are called activators (or acceptor).
The energy transfer can happen when the difference between two energy levels in the donor/sensitiser is resonant to the energy gap in the acceptor/activator. Otherwise, the energy transfer process may occur if the lack of resonance between the energy difference is compensated by lattice phonons with appropriate energy.
This non-radiative mechanism explains also the luminescence concentration quenching, namely if initially the PL enhances as the concentration of dopant ions increases, once a threshold value is reached it undergoes a progressive decrease (quenching starting point). Such value of concentration is the one at which the average distance between luminescent centers is small enough to enable energy transfer. Generally, as the concentration of luminescent centre is increased above 10% the phosphor efficiency decreases.[9]
When the energy transfer is very efficient (many impurities all close together) the excitation energy can migrate between a large number of centers before being emitted. However, this migration increases the possibility that the excitation energy is transferred to quenching traps (e.g., defects) rather than to another luminescent ion. These centers can relax to their ground state by multiphonon emission or by infrared emission. After an excitation energy migration or even without, PL can undergo a quenching also due to cross–relaxation. This process consists in the transfer of absorbed energy between two different centres, but this mechanism leaves both ions with electrons in lower energy levels.

When there is a pair of electrons in the ground state, their spins may or may not change after photoexcitation. When the transition is spin-allowed, the excited state is called singlet and electrons has an antisymmetric configuration. Otherwise, electrons are in a symmetric configuration and the excited state is called a triplet. The Coulombic repulsion is less intense in the triplet state energy, so the energy of the lowest triplet state is usually lower than that of the first excited singlet state. A non-radiative transition between two electronic states with different spin multiplicity may happen, and it is called intersystem crossing. In Figure 1.7 is reported a schematic drawing of singlet and triplet states.

Finally, the radiative release of absorbed energy is PL. This is a generic term that includes two main phenomena: phosphorescence and fluorescence. The first is achieved

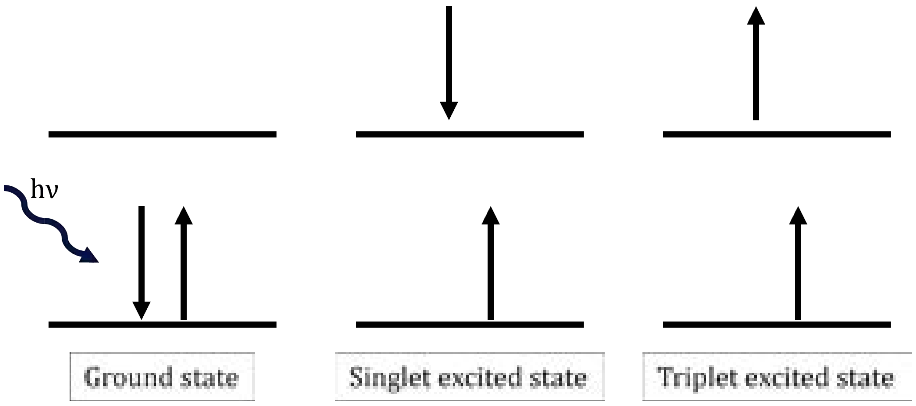

Figure 1.7: Schematic representation of singlet and triplet states. Wavy arrow represents the incident photon.

by radiative decay of electrons from the triplet excited state to the ground state. It is long-lived PL, it continues long after the photoexcitation has ceased. Fluorescence arises from the decay of electrons from the singlet excited state to the ground state (spin-allowed transitions). It ceases shortly after photoexcitation of the material.

Efficiency of light-conversion

The emission processes most exhibited by phosphors are: downshifting, downconversion, upconversion and resonance emission. When the frequencies of the emitted and absorbed photons are identical, the emission is resonant, and the energy conversion is 100%. When the luminescent material converts the excitation photons into lower energy photons (longer wavelength), the emission is termed downshifting. When the nanomaterial is an upconverter it absorbs several lower energy photons and combines them to yield a higher energy photon, reducing the quantum yield. On the contrary, downconversion nanomaterial converts a higher energy excitation photon into several lower energy ones.

Three spectroscopic key parameters are often used to assess the efficiency of the conversion of absorbed photons into emitted photons of light–emitting nanomaterials: the PL quantum yield (PLQY, Φ), the brightness and the quantum efficiency. The first parameter is defined as the ratio of the number of photons emitted to the number of photons absorbed in the stationary regime, so the equation is not time dependent.

$$\Phi = \frac{\text{number of emitted photons}}{\text{number of absorbed photons}} \tag{1.15}$$

The PLQY is so 100% only when for each absorbed photon one photon is emitted. In common language, the term brightness is often used to describe the intensity with which luminescent materials emit light. From a scientific point of view, the brightness of a phosphor depends on the relative number of emitted and incident photons. It is defined as the product between the PLQY and the molar extinction coefficient ϵ ($\alpha(\nu)$ per mole of substance).[10]

$$\beta = \Phi * \epsilon \tag{1.16}$$

Brightness is a good parameter to get an idea of the intensity with which luminescent materials emit light as it considers both absorption and emission efficiency providing a more complete view of the phenomenon. However, PLQY and β being no energy-dependent are not enough to get a complete insight in PL. Thereby, the quantum efficiency η should be also taken into account. This parameter is defined as the ratio between the energy of emitted photons over the energy of excited photons. The energy of photons is proportional to the intensity, so the quantum efficiency η can be calculated in terms of intensity.

$$\eta = \frac{I_{em}}{I_{abs}} \tag{1.17}$$

The quantum efficiency η is 100% only for resonance emission and smaller for all the other emission processes.[10]

Given the variety of electronic transitions that give rise to PL and of ways to fine-tune it by controlling severe parameters, plenty of possible luminescent nanomaterials (nanophosphors) exists.

1.1.2 Classification of nanosized phosphors

Photoluminescent inorganic nanomaterials can be classified based on their chemical composition in:

- Metallic nanoparticles, usually gold, silver, platinum, copper. Their physical and chemical properties strongly depend on the size, shape, composition and even architecture of the assembly. The PL of metal nanoparticles is mainly attributed to the quantum confinement effect (their size is usually a few nanometers so the effect is very important) and to the charge transfer due to the interaction between the metal nucleus and the ligands on the surface of the nanoparticles. nanoparticles.[11, 12]
- Metal halide perovskites nanomaterials, they have a general chemical formula of ABX_3, where A is a monovalent cation like Cs^+ and Rb^+, B is a heavy divalent cation (Pb^{2+}, Sn^{2+}, Bi^{2+}), and X stands for a halogen (Cl^-, Br^-, I^-). This variability in the chemical composition, along with different obtainable crystal structures, results in perovskites with a wide range of electronic structures.[13]
- Metal oxides nanoparticles, two most relevant types are rare earth metal oxides (REMOs) and transition metal oxides (TMOs) nanomaterials. These nanomaterials exploit the characteristic luminescence of transition metal and rare–earth ions, that are explained in detail in the next paragraph 1.1.3. Their emission bands span the visible and near–infrared spectral ranges depending

on the metal ion. Some relevant examples of metal oxides nanoparticles are SnO_2, Fe_2O_3, $CoFe_2O_4$, ZnO, CeO_2 and Gd_2O_3.[2, 14]

- Perovskite oxides nanomaterials, they have a general chemical formula of ABO_3, where A and B denote two different cations, A is usually an alkali metal or alkaline earth cation, and B is usually refers to Ti^{4+}, Ta^{4+} and Nb^{5+}. Most of them are semiconductors with wide band–gap energies.[15]

- Quantum dots (QDs), they are semiconducting nanoparticles, containing a hundred to a thousand atoms. Their chemical composition is quite variable, they combine d-block or post-transition metals (only in group 13 or 14) with N^{3-}, P^{3-}, As^{3-}, Sb^{3-}, S^{2-}, Se^{2-} or Te^{2-}. Some relevant examples are CdTe, CdSe, CdS, PbSe, ($CuInS_2$), CuS, Cu_2S,Cu_3N, Cu_3P, Ag_2S and zinc sulfide (ZnS). The PL emission of quantum dots can be tuned, alongside their chemical composition, by their size. The origin of the size dependence of the luminescent properties of quantum dots can be traced to the spatial confinement of quantum particles due to the limited size of the nanocrystals. The decrease in size of QDs gives rise to an increase in energy band gap and brings out discrete energy levels near the band edges, and so the wavelength of emitted photons is shorter (blue–shift). [16–20]

- Carbon–based nanomaterials, they are mainly carbon nanotubes, graphene (GQDs) and carbon (CQDs) quantum dots. Usually these materials exhibit tunable PL, depending on chemical structure or size they show wide or narrow optical emission in the visible or near infrared regions. Concerning GQDs, visible transitions are absent in pure graphite, but when some defects are introduced in graphite structure some changes are consequently created in the graphite electronic band, allowing even non–interband transitions.[21, 22]

- Metal halides nanocrystals, they are ionic compounds composed of alkali –metal, alkaline–earth, transition metal or lanthanide cations, and fluoride, bromide or iodide anions. Alkali and alkaline–earth metal halide nanomaterials display mainly PL in the ultraviolet region of the electromagnetic spectrum. Some relevant examples are NaI, CsBr, CsCl, CsF, RbF, BaF, BaF_2 and $CsMgCl_3$.[23, 24] In transition metal or lanthanide halides, PL is associated with the electronic transitions of the ions themselves, which will be widely described in paragraph 1.1.3. Examples include: $FeCl_2$, K_2CuCl_3, $LnCl_3$ (Ln = La^{3+}, Nd^{3+}, Sm^{3+}, Eu^{3+}, Gd^{3+}, Tb^{3+} or Yb^{3+}).

- Nanomaterials doped with luminescent ions, the PL phenomenon depends on the type of dopant, as well as on the lattice in which such ions are incorporated. Most used activators are transition metal (Sc–Zn and Y –Cd ions) and lanthanide ions (Ce^{3+}–Yb^{3+}). The electronic transitions involved in photoluminescent phenomena can be $3d^{10}$–$3d^{9}4s$, $3d^{n}$–$3d^{n}$, $4d^{n}$–$4d^{n}$, $4f^{n}$–$4f^{n}$ and $4f^{n}$–$4f^{n-1}5d$, leading to a wide variability in shape, number and location on the electromagnetic spectrum of generated emission peaks.[25] In paragraph 1.1.3 and section 1.2 it is explained in detail the involved mechanisms on the PL shown by transition metal and lanthanide ions, and an overview of host characteristics will be given with some examples of the most common nanomaterials.

1.1.3 The d- and f- block elements

In the previous section, it has been mentioned how the presence of luminescent centres contributes to the optical properties of luminescent nanomaterials. Centres in inorganic solids that are of interest from an optical standpoint include lattice defects –also called color centers –like vacancy centres in ionic crystals and recombination centres in semiconductors, and multi-electron impurities like transition metal and lanthanide ions. The optical properties of lanthanide (Ln) and transition metal (TM) ions differ considerably due to the distinct physical interactions involved. This subsection describes the differences between these cations and the physical phenomena that govern their luminescence underlining both advantages and disadvantages of their use as dopants. In particular, the luminescent properties of an ion are described by considering energy levels of the free ion, and then how the host crystalline material can influence the electronic structure of the ions.

The transition metals

When the angular quantum number ℓ is two (d-orbital), orbitals have "four leaf clover" shape, and the magnetic quantum number m_ℓ range from -2 to 2 (-2, -1, 0, 1, or 2). These five subshells, one for each m_ℓ value, are d_{xy}, d_{yz}, d_{xz}, $d_{x^2-y^2}$ and d_{z^2}. The image in Figure 1.8 represents the shapes of d-orbitals in Cartesian coordinates.

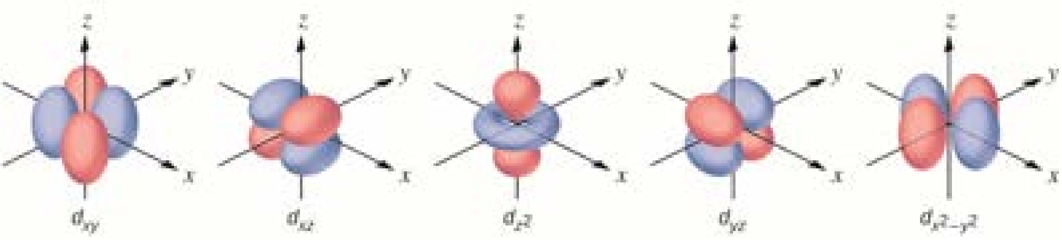

Figure 1.8: Shape of the one-electron d orbitals in a Cartesian space.

Transition metals are 35 elements with incompletely filled d orbitals. According to the International Union of Pure and Applied Chemistry (IUPAC), they include elements of the d block with the exception of group 12 elements (zinc, cadmium, mercury and copernicium) since they have a d^{10} configuration.[26] The so–called d block is divided into four series, each of them corresponds to the filling of 3d, 4d, 5d, or 6d shells respectively. There are minor deviations from this pattern, however. The metals in the fourth Period (Rf –Cn) are all synthetic elements, so they are not considered as they are not relevant for use as dopant ions.

In between the 4d and 5d levels is interposed the first f-sublevel, the 4f shell, which fills up after lanthanum. The atomic and ionic radii of elements in 4f-block gradually decrease with the increase in the atomic number. This contraction is approximately equal to the normal increase in size between one Period and the next, thus balancing the expected increase between the second and third series, viz. those filling the 4d and 5d shells. The main consequence of the resemblance in size of the pairs of heavy elements (Zr/Hf, Nb/Ta, Mo/W, etc.) is their similar chemistry. Therefore, each transition Group consists of three members (triad) and it can be split in two parts: the lightest element with its individual chemistry, and the pair of heavy elements with their similar chemistries. All d and s electrons are involved in the chemistry of the preceding elements, but once the d^5 configuration is exceeded, there is less tendency for d electrons to react. The main difference between the lighter element and the others in the same transition group, is the stability of the oxidation states. Higher oxidation states are more stable for 4d/5d elements due to the shielding of valence electrons from the nuclear charge, which is now stronger. The number of ligands adjacent to a metal ion in a complex, coordination, or crystalline compound, is termed as coordination number (CN) and it determines the geometry around the central metal ion. The most common coordination geometries for transition metals are square planar (CN=4), tetrahedral (CN=4) and octahedral (CN=6). Larger elements commonly exhibit higher coordination numbers, probably because more ligands can fit around the ion. Hence, for example, a transition metal like chromium has +3 as its most stable oxidation state and it supports low coordination numbers, typically 4 and 6.

When a transition metal ion is bound to some ligands, its orbitals pointing along the same axes as the functional groups, are more perturbed than orbitals that lie in other directions. Since ligands are regions of negative charge, those orbitals that lie in their same direction are sitting in a region of higher negative field than the non-aligned orbitals; as a result the electrons move as far apart as possible. Therefore, five d orbitals and three p orbitals are no longer degenerate, those which are found in the directions also occupied by the ligands have greater energy than the others. The size of the splitting of degeneracy depends on the size of the ligand field and this, in turn, depends on the distance of the ligand and thus on the intensity of the attraction between the central atom and the ligand. Such ligand fields occur in all chemical environments. The effect of the crystal field is significant for d orbitals and gives rise to the unique properties of transition metals. The effect of the crystalline field on d-orbitals is illustrated only for the octahedral geometry which is the subject of the experimental part of this thesis work.

When the coordination number is six, ligands are usually placed at the plus and minus ends of three coordinate axes x, y and z. Therefore, the d_{xy}, d_{yz}, d_{xz} orbitals are off-axis, unlike $d_{x^2-y^2}$ and d_{z^2} that point directly at the ligands. As result, d_{xy}, d_{yz}, d_{xz} orbitals are degenerate, and they are stabilised relative to the other two. Electrons in orbitals $d_{x^2-y^2}$ and d_{z^2} are also identical in energy, but they are destabilized.

The combined energy level diagram is composed of two upper degenerate orbitals, identified by the symbol e_g, and three lower degenerate orbitals, labelled as t_{2g}. Such energy difference ΔE between e_g and t_{2g} is termed as crystal field splitting energy.

The magnitude of the total energy separation is determined by the strength of the crystal field, two extremes being called weak field (small ΔE) and strong field (large ΔE). The magnitude of ΔE depends on the ligand and on the nature of the transition metal ion. The crystal field splitting energy for octahedral complex is often represented with the symbol Δ_{oct}. It can be measured spectroscopically by observing the energy of the electronic transitions between the t_{2g} and e_g orbitals, because the emission of transition metal ions arises from d-d transitions. Such electronic transitions usually lies in the visible or near-ultraviolet region of the electromagnetic spectrum. The nature of the transition metal ion also affects the crystal field splitting energy. The value of ΔE increases by about 30% between members of the same Group in successive Periods.

Transitions that give rise to PL of a given transition metals in a crystalline nanomaterial is thus strongly dependent on the surrounding environment. The stronger is the crystal field, the higher is the value of ΔE.

So far the atomic orbitals of transition metal ions have been discussed, but further aspects should be described to understand the spectroscopic properties of such active optical centres. Hence, the theory of the ligand field shall be introduced.

The d-d transitions, that give rise to PL, are electronic transitions that occur between molecular orbitals (MO) which has mostly metallic character.

The ligand field theory (LF) was simultaneously introduced by Hans Bethe and John Hasbrouck van Vleck in the 1930s. It is the combination of two theories: the crystal field theory, which considers only ionic interactions (electrostatic theory), and the molecular orbital theory, which assumes interactions with only covalent character. According to the LF model, the metal –ligand bond has ionic as well as covalent character.

Transition metals belonging the first row (Ti-Cu) has nine atomic orbitals: five 3d atomic orbitals $3d_{xy}$, $3d_{yz}$, $3d_{xz}$, $3d_{x^2-y^2}$ and $3d_{z^2}$, scilicet the sum of the aforementioned orbitals t_{2g} and e_g, the 4s orbital, and three 4p orbitals p_x, p_y and p_z. Thus, still referring to an octahedral site, there are six metal orbitals directed towards the ligands: the 4s that potentially overlap with all ligands, and five on-axis orbitals $3d_{x^2-y^2}$, $3d_{z^2}$, p_x, p_y and p_z. Each type of bonding produces a favorable energetic situation, σ or π bonding (depending on the donor atomic orbitals), and an unfavorable energetic situation, σ^* or π^* antibonding (from destructive interference of electron wavefunctions). Hence, in an octahedral geometry, the interactions of six transition metal atomic orbitals and the donor orbitals give rise to six bonding molecular orbitals (labelled as a_{1g}, t_{1u}, e_g) and six antibonding molecular orbitals (labelled as e_g^*, a_{1g}^*,t_{1u}^*). Three degenerate non-bonding orbitals from the metal centre are termed, like in the crystal field theory previously illustrated, t_{2g}. Filling the molecular orbitals with the twelve electrons from the ligand, the next available molecular orbitals that can be filled with d-electrons are three non-bonding MO and two antibonding MO e_g^*. So the overall molecular orbital energy level diagram consists of seven MOs, and strongly depends on the type of donor ligand.[2, 27–29]

When a transition metal is in a octahedral site, many absorption transition can happen between three non-bonding MOs and two anti-bonding MOs, from each t_{2g} to each e_g^*. In principle, such transitions should require the same energy, practically there are also some differences due to the contribution in the Hamiltonian of the potential energy associated to the electron-electron repulsion.

To summarize what it has been illustrated so far, small transition metal ions like Chromium (III) prefer low coordination number (4 and 6), and when they are not isolated their energy level structure is significantly affected by the surrounding environment, that is the host material where these ions are incorporated. In addition, the d-d transitions for configurations other than d^1 are rather more complicated, for example, d^3-transition metal ions (like Cr_3^+, [Ar] $3d^3$) has three electrons on three t_{2g} orbitals.

The lanthanides

When the angular quantum number ℓ is three (f-orbital), the orbitals have fairly complex shapes. There are seven subshells given that seven magnetic quantum number are available (m_ℓ = -3, -2, -1, 0, 1, 2 or 3). The image in Figure 1.9 represents the shapes of f-orbitals in Cartesian coordinates.

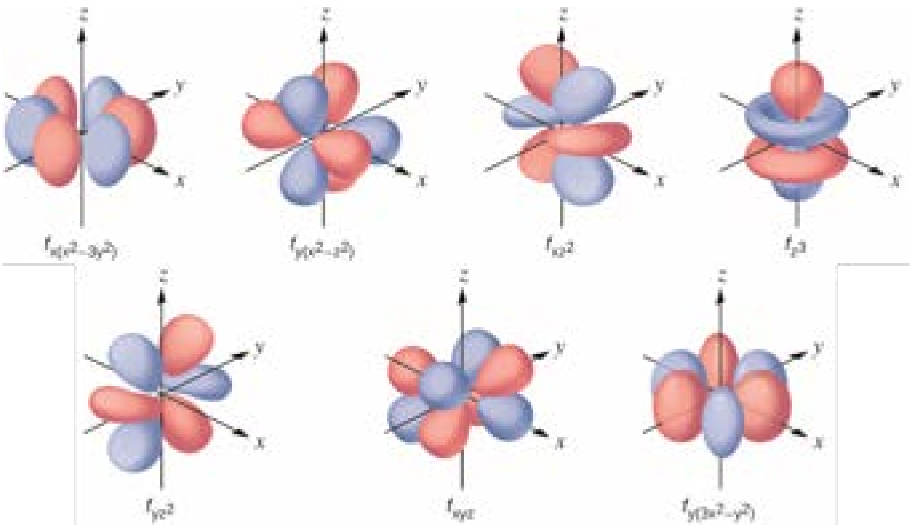

Figure 1.9: Shape of the one-electron f orbitals in a Cartesian space.

The 28 elements with filled f orbitals are equally split in two series, namely lanthanides and actinides. Actinides (Ac –Lr) are chiefly synthetic elements and are not relevant for use as dopant ions. Scandium, yttrium, lanthanum and fourteen 4f-block elements are together called rare earth elements (REEs). Their purported rarity does not refer to a low natural abundance, but to their non-trivial extraction from the minerals in which they are contained as well as their subsequent separation. The electron configuration of a lanthanide ion is [Xe] $4f^n$ $5d^{0-1}$ $6s^2$. The 5d and 4f levels are very close in energy, because of that, gadolinium - element with 64 electrons - has the electronic configuration [Xe]$4f^7$ $5d^1$ $6s^2$ and not [Xe]$4f^8$ $6s^2$. Instead of filling one of seven 4f orbitals with another electron, it is placed in a 5d orbital. As aforementioned, the atomic and ionic radii of lanthanides gradually decrease with the increase in the atomic number. This effect is called lanthanide contraction and it consists in a small but steady decrease from lanthanum (La, no f-electron) to lutetium (Lu, 14 f-electrons) due to the slow increase in effective nuclear charge as the f electrons are added. Then, however, lanthanides are very close in size, variations no greater than 20 pm, causing the chemistry of lanthanide elements to be similar. Lanthanide ions can have coordination numbers ranging from 6 to 12. Many lanthanides have the oxidation state III as the most stable electronic configuration, in which two 6s electrons and one 4f (or 5d) electron are lost. However there are some stable ions even at different oxidation numbers, i.e. Ce (IV) and Eu (II). During ionization, lanthanides lose 6s electrons before 4f electrons, so Pr^{3+} has configuration $[Xe]4f^2$ and not $[Xe]6s^2$, and this trend is abide by all lanthanides. This loss of electrons in the 6s orbital before those in the 4f, as well as the less pronounced effect of the crystalline field on the f orbitals compared to the d orbitals (experimentally proven) originate from the particular nature of the f orbitals themselves.

To understand the reason behind these features of the 4f–elements, it is necessary to introduce the probability density of finding the electron inside a differential volume $d\tau$, namely the absolute square of the wavefunction, that is a function of the spherical coordinates r (radial distance), θ (polar angle) and φ (azimuthal angle).

In this context, it is more suitable to focus in the radial probability function for hydrogen-like orbitals $|\psi^*\psi|\ r^2$, which refers to the probability of finding an electron at a given distance. ψ is the radial wavefunction. The maximum of the radial probability function for 4f is located at lower distance from the nuclei compared to those for the 5d and 6s orbitals, as shown in Figure 1.10.

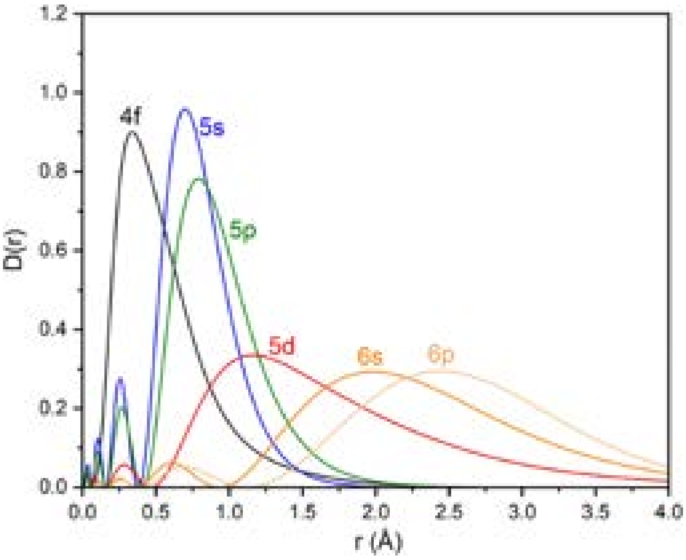

Figure 1.10: Radial distribution probability densities $D(r) = |\psi|^2\ r^2$ for 4f, 5s, 5p, 5d, 6s, and 6p orbitals of Nd atoms with the ($[Kr]4d^{10}5s^2 5p^6 6s^2 4f^4 5d^0 6p^0$) configuration. Distance from nucleus is on the x-axis.[30]

Therefore, electrons in the 4f orbitals undergo a greater electrostatic attractive force than that for electrons in the 6s and 5d orbitals. This would be enough to explain the loss of 6s-electrons, instead of the 4f electrons, due to ionization. But, the penetration of 4f orbitals is further favored, because even electrons of the 5s and 5p sublevels would appear to be further away from the nucleus than the electrons of the 4f sublevel. This implies that these orbitals do not take part in the shielding of the

4f electrons from the electrostatic force exerted by the nucleus. In conclusion, the 4f orbitals shall be considered as inner sub-shell, they do not extend out far enough to join in bonding to any appreciable extent. Hence, they are non-significantly affected by the surrounding environment, the ligand field crystal splitting is very slight, less than about 10% in energy. In lanthanide ions, an exponential decrease in the multi-phonon emission rate with an increasing energy difference involved in the transition is experimentally proven. This is because large energy gap between levels means large energy that should be compensated by the lattice vibrations, and the interaction, as mentioned, of the ion with the lattice is weak.

To summarize what it has been illustrated so far, lanthanide ions like Neodymium (III) prefer high coordination number (6-12). Due to the penetration of 4f-orbital, the perturbation of the energy level structure of such ions by the surrounding environment is little noticeable. Consequently, the emission bands of lanthanide ions in a crystalline host nanomaterial resemble those of a free ions.

Luminescence of transition metals and lanthanides

In paragraph 1.1.1, the selection rules governing optical transition has been illustrated. In the framework of PL of transition metals and lanthanides, the parity/Laporte rule is particularly relevant. When the cations occupy sites with inversion symmetry the transitions involved in the emission of these ions are electric dipole-forbidden. However, transition metal ions exhibit PL stemming from d-d transitions and lanthanide ions from f-f transitions even when the ions occupy sites with apparent inversion symmetry like octahedral sites. The rule is partially relaxed mainly due to two reasons: the d and f orbitals can mix with other orbitals of the ligands/anions generating some differences in the parity of these orbitals and lattice vibrations might move the ion from a perfectly symmetric coordination generating orbital admixing.

Threfore, the exceptions of Laporte rule are caused by some perturbations of the symmetry properties of the sites and to realise the reasons behind them, the dynamics of the ion and its surrounding environment has to be considered. Until now it has been assumed that the optical center is located in a static lattice. However, in a real crystal, the ion is part of a vibrating lattice, and it can also participate in the possible collective modes of lattice vibrations. A lattice vibration introduces a periodic distortion of the environment, especially in the separation between adjacent atoms. In a first approximation, atomic vibrations could be associated with a 3D-harmonic oscillator, however there is also an anharmonic contribution which leads to the deviation of the real movements from the model. In addition to the non-pure anharmonicity of lattice vibrations, the forces acting between the ions are not solely neighboring forces, every atom belonging to the lattice contributes to the overall motion in a real crystal.

However, for simplicity the vibrations of the optical center and the ions surrounding it are considered hereinafter as harmonic vibrations (normal modes). The loss of inversion symmetry, and therefore the non-applicability of Laporte's rule, can still be interpreted using this ideal model.

For an ion in a vibrating crystalline environment, the Hamiltonian operator should include a coupling term which depends on both electronic and nuclear coordinates. This implies that the factor should not be written as a product of two contributions. Most treatments of vibronic coupling implicitly neglect the possible electronic degenerations of the states involved in optical transitions in order to reduce the complexity of determining the effects of electron-phonon coupling. However, orbital degeneration exists and when it is taking into account, the coupling of electrons and lattice vibration is called the Jahn-Teller coupling. Such interaction is particularly relevant in octahedral complexes, in which as explained above, the electronic states of a transition metal ion are split into three-fold degenerate (triplet) t_{2g} states and two-fold degenerate (doublet) e_g states. These states may couple to some vibrational modes, leading to a decrease in energy and in symmetry of the system and consequently deviation from the Laporte rule. The centre of symmetry in the octahedral complex is so temporary lost due to lattice vibrations. When the system does not possess the centre of symmetry, mixing of d and p orbitals can occur, given that the lifetime of the vibration is usually longer (until $\sim$ 5 orders of magnitude) than that of an electronic transition.

Therefore, d-d transitions, as well as f-f transitions, are observable due to the dynamic lattice distortions that breaks the inversion symmetry that the luminescent ion would have if it was in a static lattice.

However, it is to be stressed that the probability of Laporte-forbidden transitions is lower than that of Laporte-allowed, and so also the attenuation coefficient $\alpha(\nu)$ is lower. The molar extinction coefficient ϵ is usually in the range 10^3 to 10^5 mol^{-1} cm^{-1} for Laporte-allowed transition. The d-d or f-f bands have much weaker ϵ, spanning from 10^{-1} to 10 mol^{-1} cm^{-1}. In addition, since the magnitude of the deviation of the Laporte rule is more relevant in transition metals compared to lanthanide ions, they usually present a higher value of absorption cross sections (and so attenuation coefficient). Regarding the spin selection rule, the spin –allowed d–d and f-f transitions remain Laporte-forbidden. Although, it should be noted that bands associated with 'spin-forbidden' transitions are very weak for first row transition metals (3d–3d transition) because the spin-orbit interactions has little relevance. Instead, the spin-orbit coupling is significant in lanthanides, so they usually exhibit spin-forbidden transitions.

The lattice vibration responsible to the weaking of Laporte rule are also related to the broadening of bands, besides the broadening of optical bands that happen increasing the temperature. The widths of emission (or absorption/excitation) bands of lanthanides and transition metals is indeed pretty different. It is well known experimentally that a strong vibronic coupling strongly influences the shape of optical band. In the majority of cases, broad optical bands are indicative of strong ion–lattice coupling, while sharp optical bands suggest weak ion–lattice coupling (weak electron–phonon coupling).

The strength of the ion-lattice interaction is the leading factor that determines the differences in full width at half maximum (FWHM) of optical bands arising from transition metal and lanthanide ions at the same external conditions. As previously discussed, since the d orbitals are bonding orbitals of transition metal ions, the elec-

tronic structure of these ions strongly depend on the type of ions by which they are surrounded and on the crystalline geometry. The interaction between transition metals and lattice is so relevant, and for this reason d-d transitions usually appear as broad bands.
Lanthanide ions, except La^{3+} with no f electrons and Lu^{3+} with no empty f orbitals, exhibit photoluminescent phenomena due to transitions between f levels. The ligand field splitting in f-orbitals, as aforementioned, is not significant due to the inner nature of these orbitals. Hence, both absorption and emission bands appear as narrow bands, similar to those of free ions. The emission bands of lanthanide ions cover the entire visible and near infrared spectrum depending on the nature of the ion itself.
The characteristic narrow emissions of Ln^{3+} facilitate spectral separation of bands during measurements, which is difficult with transition metals that exhibit bands so broad that they may be overlapped with others that have a different origin.

Trivalent lanthanide ions have numerous energy levels. In 1963, the first and most widely used, diagram of the energy levels of lanthanides known as the "Dieke diagram" was realised, shown in Figure 1.11.[31] This representation of energy levels was achieved through a systematic study of the emission and absorption spectra carried out by Dieke and Crosswhite. Levels are described through the Russell–Saunders notation. This method assumes that: spin–spin coupling > orbit–orbit coupling > spin–orbit coupling. The term symbols are in the form of

$$^{2S+1}L_J \tag{1.18}$$

where S represents the total spin quantum number (calculated as reported in paragraph 1.1.1), L specifies the total orbital angular momentum, and J refers to the total angular momentum. In a term symbol, the superscript is always an integer, the subscript is an integer or half-integer, and L is identified with spectroscopic notation. Therefore, each total orbital angular momentum is associated with a capital letter as shown in the table below:

L	0	1	2	3	4	5	6	7
	S	P	D	F	G	H	I	K

Table 1.1: Values of total orbital angular momentum and their associated spectroscopic terms.

If the Dieke diagram is an essential tool for understanding the electronic transitions possible in lanthanides, the Tanabe-Sugano diagrams result very useful for visualizing and comprehend the effects of electron-electron repulsion within transition metal complexes, as well as the influence of the crystal field strength on the energy levels. For each d^n (with n = 2–8) configuration there is an associated Tanabe-Sugano diagram, in Figure 1.12 the Tanabe–Sugano diagram for the d^3 configuration is shown. On the x-axis of the diagram there is the crystal field splitting parameter Δ_{oct} scaled by the B Racah parameter. The total inter–electronic repulsion in an ion is expressed in terms of the Racah parameters are A, B and C. They increase as the size of the

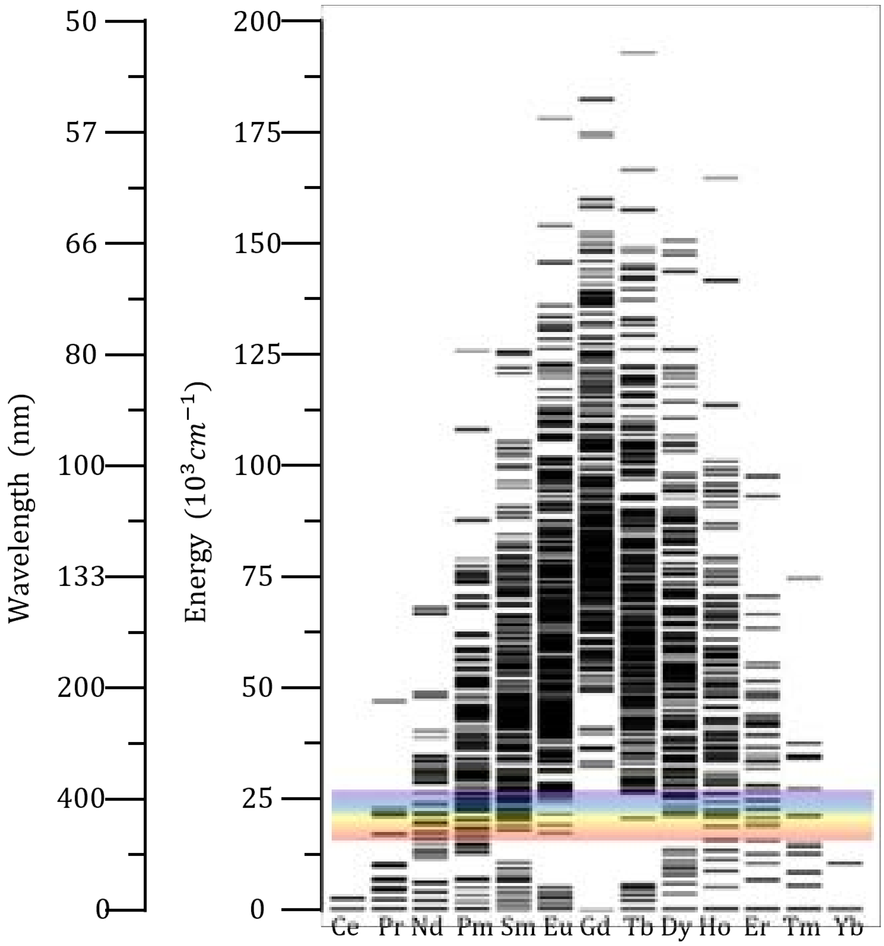

Figure 1.11: Complete 4f^n energy level diagram for trivalent lanthanides in LaF$_3$. Modified image from [32].

ion decreases because the electrons are confined to a smaller region and repel each other more. The y-axis is in terms of energy of a electronic transition, E, scaled by B; so both axes have normalized values for parameter B.

It has been mentioned that the absorption cross section of lanthanides is less than that of transition metals. The lower probability of absorption process compared to that of transition metals when both dopant lie a site with apparent symmetry, like an octahedral site in which the metal is surrounded by 6 equal ligands/lattice ions, is still related to the inner-nature of 4f-orbitals. Since the d orbitals are more influenced by the surrounding environment than f-orbital, the break of the symmetry (permanent or transitory) is facilitated and consequently the possibilities of deviations from Laporte's rule are greater in TM.
The last concept worthy of note is the temporal evolution of the intensity emitted by lanthanide and transition metal ions. Lanthanide ions show an extended lifetimes (from micro to milliseconds), generally longer than those of transition metal ions under the same external conditions (such as temperature and host material).[34–36]
In conclusion, these substantial dissimilarities between lanthanide and transition

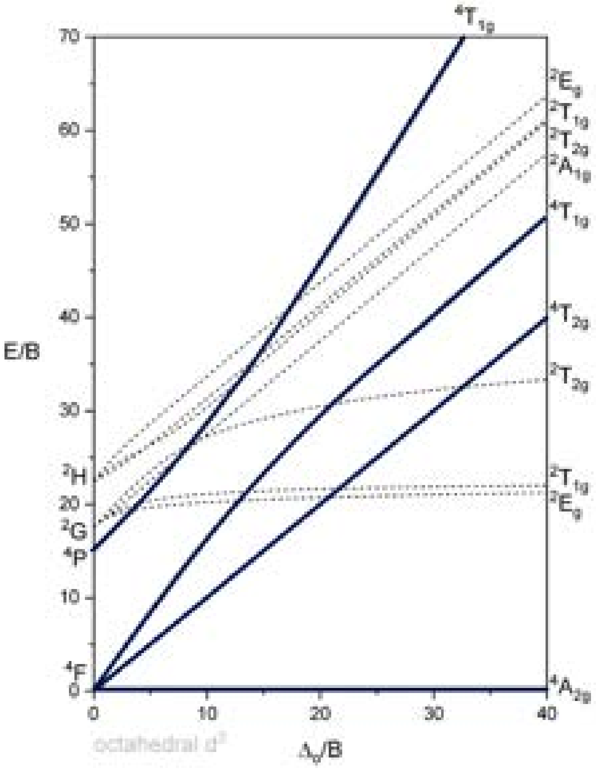

Figure 1.12: Tanabe–Sugano Diagram for octahedral metal complex with three d–electrons. Solid blue lines indicate spin-allowed transitions from the ground state (singlet to singlet transition), dashed black lines indicate spin-forbidden transitions from the ground state. Modified image from [33]

metal ions, especially with the ones belonging the first row, give rise to a different display of PL. Therefore, the preparation of a luminescent nanomaterial containing both types of ions would feature novel, exciting optical properties. By exploiting the advantages of both ions, enhanced luminescent properties would be achieved. It is appropriate to think that if lanthanide and transition metal ions, as well as their concentrations, are suitably chosen, a transfer of the energy absorbed by the transition metal to the lanthanide may occur. This energy may be released through a radiative decay by the lanthanide ions. This may be enable an increased excitation of lanthanide ions and consequently a greater probability of radiative decay.
In Figure 1.13, PL and photoluminescence excitation(PLE) spectra of trivalent chromium in two different crystalline host materials (figure 1.13a), and emission spectra of luminescent lanthanide complexes in solution (figure 1.13b) are shown to visualise the experimental differences between TM and lanthanides.

All the differences between transition metal and lanthanide ions can be summarised into seven main points:

i) The electronic transitions in TM ions involve electrons in 3d orbitals, while in lanthanide ions, they involve electrons in f orbitals.

ii) d–orbitals are bonding orbitals so they strongly interact with the lattice.

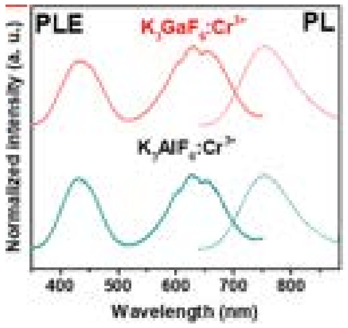

(a) PLE and PL spectra of $K_3Al_{0.97}F_6$:0.03 Cr^{3+} and $K_3Ga_{0.97}F_6$:0.03 Cr^{3+}.[37]

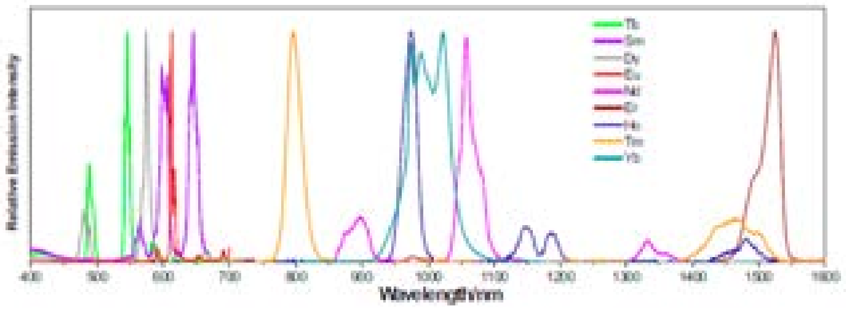

(b) Normalized emission spectra of luminescent lanthanide complexes in solution.[38]

Figure 1.13: Comparison between sharp emission bands (< 100 nm) with broad trivalent chromium bands.

f–orbitals are shielded from the surrounding environment, so they display weak vibronic coupling.

iii) Lanthanides exhibit sharper optical bands than those of transition metals.

iv) The positions of the optical bands depend on their chemical environment in the TM ions, while as the host material varies, those of the Ln^{3+} remain almost unchanged (the extent of shifts is up to a few hundred wavenumbers at most).

v) The absorption cross section is greater in TM ions than in Ln^{3+}.

vi) The ionic radii of transition metal are smaller than those of lanthanides.

vii) Emission of lanthanides arise from many spin-forbidden f-f transitions. While the deviations of the spin multiplicity selection rule is little deviated in transition metals of the first series.

viii) TM ions of the first series preferentially occupy octahedrally and tetrahedrally coordinated crystallographic sites, Ln^{3+} typically prefer high-coordination sites (CN equal or larger than 6).

ix) Ln^{3+} exhibit longer PL lifetimes compared to transition metal ions.

1.1.4 Applications

Luminescent inorganic nanomaterials surround anybody in their everyday life. They play crucial roles in diverse applications ranging from lighting and display to biological labeling and optoelectronic conversion.

Lighting and displays

Display technology has gradually but profoundly shaped the lifestyle of human beings, which is widely recognized as an indispensable part of the modern world. Smartphones, tablets, computer monitors, televisions, data projectors are all examples of display devices that are part of the daily life of anyone nowadays. Lighting and displays is one of the main application of inorganic solid-state phosphors. The luminescence of many semiconductor lasers and some light-emitting diode arises from recombination of an electron in the conduction band with a hole in the valence band. Emerging nanomaterials offers a new class of phosphors that may promote advancing towards devices with higher efficiency and innovative properties, as example they may provide more colors by simply adjusting the size of the nanoparticles as mentioned for quantum dots. In recent years, quantum dot light-emitting diode (QLED) screens have been increasingly marketed. Since they are cost-effective electroluminescence devices ideal for large-area displays and lighting applications. Another emerging class of nanomaterials that exhibit useful properties for lighting and display is perovskite light-emitting diode. Display based on this materials would provide cleaner colors and could potentially be much brighter and more energy efficient compared to current-generation organic light-emitting diode (OLED) screens. The efficiency of perovskite LEDs match that of OLEDs, but they can be further optimised. Hence, they could be implemented in many displays and lighting in the future to create both improved aesthetics and lower energy consumption.[39–41]

Photovoltaic systems

Luminescent inorganic materials are also prominent for photovoltaic application. Photovoltaic systems produce clean, reliable energy without consuming fossil fuels. They produce electrical power by converting solar radiation into direct current electricity. Photovoltaic energy is the third renewable energy source, representing approximately 15% of them. PV systems can be used in a wide variety of applications such as building-integrated photovoltaic systems, solar-powered cars, backup systems for critical equipment, and stand-alone devices (e.g., emergency telephones, and traffic signs). Photovoltaic solar cells are multi-layers semiconductor-based devices which absorbs sunlight and transports the resulting charge carriers to electrical contacts. Conventional solar cells, however, are only able to achieve 31% conversion efficiency. Inorganic nanomaterials could allow us to overcome this limit, converting a greater quantity of solar energy into electrical energy. To enhance power-conversion efficiency in solar cells, rare earths-doped phosphors and QDs for examples can be employed as solar concentrators and downshifting layers. The addition of nanoparticles in PV systems may also enhance the effective optical path, resulting in the highest possible solar energy absorption. Silicon-based PVs are the most common, and they may be modifying using carbon dots, graphene quantum dots as example.

But also SnS, CdTe, Cu(In,Ga)Se_2, and $CH_3NH_3PbI_3$ nanoparticles are emerging components of solar cells.[42–44]

Sensing

Luminescence is also useful for future sensing applications, both physical and chemical. It could be used, in principle, to monitor parameters of interest in medicine, industry, research, and the environment. The luminescent properties of a material (fluorescence or phosphorescence intensity, excitation and/or emission wavelength, emission lifetime) respond to the presence of some species in their immediate environment, or to a specific pH range. The nanomaterial is so used as chemical probe. The luminescent properties of the material can change also due to physical condition, like temperature, pressure, and mechanical force. Conventional temperature and pressure sensors present some limitations, like the inability in measuring temperature at sub-micrometric scale spatial resolution, low sensitivity and flexibility. In this context, luminescence nanothermometry, and recently also nanomanometry, stand out. The use of luminescent nanosensors enables to measure indirectly a physical condition of a system of interest through the minimal interaction between system and probe. In addition, remote sensing can be performed. The detection of temperature and pressure at nanoscale is relevant in the fields of nanomedicine, microelectronics, nanofluidics and catalytic reactions.

Temperature plays a crucial role in medical care, a change of temperature is the result of cellular responses to various states of the body, such as inflammation. For this reason, the cancerous cell temperature is often higher than normal cell. It would therefore be ideal to be able to measure these variations with minimal interaction with the biological system, and with a semi-invasive ways such as oral and injection. In the future it will probably be possible with the advancement of research in the field of luminescent nanomaterials.[45, 46]

The potential use of nanomanometry in nanomedicine is the detection of pressure changes in a specific area of a biological system. For example, high tumor interstitial fluid pressure is a fundamental feature of cancer biology and represents a major obstacle to successful cancer treatment. A nanoscale sensor could allow the accurate detection of the area affected by increased pressure.

Biomedical imaging and therapy

Luminescent nanomaterials have also a potential in biomedical imaging and therapy. Biomedical imaging is a powerful tool for visualizing the internal organs of the body, as well as specific molecular pathways, particularly those that play key roles in disease processes in living animals and humans. Bioimaging techniques involve the use of sophisticated bioimaging probes. Currently, they have poor sensitivity, specificity, and targeting, hampering the clinical application of bioimaging. Therefore, efforts are currently being undertaken to develop optimal bioimaging probes with increased sensitivity, specificity, and signal–to –noise ratio and spatial resolution. Biomedical imaging could help to diagnose fatal diseases such as cancer in their early stages that could lead to more effective treatments.[47, 48] The use of nanoprobes in optical bioimaging is bringing excellent results despite the numerous complexities of biological systems. Nano–sized contrast agent often fail in vivo tests

since nanoparticles have to overcome several barriers like the mononuclear phagocyte system, the aspecific distribution within the human body, and hemorheological limitations (inefficient dynamics of nanoparticles in blood vessels).[47, 48]
Luminescent nanomaterials for biomedical applications should meet very stringent optical requirements, such as high brightness together with photon absorption and emission capabilities in the near-infrared (NIR) spectral range of optical transparency windows (NIR–I: 680 –950 nm, NIR –II: 1000–1350 nm, NIR –III: 1500 –1800 nm), they are shown in Figure 1.14.

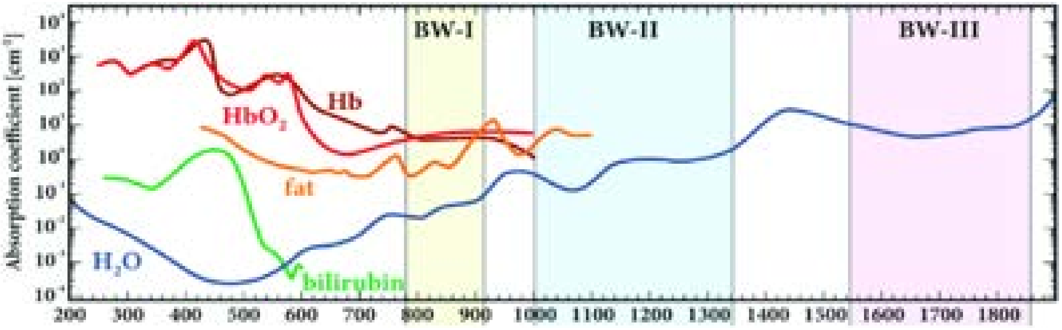

Figure 1.14: Dependence plot of absorption coefficients of some major tissue components on wavelength spanning over three biological windows.[49]

These three wavelength ranges are the optical windows of living tissues, where absorption and scattering of photons by water, and the various components of blood, biological cells, and tissues, are minimal. In the second region there is also less autofluorescence of biological tissues. Hence, the performance of luminescent nanomaterials can be significantly influenced especially by the absorption of water (several broad bands) contained in biological tissue. Lanthanides are the doping ions most used for biomedical applications, because –as explained in the section 1.1.3 –they exhibit narrow and localized bands in specific areas of the electromagnetic spectrum depending on the selected ion. Their widespread use in this medical field is therefore linked to this characteristic which allows one or more luminescent signals to be obtained exactly localized in these areas. Lanthanide ions exhibiting emission in the biological windows are: ytterbium Yb3+, which dominant emission is around 1030 nm; neodymium Nd3+, which displays a band centred in the first optical window and another one more intense located in the second optical window (1020-1100 nm); Dysprosium Dy3+, which exhibits two emission bands in the second optical window, one at the beginning and one located at about half of the transparent zone; finally erbium Er3+ is the only lanthanide to exhibit an emission band in the third optical window.
Luminescent nanomaterials play also a key role in advancing in therapy. Phototherapy is the use of light in the treatment of skin diseases that show improvement upon exposure to natural sunlight or man-made lamps. These lamps are coated with luminescent material by using a suspension of phosphor powder particles, commonly inorganic borates doped with rare earths.[50]

However, most research efforts are directed towards effective therapies against tumors. As described above, lanthanide–doped nanoparticles are promising imaging tools to identify the locations of cancers. Therefore, in recent years the development of Ln–doped NPs combined with therapeutic agents (chemotherapeutic drugs) has been hypothesized, in order to obtain multifunctional probes for imaging-guided and tumor-targeted therapies. In this context, photothermal therapy (PTT) is a therapeutic treatment that has nowadays attracted massive attention. It is one of the latest therapeutic methods to treat cancer that converts non-ionizing near-infrared (NIR) light into heat leading to thermal ablation of cancer cells. PTT is less invasive, compared to chemotherapy or surgery, and potentially very effective. For this purpose, nanomaterials should have high optical absorption capacity in the near infrared region and photothermal conversion. Graphene-based nanomaterials and Ln-doped rare earth nanoparticles seems to be two ideal candidates for photothermal therapy.[51, 52]

1.2 Host Lattice Materials

In the previous paragraphs the characteristics of lanthanide ions and transition metals, their more or less marked interaction with the host crystalline material, as well as their strong points have been illustrated. It is first necessary to define which luminescent ions has been chosen for the experimental project in order to better explain the choice of the host crystalline material.

This thesis project relies on the chemistry behind the synthesis of luminescent nanomaterials, while keeping a look towards the potential applications and usefulness that the developed material could have. For this reason, hypothesising a future use of the synthesised nanoparticles in the field of nanomedicine, and more precisely as biomedical sensors, the selected lanthanide ion was trivalent neodymium. This ion is known to give rise to three bands within the NIR region from 1000 nm to 1400 nm when excited with EM waves with wavelength 750–850 nm (common infrared excitation lasers are at 785 and 805 nm). Therefore, the region of the EM spectrum in which neodymium exhibits its photoluminescence corresponds to the second biological window. Consequently, Nd (III) is one of the most attractive lanthanide ions for medical sensing purposes. Electron configuration of neodymium ions is [Xe] $4f^3$ and its luminescence occurs by radiative depopulation of $^4F_{\frac{3}{2}}$.

Concerning transition metals both the emission range of luminescence and the rate of temperature quenching of the luminescence can be modulated by changing the type of matrix material used since they are sensitive to the strength of the crystal field. The emission of transition metals is more susceptible to physical change in the surrounding environment of the ion itself compared to Ln ions. It stands to reason that a probe based on transition metals has an enhanced sensitivity to such variations (like pressure and temperature), and consequently a better performing sensor. Therefore, a crystalline material acting as host for transition metals would be promising in the field of sensing in general, while one doped with neodymium would be promising in the field of biomedical sensing. From these considerations emerged the idea of making a nanomaterial that combined both luminescent ions in order to exploit the strengths of both active centres.

Transition metals have higher absorption cross–sections than those corresponding to f-f transitions of Ln(III). It means that a TM ion has more probability to absorb (and so to be excited by) one photon compared to a lanthanide ion. The greater absorption cross–section of TM can be useful for improving the emission of lanthanides. If a material containing both types of luminescent ions is impinged by a radiation resonant with the d-d electronic transitions, TM ions will absorb a fair amount of incident photons and then they may transfer this energy to nearby ions, lanthanide ions, which may release that energy emitting radiations. Therefore, each transition metal ion acts as sensitiser–chromophore. It harvests the incident light just like organic ligands used as "antennas" in luminescent coordination compounds. Lanthanide ions act as activators by accepting the energy from the sensitiser. Upon the fulfilment of certain conditions related to the nature of the involved luminescent ions and host material this succession of events can happen.

Firstly, the host material should be able to efficiently contains both types of ions. The crystalline matrix should feature sites that are suitable for both Ln and TM ions (appropriate coordination number), and the cations occupying those sites should have ionic radii close to the ones of Ln and TM ions to minimise lattice distortion. Ionic radii discrepancy percentage between the doped ions and matrix cations should be as small as possible, conventionally under $\pm 15\%$.

Secondly, the host material should be as transparent as possible at the wavelengths of interest (both absorption and emission) to minimize spurious absorption and optical scattering losses.

Thirdly, the host materials should be physicochemically stable over time. The composition, surface chemistry (functional groups and charge) and lack of aggregation should be preserved during storage and/or experiments even with changes in environental conditions.

Last condition related to the crystalline matrix is that it should have low lattice phonon energies to minimise all non–radiative processes involving phonon emission, less than 600 cm^{-1}.[53] If the phonon energy of the host material is low, the probability of non–radiative vibronic transitions is correspondingly low because this relaxation will require the assistance of several phonons.

Regarding transition metal and Ln $^{3+}$ ions, they should be in the same oxidation state to ensure charge neutrality of the material. In addition, the sensitiser and activator should have excited state levels of approximately equal energy (i.e., resonant) above their ground states, or rather, the excited state level of the energy acceptor should be slightly lower than that of the energy donor. Perfect resonance ensures the highest efficiency of energy transfer between ions. However, this is a two-way street and back-energy transfer from the activator to the sensitiser can also occur. As such, in chemistry of coordination compounds there is a rule of thumb to effectively preclude back energy transfer (from acceptor to donor) at room temperature and consequently ensure good energy transfer between a chromophore and a lanthanide ions, namely energy gap between two energy levels should be at least 2000 cm $^{-1}$. This threshold can be approximately calculated as

$$\Delta E = 10 k_B T \tag{1.19}$$

where k_B is the Boltzmann constant 8.6173 $10^{-5} eV\ K^{-1}$ and T the temperature (in

K).[54]
A qualitative schematic representation of energy transfer between a sensitiser with three excited energy levels and an acceptor with excited energy level approaching the lowest excited energy level of the sensitiser is shown in Figure 1.15. The representation was created based on the presumed relative positions of the levels of Cr(III) and Nd(III) in fluoride host materials, but it is not to scale.

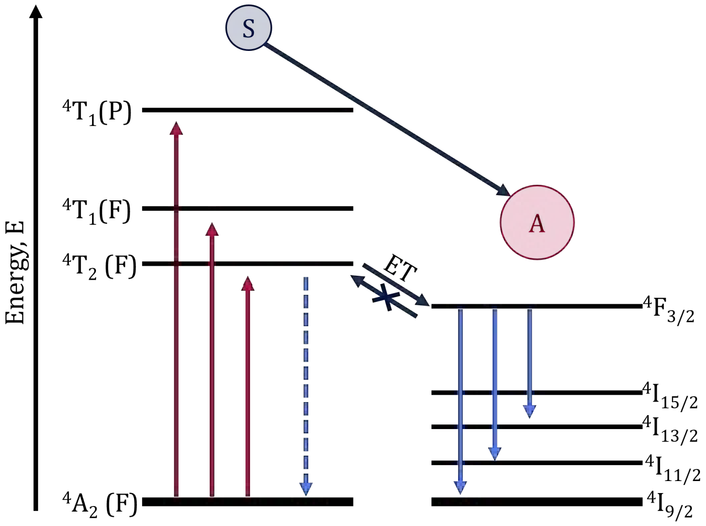

Figure 1.15: Schematic representation of ET (out of scale) between a sensitiser ions with three excited energy levels and an acceptor ions with four excited energy levels. Pink and light blue arrows mark photoexcitation and emission respectively. Dashed arrow indicates the quenched emission of sensitiser.

Energy transfer can occur via radiative or non–radiative processes:

i) In a radiative ET there is no actual interaction between donor (sensitiser) and acceptor (activator). Donors absorb the incident radiations, then their emitted photons will be absorbed by acceptors. This mechanism implies the absorption by lanthanide ions, thereby reasonably this would not bring great advantages.

ii) In a non–radiative ET depending on the spatial separation between sensitiser and activator two major mechanisms can occur.

   - Dexter exchange mechanism, wherein the excitation energy is transferred via direct electron transfer exchange between sensitiser and activator since they are closely spaced ($\sim$ 10 Å).
   - Förster resonance mechanism, the excitation energy of the donor is transferred to the acceptor through a multi–dipole coupling interaction that is distance–dependent. This process usually occurs when ions are about 1–10 nm apart from each other.[55, 56]

A schematic representation of three energy transfer mechanisms is reported in Figure 1.16.

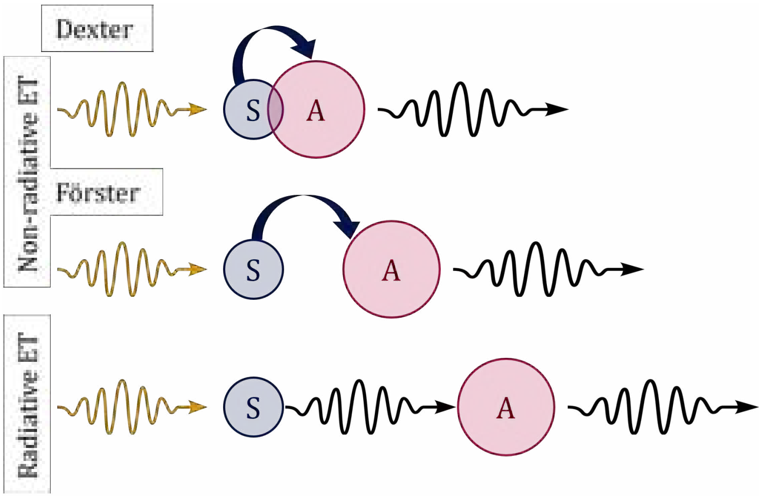

Figure 1.16: Schematic illustration of energy transfer through electron transfer exchange, multipolar interactions and donor emission - acceptor reabsorption. S and A stand for sensitiser and activator; wavy arrows represent EM waves. The size of sensitiser is smaller than acceptor to abide by size ratio between Cr(III) and Nd(III), i.e. about 5:8.

The probability of energy transfer W_{DA} between an excited donor (sensitiser) and a relaxed acceptor (activator) A, according to Fermi's golden rule, is proportional to the degree of spectral overlap, i.e. energy density of initial and final state $\varrho(E)$.[57]

$$\begin{aligned} W_{DA} &= \frac{2\pi}{\hbar} \; |< D^*, A|\hat{H}_{DA}|D, A^* > |^2 \;\; \varrho(E) \\ \varrho(E) &= \int f_{em}^{D}(E) f_{ex}^{A}\,(E)\,dE \end{aligned} \tag{1.20}$$

where $| < D^*, A|\hat{H}'_{DA}|D, A^* > |^2$ is the square of the transition matrix element, $\hat{H}'$ is the perturbed Hamiltonian operator, note that asterisk denotes excited states. The spectral overlap zone in terms of intensity is represented by the yellow shaded region in Figure 1.17.

The higher is the degree of overlap between the emission of the donor and the excitation of the acceptor, the greater is the probability that the energy transfer will occur. The spatial separation between the ions involved in energy transfer can be tuned by their concentration. Both of them should be high enough to ensure an appreciable transfer probability without exceeding the quenching concentration threshold. Above all, the concentration of the activator should not be excessive in order to prevent the migration of energy through the host matrix until entrapment in a crystalline defect. The concentration of sensitiser is usually higher than that of the activator.

If luminescence sensing is targeted, the emission bands of TMs and Lanthanide ions should have reduced overlap so to avoid difficulties in the deconvolution of signals for sensing purposes. This condition is usually readily satisfied in the system of interest

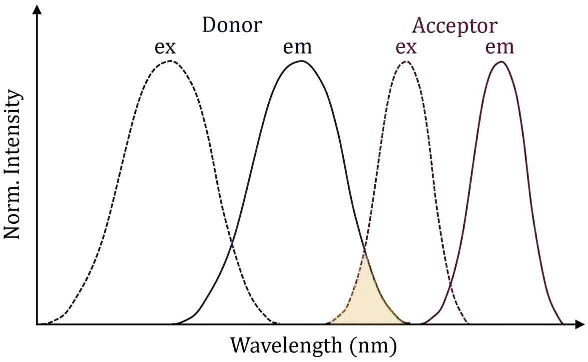

Figure 1.17: Schematic representation of the Förster resonance energy transfer spectral overlap integral (shown in yellow shadow). Donor emission (blue solid line) and acceptor excitation (pink dashed line).

for this thesis since the emission of transition metals rarely occurs in correspondence with the second biological window where the neodymium bands are found.
Finally, there are also basic requirements related to the future potential application of the material in nanomedicine: the wavelength of excitation should be red light or NIR radiation and the nanoparticle should be dispersible in water. The constraint in the excitation radiation is associated to the penetration depth into the human skin. Red light penetrates deeper than blue light, it is extinguished at about 4–5 mm beneath the surface of the skin, while NIR radiation reaches deeper, with penetration depths in the order of 1 cm or more.[58]

The choice of the transition metal and the suitable matrix is a non-trivial task.
The transition metal apparently having the previous ideal features to act as sensitiser towards neodymium ions is trivalent chromium. The research field of TM-based luminescence sensing is dominated by sensors composed of chromium or manganese (Mn^{2+}, Mn^{3+}, Mn^{4+}, and Mn^{5+}). Trivalent manganese is not the most thermodynamically favourable oxidation state, its use is in fact hindered as it is difficult to stabilise. However, the primacy belongs to trivalent chromium, it is the most used TM mainly thanks to its high emission intensity and its better temperature dependence compared to the other ions. Although hexavalent chromium is carcinogenic if swallowed or absorbed through the skin, our diet requires small quantities of chromium (III), actually this ion plays a role in regulation of blood glucose levels. The applicability of the ion in biological systems still remains controversial, but theoretically there should be no critical issues related to its use. Regardless, when a new material doped with Cr(III) is developed, its cytotoxicity should be evaluated on a case-by-case basis.
Trivalent chromium preferentially occupies octahedral crystallographic positions. Its luminescence occurs by radiative depopulation of the ^2E and/or $^4T_2$ energy levels. According to the Tanabe-Sugano diagram for the d^3 electron configuration, an increase in crystal field splitting causes an increase in the $^4T_2$ level energy, see Figure 1.12. Therefore, the energy of $^4T_2$ level strongly depends on the local crystal field affecting the luminescence properties of Cr(III) ions.

To recapitulate, the crystalline matrix should have low phonon energies to minimise non-radiative decay pathways, low refractive index and a trivalent cation with ionic radius between 0.615 Å(Cr(III)) and 0.983 Å(Nd(III)) lying an octahedral site.[59] Considering phonon as quantum of lattice vibrational energy, neglecting anharmonicity of vibrations, the energy of a phonon can be written as $E = \hbar\omega$ where ω is the angular frequency of the phonon. In the table below, the maximum phonon energies ($\hbar\omega_{max}$) of the most used host crystalline inorganic matrices for lanthanide and/or transition metals are reported. Note that the reported maximum phonon energies refer to bulk materials, not to their nanoscale counterparts. Over the shrinkage from bulk to nanoscale, the maximum phonon frequency may change, but an overall trend has not yet been determined.[20, 60–67]

Host material	**Highest phonon energy (cm^{-1})**
Borate glasses	1400
Phosphate glass (P_2O_5)	1200
Silica glass (SiO_2)	1100
Lanthanum phosphate ($LaPO_4$)	1050
Simple oxides (e.g La_2O_3–Ga_2O_3)	550–900
Yttrium aluminium garnet ($Y_3Al_5O_{12}$)	800
Titanates ($Ti_2O_7{}^{6-}$)	800
Yttrium orthovanadate (YVO_4)	600
Fluoride glass (e.g. $BaZrF_6$)	550–580
Lithium yttrium fluoride ($LiYF_4$)	570
Non-oxide chalcogenide glass (e.g.As_2S_3)	360 –400
Sodium yttrium fluoride ($NaYF_4$)	420
Potassium indium fluoride (K_3InF_6)	370
Barium fluoride (BaF_2)	330
Calcium fluoride (CaF_2)	320
Lanthanum trifluoride (LaF_3)	300

Table 1.2: The maximum vibrational phonon energies of commonly used inorganic host materials for lanthanide and transition metals.

From data in Table 1.2, it appears clear that the host materials for lanthanides and/or transition metals with lower phonon energies are fluoride-based. Fluorides have refractive index values between 1.4 and 1.5 with wavelength of the incident light of 600–900 nm (λ_{ex} of Cr(III) and Nd(III) belongs this range), so they are transparent matrices.

Unfortunately, sodium yttrium fluoride ($NaYF_4$), barium fluoride (BaF_2), calcium fluoride (CaF_2), lanthanum trifluoride (LaF_3) are all non-versatile host materials for the incorporation of both chromium and neodymium ions. They are suitable crystalline materials for doping with lanthanides as the substituted cations occupy sites with high coordination numbers: yttrium is nine-coordinated in α-$NaYF_4$(cubic phase) and eight-coordinated β-$NaYF_4$(hexagonal phase); calcium and barium are eight-coordinated in CaF_2 and in BaF_2 and lanthanum is nine-coordinated in LaF_3.

In Figure 1.18 the crystal structure of β-$NaYF_4$ (a), α-$NaYF_4$ (b) and CaF_2 (c) standard orientation.

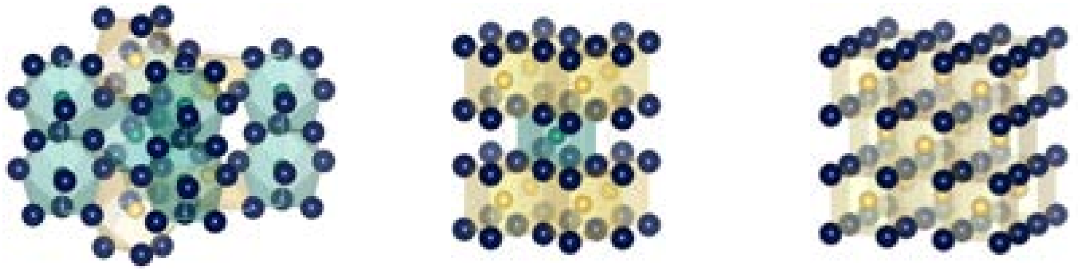

(a) β-$NaYF_4$. (b) α-$NaYF_4$. (c) Cubic CaF_2.

Figure 1.18: Polyhedral views of crystal structure of three common host materials in standard orientation. Sodium and calcium in yellow, fluorine in blue and ytterbium in water green.

Fortunately, there is a family of fluorides that seems to possess all the ideal characteristics listed above, namely ternary fluorides with chemical formulas A_3BF_6, $A_2A'BF_6$ and $AA''BF_6$ where A is an alkali metal or Ag^{3+}, A' and A" an alkaline earth metals and B a post-transition metal (Al, Ga, In or Tl). The table 1.3 shows the chemical compositions of the possible fluorides belonging to this family for which there are references in the scientific literature. Where possible, the presence of doping ions is also shown.[68–71]

Chemical formula	**Dopant ion**	**Ref.**
Rb_2KInF_6	Ce^{3+}	[72]
K_2NaInF_6	Ce^{3+}	[72]
K_3InF_6	Ce^{3+}	[72]
Ag_3ScF_6	—	[73]
Ag_3AlF_6	—	[73]
Ag_3GaF_6	—	[73]
Ag_3InF_6	—	[73]
Ag_3TlF_6	—	[73]
Rb_3TlF_6	—	[73]
Na_3AlF_6	Cr^{3+}	[74]
Na_3GaF_6	Cr^{3+}	[74]
Na_3ScF_6	Cr^{3+}	[74]
Na_3InF_6	Cr^{3+}	[74]
$Na_3Li_3In_2F_{12}$	Cr^{3+}	[75–77]
K_2LiGaF_6	Cr^{3+}	[76]
$CsZnInF_6$	—	[78]
$RbZnInF_6$	—	[78]
$RbMgInF_6$	—	[78]
K_3InF_6	Er^{3+}, Er^{3+}/Yb^{3+}, Eu^{3+} and Tb^{3+}	[67]

Li_3InF_6	——	[79, 80]
Li_3GaF_6	——	[80]
Li_3AlF_6	——	[80]
Li_3CrF_6	——	[80]

Table 1.3: Known ternary fluorides with formula A_3BF_6, $A_2A'\ BF_6$ or $AA''\ BF_6$ and where possible, the used dopant ions.

The best photoluminescence performance of chromium (III) were achieved with bulk Na_3ScF_6 and Na_3InF_6. Doping with several lanthanides of metal hexafluoroindate A_3InF_6 was proven. For these reasons, the best candidate among this series of compounds to be studied as a versatile material for lanthanides and transition metals on the nanoscale seems to be sodium indium fluoride Na_3InF_6.

The thermodynamically most stable phase of sodium indium fluoride is monoclinic, space group $P2_1/c$ (number 14). In Figure 1.19 the structure of sodium indium fluoride, showing the corner connected InF_6 and NaF_6 octahedra and the mono-capped trigonal prism located between these octahedra. The crystal structure can be considered as a double perovskite form of $A_2A'BF_6$ and from this cryolite A_3BX_6 structure types are derived by a cationic ordering and are based on a double perovskite cell but with a lower symmetry. Therefore, Na_3InF_6 is isomorphous to cryolite Na_3AlF_6, an uncommon mineral.[81] The reported lattice constants for Na_3InF_6 in bulk are: 5.56418 for the a-parameter, 5.82870 for the b-parameter, 9.70228 for the c-parameter, and 123.4450 °for the β angle, considering b as unique axis.

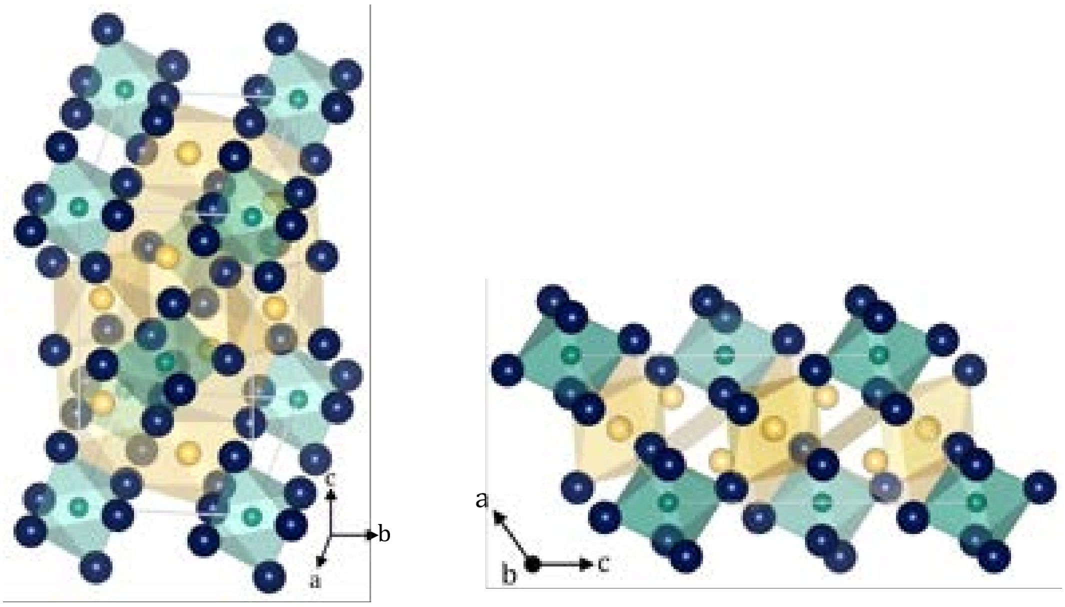

(a) Standard orientation.

(b) View along the b-axis.

Figure 1.19: Polyhedral views of crystal structure of Na_3InF_6 in two different orientations. Na^+ in yellow, In^{3+} in water green and F^- in blue.

The structure comprises alternating corner sharing InF_6 and NaF_6 octahedra, so each hexacoordinated indium ion share corners with six equivalent NaF_6 octahedra. Sodium cations, besides six-coordinated site, occupy also an interstitial site with a 7-coordinate geometry in which Na^+ is bonded to seven F^{-1} atoms. Two crystallographic positions of sodium cations are shown in Figure 1.20. In a single base-centered monoclinic unit cell, with indium ions at eight corners and at the centers of two sides parallel to bc plane, there are four NaF_6 octahedra and four mono-capped trigonal prism NaF_7. Fluorine F^- occupy three inequivalent sites, tetra or penta coordinated.

(a) NaF_6 octahedra.

(b) Mono-capped trigonal prism NaF_7.

Figure 1.20: Polihedral view of local geometrical coordination environments of sodium cations in two different orientations.

The ionic radius of In(III) in VI-fold coordination is 0.8 , it is quite versatile from the point of view of doping it with lanthanide or transition metal ions since the octahedral site is suitable to host both cations. The Shannon radius of In(III) differs from that of Cr(III) and Nd(III) of about 23% in both situations. Cr(III) should shrinks and Nd(III) should expand Na_3InF_6 lattice parameters. It is therefore probable that the introduction of such ions requires some structural rearrangements in terms of displacement of the ions from their ideal crystallographic positions, and this may impart variations in the photoluminescence of the doping ions, especially of chromium.

Therefore, sodium indium fluoride represents a valid candidate as versatile crystalline host material for the co-doping of chromium and neodymium. Since it has never been created at the nanometric scale, no protocols are available in scientific literature. Fortunately, in the past numerous investigations have been carried out on the chemistry of fluorine F^- which have allowed an advanced understanding of the structure and reactivity of fluorides, especially in bulk, but also at the nanoscale.

1.3 Preparation of Fluoride-based Nanomaterials

The past decades have witnessed an increased interest in the nanochemistry of the fluoride compounds due to the prospective applications of nanofluoride materials in photonics, catalysis, biosensing and high temperature superconductor devices. This section summarizes information about the most common synthetic methods of inorganic fluorides at the nanoscale. There is a huge variety of existing methods to synthesize fluoride nanoparticles usually classified into top-down and bottom-up. Each of them has its own advantages and drawbacks. Because of extremely large volume of information on this topic, this section focuses on the description of bottom-up processes being the most commonly used. Preparation of fluoride-based nanoparticles can be carried out by physical and chemical methods. Actually, also in physical methods the formation of the nanophases is accompanied with the chemical reactions, like in ultrasonication or microwave-assisted heating. Bottom-up approaches are so defined given that atoms, ions and molecules are assembled together into increasingly larger structures until they reach nanometric sizes ($<$ 100 nm). These methods often result in the formation of colloids in organic medium. Nanoparticles form through a complex sequence of several stages that result in colloidal self-assembly. When a system, consisting in reactants and solvent(s), is in a non-equilibrium condition, like a supersaturated solution (or very close to the critical concentration) it spontaneously forms a new phase. The ions dissolved in solution are in constant motion and begin to aggregate, forming small nuclei of this new phase. This first stage consists in the formation of small groups of ions/molecules due to condensation and it is called homogeneous nucleation. The nucleation can also be heterogeneous, i.e. taking place on external substances such as crystal seeds, impurities and dislocations (lower energy demand). This stage is pretty relevant as it determines both the crystalline structure and the subsequent sizes.The preformed nuclei can act as crystallization centers, ions in solution can be deposited on their surface by diffusion, becoming incorporated into the structure of the crystal lattice. The crystal formation proceeds by the assembly of clusters or nanostructures with discrete sizes through coalescence, oriented attachment and Ostwald ripening. Therefore, small masses combine to form larger and more stable objects (with or without preferences in the orientation of the crystal lattice at the grain boundary) or dissolve and redeposit on larger masses. The propagation of this new metastable phase is thus the growth of crystals. The rate of nano-particle growth is influenced by many factors: viscosity of the liquid, amount of material, particle-particle aggregation. All colloidal methods are therefore based on these two fundamental stages: nucleation and growth of nanocrystals. In the paragraphs below the most commonly used chemical and physical methods to synthesize metal nanofluorides (binary and ternary) are illustrated.[82, 83]

1.3.1 Thermal decomposition method

The thermal decomposition method for synthesizing fluoride nanoparticles involves the decomposition of precursor compounds at elevated temperatures. The general strategy consists in the combination of organometallic compounds or inorganic salts at sufficiently high temperatures and/or concentrations in the presence of stabilisers or surfactant molecules. The synthesis involves a fast nucleation followed by slower growth of the existing nuclei. Depending on the introduction of precursors the synthesis technique can be defined:

i) Hot injection, precursors are quickly injected into the reaction media at relatively high temperatures, usually 100-370 °C.

ii) Heating up,precursors are injected into the reaction media at room temperature and the setup is quickly heated.

Since the reaction temperature is high and unwanted reactions may occur, such as oxidation of reagents, the protocols require oxygen-free atmosphere, so an inert gas atmosphere such as nitrogen and argon. The reaction mixture, besides reagents and solvent(s), often contains additives to manipulate the size and shape of nanoparticles. They can be coordinating solvent or additional molecules that control the nucleation and growth rates by dynamically binding to the surface of the nanoparticles and to the constituent elements in solution. This molecules have a long non-polar chain and an head group able to bind to the nanoparticle surface. The polar group contains atoms having unshared electron pairs like nitrogen, oxygen, sulfur and phosphorus. These atoms act as donor of electrons forming coordinating bonds with metal atoms or ions on the surface of nanocrystals. Precursors are often metal trifluoroacetate $M(CF_3COO^-)_x$ or acetate $M(CH_3COO^-)_x$, fluoro ammonium complexes, metal nitrate $M(NO_3)_x$ and highboiling organic solvent/surfactant are commonly octadecene (ODE), oleic acid (OA), amine derivatives of the oleic acid (oleylamine, OAm), benzylamine or their mixture. The prepared nanocrystals are often easily redispersed in various nonpolar organic solvents such as hexane, toluene, and chloroform being organic ligands on the surface of the nanofluorides.[83–85]

1.3.2 Co-precipitation method

Co-precipitation methods are generally easy to use and inexpensive, but usually require additional washing of the product from matrix anions making the protocol laborious and time consuming. As for the approach illustrated previously, the solvents used are usually organic, but water could also be used as a reaction medium. Fluorides, precipitated from water solutions, usually contain large amount of adsorbed water that can cause their pyrohydrolysis (thermal process that exploits oxygen contains in water). To avoid this undesidered process, the samples have to be heated under inert or fluorinating atmosphere to remove adsorbed water molecules and OH-groups from the surface of the particles. The agglomeration of small nanoparticles precipitated from solutions is practically inevitable in the absence of a stabiliser. The approach to stabilise nanoparticles in colloids is also in this method the addition of capping ligands like surfactants and polymers, thus exploiting the steric repulsion between the coated particles. Besides the examples reported in the previous paragraph, ethylenediaminetetraacetic acid (EDTA) and dipicolinate (DPA) can be used as stabiliser. Precursors are usually ammonium fluorides (NH_4F and NH_4HF_2), metal fluoride salts (NaF, LiF, KF), metal tetrafluoroborate ($NaBF_4$, KBF_4), fluoride acid (HF), chloride salts (MCl_x) and nitrate salts ($M(NO_3)_x$). The synthetic protocol used in the experimental part of this thesis work was a combination of these two illustrated methods.The nucleation was generated by co-precipitation in a high-boiling binary mixture (mixture of oleic acid and octadecene 2:3 by volume) at 50 °C and subsequently the reaction mixture (under argon atmosphere) was heated to high temperature (290 °C) for the growth of the preformed nuclei. Oleic acid acted not only as a solvent, but also as a coordinating capping agent by binding to the surface (positive charged) of the nanofluorides, effectively controlling nucleation and growth rates. Precursors were $M(CH_3COO^-)_x$ (for indium and neodymium), metal nitrate salt ($Cr(NO_3)_3$, converted into chromium oleate before addition into reaction mixture), ammonium fluoride (NH_4F) and sodium hydroxide (NaOH).[86, 87]

1.3.3 Hydro/Solvothermal method

In hydro/solvothermal method the chemical reactions take place in a closed system where precursors are treated under high pressure and temperature conditions. Most hydrothermal/solvothermal reactions proceed in a sealed reactor, known as an autoclave, a pressure vessel, or a high-pressure bomb. This method is used for crystallization process that would be impossible or pretty difficult in conventional conditions since at elevated temperature the solubility and reactivity of precursors considerably increase. Nanofluorides can also be prepared by hydrothermal treatment of samples already precipitated from the matrix solutions. The protocol usually takes a long time, but once the reaction conditions have been set, no further operator intervention is required. The growth of nanoparticles can also be controlled in this method by adding the stabilizing agent. Frequently used nanofluoride size-controlling agents synthesized by hydrothermal methods are EDTA, cetyltrimethylammonium bromide (CTAB), and polyethylene glycol (PEG). Hydrothermal methods are environmental friendly, but non-aqueous solvents prevents oxygen contamination and also stabilize the particle surfaces and prevent their growth and agglomeration. Solvothermal methods include heating of the reaction mixtures in the suitable solvents in autoclaves at the temperature up to 370 C. In addition to the already mentioned solvents (OA, ODE, OAm), n-heptane, n-(2-hydroxyethyl) ethylenediamine (HEEDA), diethyleneglycol and their mixtures can be used as media for these techniques.[88, 89]

1.3.4 Reversed micelle and microemulsion methods

Fluoride-based nanoparticles are synthesised in colloid nanoreactors (micelle). The surfactant molecules (with ionic or uncharged head) are dissolved in organic solvents to form aggregates that are called as reverse micelles. The term reverse indicates that the core region is polar and non-polar tails of surfactants point towards organic solvent. Reverse micelles are usually nanometer-sized (1-10 nm), but they can encapsulate a fairly large amount of water in their polar core to form a microemulsion (size up to 100 nm). In this synthetic approach the chemical reactions takes place in the aqueous core of the reverse micellar droplets. There are two types of the synthetic methods with the use of reversed micelles with nano or micro sizes:

i) Reagents are contained in different reverse micelles, which are mixed together in the organic medium. The coalescence (droplets fusion) of reverse micelles leads to the exchange of the precursors and the chemical reaction can occur within the droplets. Therefore, nanofluorides are formed inside the hydrophilic nuclei of the micelles.

ii) Reagents are contained in different reverse micelles and in the lyophilic media, thanks to diffusion and exchange processes, the chemical reactions among precursors can take place withind droplets.

Therefore, in both approaches the desired nanoparticles are obtained inside the inverted micelles and precipitate, being insoluble, in the aqueous core. The concentration and nature of the surfactant allow the creation of micelles of various shapes, e.g. cylinders, lamellae, spherolites, etc.
Cyclohexane, n-octane, isooctane, n-heptane are commonly used as the lyophilic phase; aqueous HF, NH_4F, NaF as sources of fluoride anion; and tetrahydrofuran (THF), CTAB as surfactants. N-butanol, 2-octanol and PEG are often used and play the dual role of solvents and co-surfactants.[83, 90, 91]

1.3.5 Microwave-assisted synthesis

Microwave-assisted synthesis is a fast physical approach commonly performed in ionic liquids. Microwave heating allows a shorter time of reaction as compared with the conventional hydrothermal method and thermal decomposition. Microwaves are EM waves with frequencies in the range of 300–300000 MHz, see Figure 1.5, that can interact with matter producing heat in situ. The heat transfer due to microwave absorption is limited to the reaction mixture lowering production cost, in contrast with the conventional methods where heat is transferred from outside to inside. The reactions often take place in ionic liquids that play the dual role of solvent and fluorine source like 1-ethyl-3-methylimidazoliumtetrafluoroborate ($C_6H_{11}BF_4N_2$, EMIM BF_4), 1-methyl-3-octylimidazolium tetrafluoroborate ($C_{12}H_{23}BF_4N_2$, $OMIMBF_4$) and 1-n-butyl-3-methylimidazolium tetrafluoroborate ($C_8H_{15}BF_4N_2$,$[BMIM]BF_4$). Ionic liquids are a class of non-molecular compounds that are composed solely of ions with melting points lower than 100 °C, and they can be also used in mixture with ethylene glycol. When the chemical reactions occur in an ionic liquid, different additives are required to stabilise the nanofluorides like citrate, N,N,N-trimethylglycine (betaine), and lauryldimethylglycine (lauryl betaine). However, the microwave-assisted synthesis can also occur in water or alcohol involving chloride salts, alkali hydroxide and metal tetrafluoroborate as precursors and EDTA as stabiliser.[92–94]

1.3.6 Sonochemical method

Sonochemical method is a physical synthetic approach that exploit ultrasound radiations to generate local extreme and transient conditions. Temperatures above 5000 K and pressures exceeding 1000 atm without the need to heat and pressurize the entire system (like for thermal decomposition and hydro/solvothermal methods) reduce considerably cost. Ultrasound irradiation beyond a certain threshold value involves the agitation of the particles in a liquid medium and the development of a series of chemical reactions, in particular inducing the formation of (very reactive) radical species. Sonochemical synthesis is related to the cavitation phenomenon, which depends on the ultrasound settings, the type of liquid, the temperature and the pressure. It has been shown that cavitation is induced by high frequency sonic waves, in the range 16 kHz - 100 MHz. This phenomenon consists in the formation of several microbubbles in the liquid, which when they explode or implode/collapse cause the release of a large amount of energy. As a result, pressure and temperature increase locally for a few moments, forming hot spots in cold liquids. This phenomenon occurs when the pressure inside a liquid drops sufficiently below the vapor pressure of the liquid itself. Often the pH of the reaction mixture also plays an important role in the synthesis. Aqueous or alcoholic solvents are the most used, and the samples obtained must subsequently undergo a calcination process.[95–97]

1.4 Post-Synthetic Surface Modification

Post-synthesis surface modification allows for fine-tuning and tailoring of the properties and functionalities of the nanoparticles for specific applications. Nanoparticles synthesized with the colloidal approaches described in the previous section are usually covered by some amphiphilic molecules (ligands). Ligands play a very important role during synthesis as they control the nucleation and growth processes. After synthesis, they provide greater colloidal stability and often also play a protective role against unwanted chemical reactions or interactions with the environment (e.g. pH). The surface–ligand interactions can also result in changes in the electronic or optical properties of nanoparticles due to charge redistribution and polarization effects on the surface.

Furthermore, ligands can be selected to impart compatibility with biological systems to the nanomaterial. Some ligands may also possess additional functional groups (e.g., amino, thiol, carboxyl) that allow the bonding to secondary molecules like antibodies, proteins, carbohydrates and nucleic acids. Surface modification strategies include, besides the formation of organic coatings, the growth of inorganic shells (single or multiple) which can be amorphous (silica or titania) or crystalline (same or different composition of the core). The most commonly used post-synthesis surface modifications are illustrated below.[98–100]

1.4.1 Organic coatings

Organic coatings can be made up of either small organic compounds, large polymers with adjustable polarity, or other functional biomolecules that enrich the nanoparticles with additional properties. Small organic compounds are for examples oleic acid. oleylamine and trisodium citrate. The appropriate choice of ligands plays a critical role in the structure, colloidal stability, function and intended applications of nanoparticles. Two main parameters should be taken into account in the design of the surface of nanomaterials:

i) The nature and strength of the bond between the ligand and the surface of nanoparticles. The strength of ligand binding is essential for the long-term colloidal stability of nanoparticles. If the affinity between surface and ligands is weak, nanoparticles should be dried or stored in a medium containing a high excess of ligands. Ligands can be multidentate (like EDTA and citrate), which usually display an increased binding strength having multiple anchoring points.

ii) The environment for which nanoparticles are designed. It may be necessary to disperse the nanoparticles in aqueous mediums with different pH values, in buffers, in biological or organic media. Biological applications limits the choice of ligands to those that are biocompatible, noncytotoxic, and remain strongly bound to the nanoparticle surface. The ligands in this case may also have targeting and drug delivery abilities, or enabling the self-assembly of the nanoparticles in an orderly manner. The terminal groups of the ligands may also be used for the immobilization of functional bio-macromolecules (bioconjugation).

Polymeric coatings are often polyethylene glycols, poly(ethylene-alt-maleic anhydride) functionalized with dodecylamine, 2-methacryloyloxyethyl phosphorylcholine, polystyrene and polyacrylamide. While bio-polymer coatings includes peptides, proteins, antibodies, carbohydrates and oligonucleotides. Conjugation of inorganic nanoparticles to biomolecules generates hybrid materials that can be used to let the nanoparticles interact specifically with biological systems.

The most common approach to functionalize nanoparticle surfaces with organic ligands consists in the replacement of the original ligands with specifically designed species through a ligand-exchange process. The reagents most used to replace the original ligands are nitrosonium tetrafluoroborate ($NOBF_4$), diazonium tetrafluoroborate compounds (like 4-nitrobenzenediazonium tetrafluoroborate), methyloxonium tetrafluoroborate and triethyloxonium tetrafluoroborate. In these cases, the original ligand is replaced by inorganic ${BF_4}^-$ anions, which provide electrostatic stabilization of the nanocrystals in the polar media. Subsequently, nanoparticle can be readily further functionalized by various capping molecules via a secondary ligand-exchange reaction, since ${BF_4}^-$ anions weakly interact with the surface of nanoparticles. Some uncommon ligand stripping strategies involve acidic solution like HCl solution and formic acid (acid-base ligand-exchange reactions) or the sonication under stirring of a mixture of nanoparticles and new ligand molecules in an anti-dispersion medium (no affinity with original ligand capped-nanoparticles).[101–105]

1.4.2 Inorganic coatings

Inorganic coatings are mainly prepared to protect the core (lower sensitivity to environmental changes), to improve dispersibility in aqueous media and biocompatibility of nanocrystals, and to passivate the surface of the core by suppressing surface electron trap states resulting from unsatisfied bonds on the surface. Therefore, modification of the surface chemistry of nanocrystals can lead to improved PLQYs, changes in catalytic activity, and toxicity. By varying the size, composition, and thickness of the shell, it is possible to finely tune the properties of the nanoparticle. Inorganic coatings can be amorphous or crystalline, which can have the same or different composition of the core.

Dual–phase core–shell nanostructures possess an amorphous shell generally a few nanometers thick. Amorphous boundary layers can effectively reduce interface energy, block the motion of dislocations, trap/absorb and smear accumulated dislocations away along crystal–amorphous interfaces. Silica is an excellent candidate for amorphous coating nanostructures, as it is optically transparent, chemically inert and photo-chemically stable. In addition, SiO_2 is hydrophilic and negatively charged preventing the aggregation form colloidal particles. Silica shell allows core nanoparticle to be biocompatible (reducing its toxicity) and easily bioconjugated with functional groups.

Several strategies have been devised for the fabrication of silica shell/crystalline core nanoparticles often relying on the sol–gel synthesis of silica from an alkoxysilane. The synthetic process involves hydrolysis and poli-condensation of metal alkoxides ($Si(OR)_4$) such as tetraethylorthosilicate (TEOS) or inorganic salts such as sodium silicate (Na_2SiO_3) in the presence of mineral acid (e.g., hydrochloric acid HCl) or base (e.g., ammonia NH_3, ethanolamine $NH_2CH_2CH_2OH$) as catalyst. The structure of the resulting gel is significantly different depending on the catalyst and this is due to the relative rates of the hydrolysis and condensation reactions.

It has been proven that TEOS replaces the capping agent originally present on the hydrophobic nanocrystalts, enabling their transfer into the water phase where silica shell can be prepared. The main limitation of the available synthetic strategies relies on the removal of the templating agent, which generates the porous network. Calcination enables the complete removal of the template and formation of the mesoporous ordered structure, but it may alter the functionalities or compromise the dispersibility of the nanoparticles. And on the other hand, if mild conditions are used the removal of the template is usually incomplete. [106–109] Crystalline inorganic shells, on the other hand, are mainly used to improve the luminescent properties of nanocrystals. The photoluminescence of nanocrystals strongly depends on their surface chemistry, as lattice surface defects, such as dangling bonds, can act as charge carrier traps, resulting in a decrease in PLQY. The inorganic shell serves to passivate the surface trap states and, thus, reduce nonradiative recombination (nonradiative decay of the exciton). The thickness of the shell can also influence the emission properties of nanocrystals. More than one inorganic crystalline shells are often prepared around a single core. The shell often consists of an inorganic material with a band gap wider than that of the core, or the core and shell are made up of the same crystalline matrix (isostructural phases) but contain different doping ions. The inorganic shells are created through an epitaxial growth route, i.e. the pre-formed cores are introduced into the reaction mixture acting as seeds on which the formation of the shell takes place via heterogeneous nucleation.[110–113]

Materials and Methods

2.1 Materials

2.1.1 Reagents, Solvents and Dispersion medium

Oleic acid $C_8H_{17}CH{=}CH(CH_2)_7COOH$

CAS No.112-80-1, MW: 282.47 amu(g/mol), d=0.89 g/cm^3 at 25 °C, laboratory reagent grade 70%, Brand: Fisher Chemical^{TM}.

1-Octadecene $CH_2{=}CH(CH_2)_{15}CH_3$

CAS No.112-88-9, MW: 252.486 amu(g/mol), d=0.789 g/cm^3 at 25 °C, technical grade 90%, Brand: Alfa Aesar.

Ethanol CH_3CH_2OH

CAS No.64-17-5, MW:46.07 amu(g/mol), d=0.789g/cm^3 at 25 °C, reagent grade 95%, Brand: Labkem.

Methanol CH_3OH

CAS No.67-56-1, MW: 32.042 amu(g/mol), d=0.7866 g/cm^3 at 25 °C, analytical reagent grade $\geq$ 99.9%, Brand: Fisher Chemical^{TM}.

Cyclohexane C_6H_{12}

CAS No.110-82-7, MW: 84.16 amu(g/mol), d=0.996 g/cm^3, reagent grade 99.9%, Brand: Labkem.

n-Hexane C_6H_{14}

CAS No.110-54-3, MW: 86.18 amu(g/mol), d=0.6606 g/cm^3, reagent grade 95%, Brand: Labkem.

Indium acetate $In(CH_3CO_2)_3$

CAS No.25114-58-3, MW:291.95 amu(g/mol), d=1.068 g/cm^3 at 25 °C, reagent grade 99.9%, Brand: Thermo Scientific.

Sodium hydroxide NaOH

CAS No.1310-73-2, MW: 39.997 amu(g/mol), d=2.13g/cm^3, pearl, technical grade 95%, Brand: Fisher Chemical™.

Ammonium Fluoride NH_4F

CAS No.12125-01-8, MW:37.037 amu(g/mol), d=1.01 g/cm^3, reagent grade ≥ 98%, Brand: Thermo Scientific.

Neodymium(III) oxide Nd_2O_3

CAS No.1313-97-9, MW: 336.48 amu(g/mol), d= 7.24 g/cm^3, reagent grade 99.9%, Brand: Thermo Scientific.

Acetic acid CH_3COOH

CAS No.64-19-7, MW: 60.052 amu(g/mol), d= 1.05 g/cm^3 at 25 °C, reagent grade ≥ 99.8%, Brand: Thermo Scientific.

Chromium(III) nitrate nonahydrate $Cr(NO_3)_3$

CAS No.7789-02-8, MW: 400.15 amu(g/mol), d= 1.85 g/cm^3 at 25 °C, reagent grade 98.5%, Brand: Alfa Aesar.

Sodium oleate $C_{18}H_{33}NaO_2$

CAS No.143-19-1, MW: 304.44 amu(g/mol), d=0.9 g/cm^3 at 25 °C, reagent grade ≥ 99.8%, Brand: Thermo Scientific.

Acetone CH_3COCH_3

CAS No.67-64-1, MW: 58.08 amu(g/mol), d= 0.78 g/cm^3 at 25 °C, reagent grade ≥ 99.8%, Brand: Thermo Scientific.

Chloroform CH_3CCl_3

CAS No.67-66-3, MW: 119.37 amu(g/mol), d= 1.56 g/cm^3 at 25 °C, reagent grade 98.5%, Brand: Thermo Scientific.

Triethyloxonium tetrafluoroborate EtO_3BF_4

CAS No.99 429-06-1, MW: 217.06 amu(g/mol), d= 1.23 g/cm^3 at 25 °C, reagent grade 99%, Brand: Sigma-Aldrich.

Nitrosonium tetrafluoroborate $NOBF_4$

CAS No.14635-75-7, MW: 116.81 amu(g/mol), d= 2.18 g/cm^3 at 25 °C, reagent grade 99%, Brand: Sigma-Aldrich.

N,N-Dimethylformamide $(CH_3)_2NCHO$

CAS No.68-12-2, MW: 73.09 amu(g/mol), d= 0.94 g/cm^3 at 25 °C, reagent grade 99.8%, Brand: Sigma-Aldrich.

Acetonitrile CH_3CN

CAS No.75-05-8, MW: 41.053 amu(g/mol), d= 0.786 g/cm^3 at 25 °C, reagent grade 99.9%, Brand: Fisher Chemical™.

Deionized water H_2O

CAS No.7732-18-5, MW: 18.02 amu(g/mol), d= 0.998 g/cm^3 at 25 °C, technical grade.

2.1.2 Laboratory Equipment

Na_3InF_6 nanocrystal synthesis setup

- 100% Argon Gas Tank
- Schlenk line with bubbler, cold trap and Dewar flask
- Rotary vane vacuum pump
- Magnetic stir bars
- Heating mantle with temperature controller
- Three-neck 50-mL round-bottom flask
- Liebig condenser
- Cold trap
- Flow control adapter
- Vacuum take off adapter and trap
- Septum for fitting the temperature probe
- Teflon-coated, oval magnetic stir bar (dimensions: 20 × 10 mm)
- Borosilicate glass syringe and needle
- Three micropipettes (ranges: 20–200, 100–1,000 and 1000–10,000 μL) with appropriate disposable tips
- Poly(propylene) manual pipette filler
- Pipettes (capacity: 5 mL and 10 mL)
- Eppendorf tubes (capacity 1.5 mL)
- Poly(propylene) centrifuge tubes (capacity: 15 mL and 50 mL)
- Two graduated cylinders (capacity: 10 mL and 50 mL)

- Sample vials with caps and parafilm
- Pasteur pipettes
- Centrifuge (for falcon and for eppendorf tubes)
- Vortex mixer
- Ultrasonic cleaning bath
- Spatulas with different sizes
- Laboratory balance (220 g–0.01 mg) and weighing papers
- Crystallization dish (dimensions: 100 mm × 50 mm) and water
- Hot plate (Capacity: 350 °C and 2000 rpm)
- X-ray diffractometer (Panalytical X'PERT PRO) and zero diffraction plates for XRD
- Transmission electron microscope (JEM1010, Jeol) with acceleration voltage up to 100 KeV and carbon-coated copper TEM grids. Madrid, Spain.
- Transmission electron microscope (JEM-F200, Jeol). Venice, Italy.
- FS5 spectrofluorometer (Edinburgh Instruments), measures up to 850 nm
- Quartz cuvettes (Hellma)
- 808-nm and 405-nm diode laser (Lumics GmbH)
- Optical fibers
- Ocean HDX and NIR-Quest spectrometers for visible and near-infrared measurements, respectively (Ocean Insight)
- Fourier-transform infrared spectrophotometer IRSpirit (SHIMADZU)
- Mini-Pellet press kit Specac$^{\text{TM}}$ with manual hydraulic presses for KBr tablets
- Dynamic Light Scattering instrument, Zetasizer Advance Pro (Malvern) size range 0.3 nm to 10 μm, minimum volume 12μL

Chromium oleate $\mathrm{Cr(C_{18}H_{33}O_2)_3}$ preparation setup

- Laboratory balance (220 g-0.01 mg) and weighing papers
- Spatula
- 25mL-single-neck round-bottom flask
- Magnetic stir bars
- Allihn condenser
- Flask clamp
- Inlet and outlet tubes for cooling water

- Crystallization dish (dimensions: 100 mm x 50 mm) and water
- Magnetic stirrer hot plate (Capacity: 350 °C and 2000 rpm)
- 25mL-separatory funnel with a suitable cap
- 50mL-becker
- 10mL-pear-shaped evaporating flask
- Rotary evaporator
- Glass vial with cap
- Parafilm
- Pasteur pipettes
- Graduated cylinder (capacity: 10 mL)
- Vortex mixer
- Ultrasonic cleaning bath

Neodymium acetate $Nd(CH_3COO)_3$ preparation setup

- Microwave reaction vial
- Magnetic stir bars
- Microwave synthesis reactor
- Crystallization dish (dimensions: 100 mm x 50 mm) and silicone fluid
- Magnetic stirrer hot plate (Capacity: 350 °C and 2000 rpm)
- Glass vial with cap

Stripping of oleate on Na_3InF_6 nanocrystals

- Parafilm
- Pasteur pipettes
- Graduated cylinder (capacity: 10mL)
- Magnetic stirrer plate (Capacity: 2000 rpm)
- Glass vial with cap
- Sample vials with caps and parafilm
- Pasteur pipettes
- Centrifuge
- Poly(propylene) centrifuge tubes (capacity: 15 mL)
- Laboratory balance (220 g - 0.01 mg) and weighing papers

- Spatula
- Vortex mixer
- Ultrasonic cleaning bath

2.2 Experimental Protocols

2.2.1 Preparation of precursor stock solutions

Solution 1.0 M of sodium hydroxide in methanol

In a 50 mL - falcon tube, pearls of caustic soda (1599.88 mg, 40 mmol) were dissolved with methanol (40 mL) with the aid of an ultrasonic bath at room temperature for about 20 minutes. The falcon tube was sealed and stored in a refrigerator at ∼ 4 °C until needed. The sodium hydroxide-methanol stock solution is stable for 1 month without producing any noticeable precipitation.

Solution 0.4 M of ammonium fluoride in methanol

In a 50 mL - falcon tube, small crystals of ammonium fluoride (711.11 mg, 19.2 mmol) were dissolved with methanol (48 mL) with the aid of an ultrasonic bath at room temperature for about 30 minutes. The falcon tube was sealed and stored in a refrigerator at ∼ 4 °C until needed. The ammonium fluoride-methanol stock solution is stable for 1 month without producing any noticeable precipitation. A solution with greater concentration would be difficult to obtain at room temperature because ammonium fluorides is slightly soluble in alcohol.

Solution 0.2 M of chromium oleate $Cr(C_{18}H_{33}O_2)_3$ in n-hexane

In a one-neck-round bottom flask fitted with an allihn condenser in vertical position, chromium(III) nitrate (238.01 mg, 1 mmol) and sodium oleate (974.21 mg, 3.20 mmol) were mixed with deionized (DI) water (2.0 mL), ethanol (1.53 mL) and hexane (3.53 mL). The round-bottom flask was placed into a hot water bath and heated to 70 °C for 2 hours under stirring (high speed). The content of the flask was then transferred into a separating funnel with the aid of a glass rod. The separation of two phases required several minutes. The lower phase, milky white, contained the polar solvents with sodium nitrate (by-product), and the upper phase, greyish blue colour, consisted of hexane, chromium oleate and unreacted sodium oleate. The lower phase was removed and then the organic phase was washed with DI water (7 mL). The residues of sodium oleate, acting as anionic surfactant, stabilised the mixture in the separatory funnel, to break the formed emulsion a small volume of ethanol was sprayed into the liquid mixture. The washed mixture was poured into a small pear-shaped evaporating flask and the hexane was completely removed via vacuum, resulting in a blue solid. The obtained powder of chromium oleate was then dissolved in hexane (5 mL) with the aid of an ultrasonic bath. The stock solution theoretically had a concentration of 0.2 M. The non-polar solvent was n-hexane

which can be easily removed during the first nanoparticle synthesis step. The solution is stable for up to 12 months when stored in sealed glass vials at about 4°C.
The overall chemical reaction involves in the preparation of chromium oleate is:
$Cr(NO_3)_3 + 3Na(C_8H_{17}CH{=}CH(CH_2)_7COO) \xrightarrow{\Delta} Cr^{3+}(C_8H_{17}CH{=}CH(CH_2)_7COO^-)_3 + 3Na(NO_3)$
A graphical representation of the separatory funnelcontaining the bilayer mixture is shown in Figure 2.1.

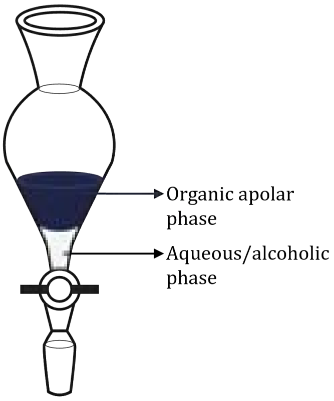

Figure 2.1: Image representing the separatory funnel containing the bilayer mixture, the organic phase is blue and aqueous/alcoholic phase in greyish white.

Solution 0.2 M of neodymium acetate $Nd(CH_3COO)_3$ in water

In a round-bottom reaction vial, neodymium oxide (336.48 mg, 2 mmol) and acetic acid (1.5 mL, 26.2 mmol) were mixed with DI water (1.5 mL, 83.3 mmol). The glass vial was placed in a microwave reactor (rated for 300 PSI at 180 °C). The reaction mixture was kept at these conditions for 30 minutes under stirring (medium speed setting). After the vial had been cooled to room temperature, the magnetic stirrer was removed and the product was transferred into a new vial with a wide aperture to enable a fast dry of it. The container was placed in a crystallization dish containing silicone fluid heated at 60 °C. The heating of the product was kept for more than 24 hours. The dried lilac powder was dissolved in DI water (10 mL) using an ultrasonic cleaning bath. To facilitate the dissolution of neodymium acetate in DI water, acetic acid ($\sim 150\ \mu L$) was added to the solution. The vial with the obtained solution was sealed and stored in a refrigerator at ~4 °C until needed. The neodymium acetate stock solution can be stored in these conditions for 12 months without producing any noticeable precipitation.[1]
The overall chemical reaction occurring during the preparation of neodymium acetate is: $Nd_2O_3 + 6CH_3COOH \xrightarrow{\Delta} 2Nd^{3+}(CH_3COO^-)_3$.
A large excess of acetic acid (~118%) was experimentally used. A graph representing the oscillation of temperature and pressure over time during the preparation of neodymium acetate in the microwave reactor is shown in Figure 2.2.

---

[1] Neodymium acetate may be directly used as solid, like indium acetate, however the use of a solution enables to have a greater control in the added amount of dopants.

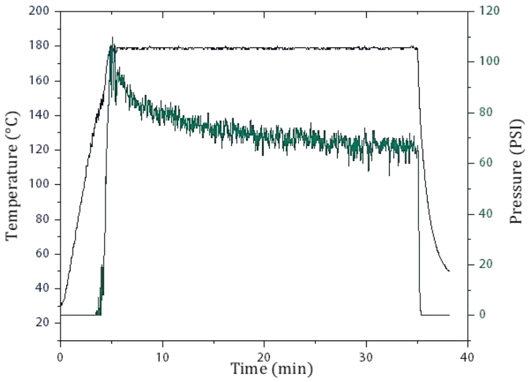

Figure 2.2: Graph representing the oscillation of temperature (left axis) and pressure (rigth axis) over time (heating, reaction and cooling time).

2.2.2 Preparation of sodium indium fluoride nanocrystals

The synthesis of sodium indium fluoride Na_3InF_6 nanocrystals was inspired by the protocol for sodium gadolinium fluoride ($NaGdF_4$) published in 2014.[114] The appropriate variations were done in the amount of precursors because the stoichiometry of the chemical reaction for the synthesis of Na_3InF_6 is different from that for $NaGdF_4$. In addition, the synthetic procedure was optimised for sodium indium fluoride nanocrystals exploring three synthetic parameters related to the growth of the nanocrystals: the rate at which the system was heated until the desired temperature (∼7.5 or ∼15 °C/min), the temperature (270 °C, 280 °C and 290 °C) and the duration of the stage itself (30, 60, 90, 120 minutes). Experimentally performed nanoparticle purification differs almost completely from that proposed in the protocol for sodium gadolinium fluoride.

Preparation of undoped sodium indium fluoride nanocrystals

Preparation of indium oleate The first stage of the preparation of undoped sodium indium fluoride nanocrystals was the preparation of indium oleate. In a 50-mL three-neck round-bottom flask, indium acetate (116.8 mg, 0.4 mmol), oleic acid (4 mL, 8.8 mmol) and 1-octadecene (6 mL, 16.9 mmol) were mixed at room temperature (23–25 °C). Octadecene was chosen as non-polar solvent since its boiling temperature is about 315 °C, higher than the working temperature. The flask was fitted with a thermocouple temperature sensor, a vacuum take-off adapter with trap and a flow control adapter. The vacuum pump and magnetic stirrer were turned on, then the stopcock on the Schlenk line was opened to create the vacuum in the flask. At this point, indium acetate started to dissolve in the organic solvent and the temperature began to decrease. The heating mantle was turned on, the solution was heated at 100 ±8 °C for 10 min under stirring to ensure the complete dissolution of the indium acetate in the organic phase. The reaction mixture was further heated at 150±5 °C for 20 min under stirring. The heating mantle was switched off and removed allowing the slow cooling down to room temperature of the reaction mixture, still under stirring. When the temperature approached the room temperature the stopcock on the Schlenk line was closed, and the vacuum

pump was turned off. The temperature sensor, vacuum take-off adapter and flow control adapter were removed from the flask. Once the yellowish solution was cooled, the preparation of the indium oleate was completed.
The overall theoretical chemical reaction involved in this first step is:
$In(CH_3COO^-)_3 + 3\ (C_{17}H_{33})COOH \xrightarrow{\Delta} In^{3+}((C_{17}H_{33})COO^-)_3 + CH_3COOH$
Actually, an excess of oleic acid (~6 times) was experimentally used.
In Figure 2.3 the chemical structure of indium oleate complex is shown.

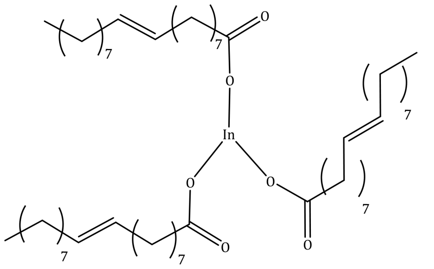

Figure 2.3: Indium (III) oleate complex. Oleate is a monodentate ligand.

Nucleation The 1 M sodium hydroxide solution (2 mL, 2.0 mmol) and the 0.4 M ammonium fluoride solution (6.6 mL, 2.6 mmol) were pipetted into 50-mL round-bottom flask containing the reaction mixture obtained in the previous synthetic stage. The way of introduction of precursors (sodium and fluoride ions) was explored, but additional tests would be necessary to make consistent suppositions. In most of experiments the precursors were individually introduced in the flask, giving priority to the sodium hydroxide solution. In some experiments the precursors were introduced together in the flask, sodium hydroxide and ammonium fluoride solutions were pipetted into a 15-mL falcon tube, the mixture was sonicated using an ultrasonic cleaning for 10 seconds and pipetted in the flask using a pasteur pipette. Immediately after the introduction of precursors the round-bottom flask was placed in a hot water bath and heated at 50 °C for 30 minutes under stirring. This stage consisted in the formation of sodium indium fluoride nuclei from which nanocrystals were then originated. The flask was removed from the water bath and it was cooled down by about twenty degrees under stirring.

Nanocrystals growth The round-bottom flask was placed inside the heating mantle and fitted with a thermocouple temperature sensor, a vacuum take-off adapter with trap and a flow control adapter. The vacuum pump and magnetic stirrer were turned on, then the stopcock on the Schlenk line was opened to create the vacuum in the flask. The heating mantle was switched on and set at 100 °C. The reaction mixture was kept at 100±8 °C for 10 minutes to remove the excess of methanol (derived from solutions of precursors). At this point, the stopcock of the vacuum in the Schlenk line was slowly closed and that of the argon flow was gradually opened. The stopcock in the flow control adapter (mounted on the flask) was opened to fill the flask with argon. The reaction mixture was heated to 290±5 °C with a heating rate of ±7.5 °C/min for 30 minutes under stirring.[2] This stage consisted in the growth of sodium indium fluoride nanocrystals. The heating mantle was switched off and removed to cool down slowly until room temperature under stirring the reaction mixture. When the temperature was about 60 °C the stopcock in the flow control adapter and then on the Schlenk line were closed.

Purification The content of the flask (∼10 mL) was transferred into a 50-mL centrifuge tube. Ethanol (20.0 mL) was added to the reaction mixture and the falcon tube was centrifuged for 5 minutes at 3'800 g at room temperature. The supernatant was discarded and the remaining pellet was dispersed in cyclohexane (4 mL). To restore the ligand coverage on the surface of the nanoparticles, oleic acid (350 μL) was pipetted into the dispersion, the centrifuge tube was agitated using a vortex mixer and sonicated with the aid of an ultrasonic bath at room temperature for 3 minutes. The final dispersion was spun down at 500 g for 1 min at room temperature, the supernatant was collected and transferred in two 15-mL centrifuge tubes (to obtain a better centrifugation). Ethanol (4.3 mL) was added to each centrifuge tube. The mixture was agitated with a vortex mixer, and then spun down at 6'575 g for 5 min at room temperature. Two supernatants were discarded and each pellet was dispersed in cyclohexane (2 mL). The dispersions were agitated with a vortex mixer and sonicated for three minutes. Ethanol (2 mL) and methanol (2 mL) were added to the dispersion in each falcon tube. The mixture (apolar organic phase and alcoholic phase) was stirred with a vortex mixer and then spun down at 6'575 g for 5 min at room temperature. Two supernatants were discarded, the washed Na_3InF_6 nanocrystals (pellets) were dispersed in cyclohexane (1 mL). The dispersions were agitated with a vortex mixer, sonicated for three minutes and then joined together. The final dispersion of Na_3InF_6 nanocrystals in cyclohexane was transferred to a glass vial. Oleic acid (150 μL) was pipetted into the vial to restore the outer organic shell and after 3 minutes of sonication the vial was sealed with parafilm and stored in a refrigerator at ∼ 4 °C.
The overall chemical reaction involved in the synthesis is:
$In^{3+}(C_{18}H_{33}O_2)_3 + 3Na^+OH^- + 6\,NH_4{}^+F^- \xrightarrow{\Delta}$ oleate capped–Na_3InF_6NCs$+x\,NaF\downarrow + 6NH_3\uparrow + 3H_2O\uparrow$
Actually, there was an excess of sodium cations (+66.7 %) and fluoride ions (+10%) in the experimental reactions. The experimental molar ratio among the various precursors was: $Na^+:In^{3+}:F^- = 25:5:33$. Sodium fluoride was one of the main by-product of the reaction, and it was separated from sodium indium fluoride nanocrystals during the first and second wash steps. The concentration of nanoparticles in the final dispersion has not been determined, assuming a reaction yield of 100% the concentration is 59.56 mg/mL (200 mM).

---

[2] The ideal growth conditions for sodium indium fluoride nanocrystals were searched, hence some variations of this stage were performed. Firstly, two heating rates were explored (±7.5 °C/min and ±15 °C/min). Secondly, three temperatures (270 °C, 280 °C and 290°C). Several experiments were done for each heating rate and temperature. To search the ideal period of time of growth, once the selected temperature was reached every 30 minutes up to 120 minutes an aliquot of sample (1 mL) was collected using a glass syringe fitted with a long needle.

A schematic representation of four main stages involved in the preparation of sodium indium fluoride nanocrystals is shown in Figure 2.4.

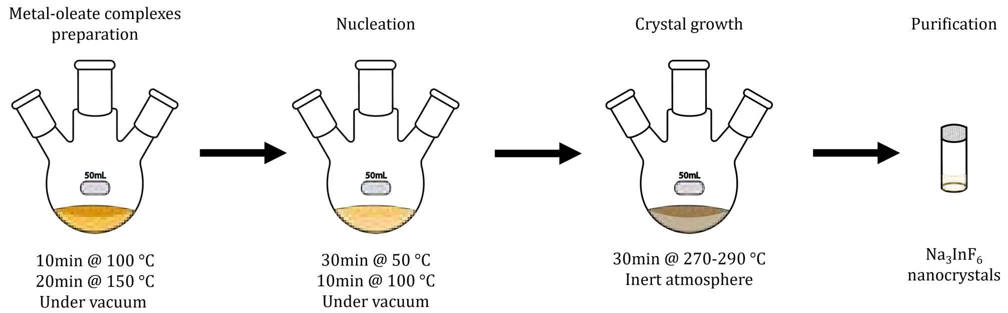

Figure 2.4: Schematic representation of four main stages involved in the synthesis of sodium indium fluoride nanocrystals: preparation of metal-oleate complexes (based on indium(III) or neodymium(III)), nucleation, growth and purification of nanocrystals.

A schematic representation of the stages involved in the precipitation and purification of sodium indium fluoride nanocrystals is shown in Figure 2.5.

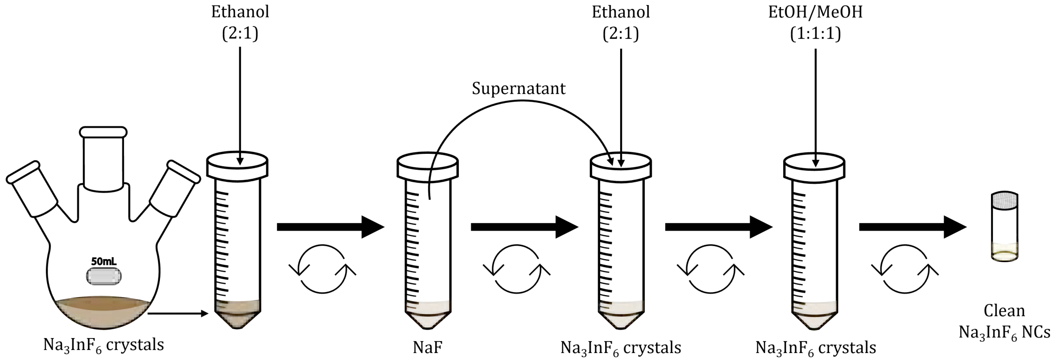

Figure 2.5: Schematic representation of nanocrystals purification. Circular arrows in the chart symbolize vortex mixer and sonicator.

2.2.3 Preparation of doped and co-doped sodium indium fluoride nanocrystals

The preparation of doped or co-doped sodium indium fluoride nanocrystals differs from the previous synthetic procedure only for the quantities of precursors involved in the first stage, described in paragraph 2.2.2. All the other synthetic steps illustrated in subsection2.2.2 are valid even for the preparation of doped and co-doped nanoparticles.

Preparation of metal(III) oleate

Doping with 2% Cr(III) [3] In a 50-mL three-neck round-bottom flask, indium acetate (114.44 mg, 0.392 mmol), the solution of chromium oleate (40μL, 0.008 mmol), oleic acid (4 mL, 8.8 mmol) and 1-octadecene (6 mL, 16.9 mmol) were mixed at room temperature (23–25 °C).

Doping with 5% Cr(III) [3] In a 50-mL three-neck round-bottom flask, indium acetate (110.94 mg, 0.380 mmol), the solution of chromium oleate (100μL, 0.02 mmol), oleic acid (4 mL, 8.8 mmol) and 1-octadecene (6 mL, 16.9 mmol) were mixed at room temperature (23–25 °C).

Doping with 2% Nd(III) [3] In a 50-mL three-neck round-bottom flask, indium acetate (114.44 mg, 0.392 mmol), the aqueous solution of neodymium acetate (40μL, 0.008 mmol), oleic acid (4 mL, 8.8 mmol) and 1-octadecene (6 mL, 16.9 mmol) were mixed at room temperature (23–25 °C).

Doping with 5% Nd(III) [3] In a 50-mL three-neck round-bottom flask, indium acetate (110.94 mg, 0.380 mmol), the aqueous solution of neodymium acetate (100μL, 0.02 mmol), oleic acid (4 mL, 8.8 mmol) and 1-octadecene (6 mL, 16.9 mmol) were mixed at room temperature (23–25 °C).

Co-doping with 5% Cr(III) and 2% Nd(III) [3] In a 50-mL three-neck round-bottom flask, indium acetate (108.61 mg, 0.372 mmol), the aqueous solution of neodymium acetate (40μL, 0.008 mmol), the solution of chromium oleate (100μL, 0.02 mmol), oleic acid (4 mL, 8.8 mmol) and 1-octadecene (6 mL, 16.9 mmol) were mixed at room temperature (23–25 °C).

After each of these five steps, the synthetic phases already illustrated in the previous section 2.2.2 were carried out.

2.2.4 Stripping of oleic acid from nanocrystal surfaces by using Meerwein's salt

The procedure for the removal of oleate molecules on the surface of sodium indium fluoride Na_3InF_6 nanocrystals was inspired by the protocol reported in a research article published in 2012 in Angewandte Chemie.[115]
Firstly, the preparation of precursor stock solutions was performed. A solution of triethyloxonium tetrafluoroborate (100 mM, 18.999 mg/mL) was made dissolving the Meerwein's salt (200 mmol, 38.00 mg) in in acetonitrile (2 mL, ACN). A solution of trisodium citrate (400 mM, 103.22 mg/mL) was prepared dissolving the salt (309.66 mg) in DI water (3 mL).[4]

---

[3] The percentages of dopant ions are expressed in terms of concentration and not in terms of ions.

[4] The removal of oleic acid from the surface of nanocrystals was also performed using nitrosonium tetrafluoroborate $NOBF_4$ and formic acid HCOOH.

The purified dispersion of nanocrystals in cyclohexane (650 μL) was mixed with oleic acid (100 μL) and then sonicated for 3 minutes to break potential aggregations. The sample was centrifuged for two minutes at 500 g to remove sodium fluoride (by-product) from the dispersion. The supernatant was collected and transferred in a 15-mL centrifuge falcon tube. The sample was divided into four aliquots (150 in each epperndorf tube) and mixed with ethanol (900 μL in each epperndorf tube). Four samples were spun down at 4'000 g for 5 min at room temperature in a centrifuge. The supernatant was discarded, the pellet in each epperdorf tube was dispersed in cyclohexane (700 μL) agitating it with a vortex mixer and sonicating it for 3 minutes. The triethyloxonium tetrafluoroborate solution in ACN (175 μL) was added to each eppendorf tube containing the dispersion of nanocrystals.[5] All four samples were agitated with a vortex for 30 seconds. Four samples were then sonicated for a variable time (0, 3, 6, 9 minutes) to determine the ideal reaction time for the removal of oleic acid on the surface of nanoparticle. Immediately after each incubation time in the ultrasonic bath at room temperature, chloroform (350 μL for each eppendorf tube) was then added to the mixture in order to dissolve the free oleic acid (removed from the surface of NCs) and to trigger the precipitation of BF_4^-ion-coated-NPs. The mixture was spun down at 3'000 g for 5 min at room temperature. The supernatant was discarded, the pellet theoretically containing BF_4^-ion-coated-NPs was mixed with dimethylformamide (260 μL for each sample) and slightly heated. The aqueous solution of trisodium citrate (262 μL) was added in each eppendorf tube containing the nanocrystals, the obtain mixture was agitated with a vortex mixer for 1 minute and sonicated for 10 minutes. The purification of citrate capped-NCs was performed by adding acetone (520 μL). The sample was spun down at 3'000 g for 10 minutes. The supernatant was discarded and disperse in DI water (1 mL).

A schematic representation of the stages involved in the ligand exchange on the surface of sodium indium fluoride nanocrystals from oleate (apolar ligand) to citrate (polar ligand) is shown in Figure 2.6.

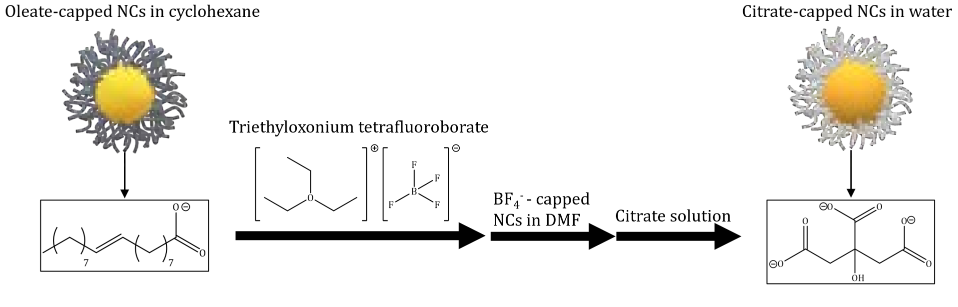

Figure 2.6: Schematic representation of nanocrystal ligand exchange.

---

[5] To explore the ideal amount of Meerwein's salt required to remove oleic acid from the surface of sodium indium fluoride NCs, the experimental procedure was repeated adding a different amount of salt to each samples. instead of using a theoretical molar ratio between NCs and triethyloxonium tetrafluoroborate of 1:2.5, where used a molar ratio of 1:1.25. Therefore, the Meerwein's salt stock solution was diluted, 200 μL of acetonitrile were added to 200 μL of solution in an eppendorf tube. The diluted solution (175 μL) was pipetted into each of four containers.

2.3 Characterization of Colloidal Suspensions

2.3.1 Transmission Electron Microscopy

Transmission Electron Microscopy (TEM) is an advanced microscopy technique to obtain information about the composition, crystal structure, and morphology of nanomaterials. A conventional transmission electron microscope is composed of an electron-optical system containing an electron gun (which produces the beam of electrons) and several magnetic lenses stacked vertically to form a lens column. The electrons produced by the electron gun are accelerated and focused into a small, uniform, beam by the condenser lenses. When the electron beam strikes to the specimen, the interaction can produce numerous outcomes: some electrons are bounce back out of the sample (back-scattered electrons), some cause the ejection of electrons by the surface of the sample (secondary electrons), some are scattered (transmitted electrons are those that are scattered forward), some are absorbed. The instrument can provide at the same time either the diffracted pattern or the image of the specimen. This is possible because the specimen is located between the pre-field and the post-field ot the objective lens The objective lens takes electrons scattered by the specimen and forms a diffraction pattern in the back focal plane and an image of the specimen in its image plane. The instrument can have two different operating modes: imaging and diffraction mode, see Figure 2.7. When TEM is operating in diffraction mode information on the crystalline structure either of a small region in the specimen or a single nano-structure can be obtained, unlike X-ray diffraction which provides an information which is the average of crystallites within a sample. In addition, electron diffraction patterns are direct representations of 2-D sections through the reciprocal lattice of the specimen. When TEM is operating in imaging mode, an aperture located in the back focal plane is used in order to increase the contrast in the magnified image. Depending on the orientation of the beam respect to the optical axis and to the position of the aperture on the back focal plane, three different imaging modes can be obtained: bright field mode, dirty dark field mode and axial dark field mode. In the bright field mode, the beam of electrons is parallel to the optical axis and the aperture is centred to the optical axis (only transmitted beam); in the dirty dark field mode the beam of electrons is still parallel to the optical axis, but the aperture is off-centered selecting a diffracted beam of electrons; and finally in the axial dark field mode the aperture is centred to the optical axis, but the electron beam is tilted by a specific angle respect to the optical axis. TEM can also produce a high resolution image when a large aperture (or no aperture at all) is used to enable interference among the diffracted beams of electrons. HR-TEM provides direct images of the crystallographic structure of nanomaterials at the atomic level.

It should be stressed that carrying out TEM analyzes on a sample might damage it. The damage caused by an electron beam is usually not negligible for materials with poor thermal conductivity, as some damage can occur due to the rise in temperature following the electron-matter interaction. The crystalline structure may change due to heating, cracks and holes may appear on the surface or inside a specimen. Usually metals and semimetals are able to endure electron beams with high energy, while insulators and ceramics may suffer the problem of heating.[116–118]

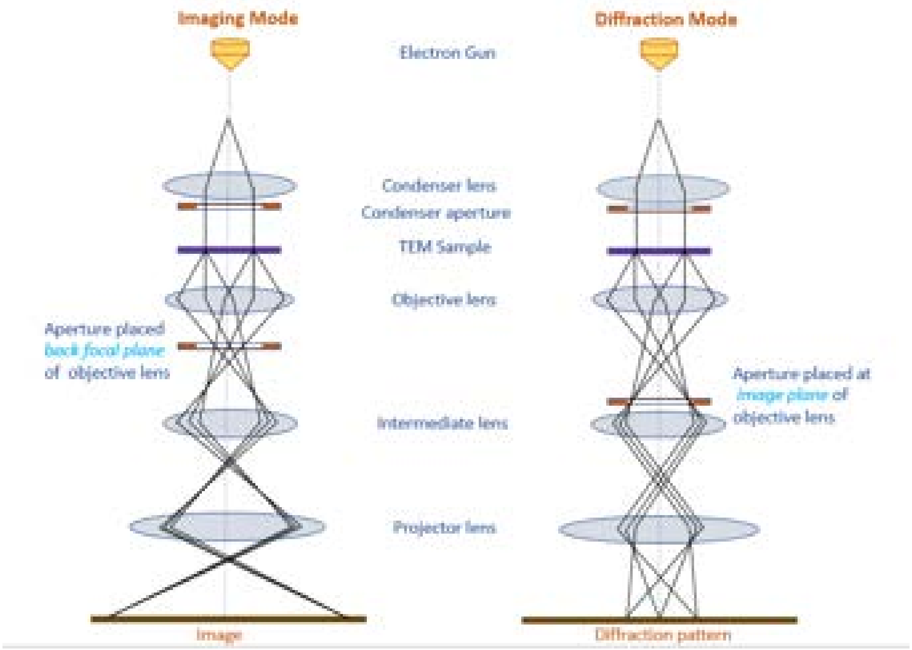

Figure 2.7: Schematic representation of a TEM operating in imaging (left) and diffraction (right) mode. Figure from [119]

2.3.2 X-ray Diffraction

X-ray diffraction (XRD) is a non-destructive analytical technique primarily used for phase identification of a crystalline material, but it can provide useful information on unit cell parameters, atomic positions, crystallite sizes and lattice strain. X-rays are highly energetic EM radiations, see Figure 1.5, characterized by wavelengths of the order of atomic distances. A X-ray diffractometer consists of three basic elements: an X-ray tube, a sample holder, and an X-ray detector. Two fundamental components of the X-rays tube are: cathode and anode with copper bar (the metal target is commonly copper, but it can be also iron, cobalt, molybdenum,. . .). A filament (usually tungsten-based) is heated to produce electrons, which are then accelerated toward the metal target by applying a voltage. The interaction of accelerated electrons with metal causes the generation of X-rays. Such EM radiations wavelength between 0.2 and 0.1 nm, being highly energetic are termed as hard X-rays. X-rays wavelengths frequently used on lab-scale diffractometers are those generated by using a copper tube, producing K-α1, K-α2 wavelengths respectively equal to 1.540562 and 1.544398 . When impinging on a crystalline sample, x-rays are coherently and elastically scattered (diffracted) into very specific directions (given by the Bragg's law) with various intensities. When an electron interacts with an X-ray photon, it becomes a source of secondary spherical waves, meaning that an arrangement of electrons generates an array of spherical waves. These waves interfere along many directions through a destructive interference, but in few specific directions their interference is constructive. When waves move in phase with each other they generate a diffraction pattern.[120, 121] The detector records diffracted intensities vs angle

2θ, the angle θ corresponds to the detector position with respect to the sample. The lattice spacing d$_{hkl}$ for each set of crystalline lattice planes is determined through the well-known Bragg's law.

$$2\ d_{hkl}\ sin\theta\ =\ n\lambda \tag{2.1}$$

where (hkl) are the Miller indices, λ is the X-ray wavelength, and n is the integer representing the order of the diffraction peak. X-ray diffraction is a powerful technique also to study the crystal size and lattice strain. Crystallite size affects the FWHM (Full Width at Half Maximum) of diffraction peaks in according to the Scherrer equation

$$D(2\theta)\ =\ \frac{K\ \lambda}{L\ cos\theta} \tag{2.2}$$

where D is the width of the peak located at 2θ in the diffraction pattern, K the shape factor (constant close to 1) and L the crystallite size. Lattice strains can cause a shift in position and the broadening of diffraction peaks. A compressing stress for example would make the d_{hkl} spacing smaller, and usually the broadening in XRD peaks due to strain is visible at high angles..[117, 122–124]

2.3.3 Dynamic light scattering

Dynamic light scattering (DLS) spectroscopy is a simple and non-contact technique that relies on the intensity of light scattered from a sample or solution to detect the particle size distributions from the nanometer to the submicron range. A monochromatic light beam impinges on a sample and part of it is scattered towards a detector which collect the variation in the intensity of the scattered light as a function of time. Lasers typically used in DLS instruments span from red light to NIR, the most common wavelengths are 532, 637 and 732 nm. The hydrodynamic sizes of the particles in the colloidal solution are then estimated by determining the constant and random motions of the particles in the dispersion medium. This technique, besides the determination of particle sizes in colloidal samples, is particularly useful for studying the stability of formulations and for detecting the presence of aggregation or agglomeration. Particles when suspended in a fluid move freely in space continuously and randomly, this motion is called Brownian motion. The hydrodynamic diameter of a particle affects the speed with which it can move, small particles diffuse faster than larger ones. The instrument, after having determined the intensity of the light scattered as time passes, generates a mathematical correlation function between the diffusion capacity of the light (as a function of time) and the size of the particle itself. The size of a particle (hydrodynamic diameter $2R_H$) is calculated from the diffusion coefficient D by using the Stokes-Einstein equation:

$$2R_H\ =\ \frac{K_B\ T}{3\ \pi\ \eta\ D} \tag{2.3}$$

where K_B, T and η are the Boltzmann constant,temperature and viscosity of the liquid respectively. It should be stressed that this law relies on spherical particle with radius R_H. Real particles may deviate from the Stokes-Einstein model by being solvated, asymmetrical or both. The friction factor deviates from the ideal one

($f = 6\pi\ \eta\ R_H$) in these situations causing DLS results inconsistent with the actual sizes of particles, friction factor and diffusion coefficient are inversely proportional at constant temperature.
If the particles are small compared to the wavelength of the laser used, $2R_H\ <\sim 0.1\lambda$, the scattering arising from the particles illuminated by a vertically polarized laser will be essentially isotropic, i.e. equal in all directions. The scattering of light in this regime is called Rayleigh scattering, and the intensity of the scattered light (I_S) depends both on the wavelength of the laser and on the size of the particles: $I_S \propto \lambda^4\ (2R_H)^6$. Due to this significant dependence of signal intensity on size detecting the contribution of scattered light from small particles in a heterogeneous mixture containing both very small and very large particles is extremely complex. Therefore this technique turns out to be particularly effective especially for detecting the hydrodynamic diameters of colloids containing mono-disperse particles of spherical shape.[125]

2.3.4 Fourier-transform infrared spectroscopy

Fourier-transform infrared spectroscopy (FTIR) is a rapid and non-destructive spectroscopic technique that allows obtaining an absorption spectrum of a sample in the gaseous, liquid and solid state. This vibrational spectroscopy provides details about the chemical bonds and functional groups in an organic compound, making it particularly useful for confirming the identity of pure compounds. Infrared radiations are EM radiations, see Figure 1.5, the IR area of the spectrum is further divided according to the wave number into three zones: NIR (12'500 –4'000 cm^{-1}) , MIR (4'000 –200 cm^{-1}) and FIR (200 –10 cm^{-1}). FTIR spectroscopy employs MIR-radiation as it is resonant with the energy differences between the ground state and higher vibrational energy levels. A molecule is defined as active IR if an electric dipole variation occurs due to the molecular vibration induced by the absorption of radiation. The vibration motion is complex and involves the displacements of all the atoms, however it is possible to break it down into various harmonic motions independent of each other, called normal modes. In the case of a polyatomic molecule made up of N atoms it can be broken down into 3N-6. The superposition of the various normal modes will constitute the real vibrational motion of the molecule itself. Molecular vibrations can either involve a change in bond length (stretching) or bond angle (bending). Stretching can be symmetrical or antisymmetrical, whether bonds elongate/contract together or not. While bending vibrations are often subdivided into scissoring, rocking, wagging, and twisting. The harmonic oscillator approximation according to which molecular vibrations can be approximated to a spring is a good first approximation of vibrational motions especially for molecules made up of strong chemical bonds. The position of the signal depends on both the atomic mass and the bond strength. As the atomic mass decreases and the strength of the bond between the atoms increases, the wave number will also be greater. The vibrational transitions can be: fundamental, overtone, hot (between two excited vibrational states) and combination (combination of two normal vibrational modes starting from the ground state). Fundamental transitions are the most probable and consequently the most intense ($1 \leftarrow 0$). The anharmonicity of the real system, however, allows further transitions between vibrational levels. The first overtone bands derive from transitions from the ground state to the second second excited state (2←0) and have an intensity slightly lower than half of the fundamental band. The second overtone bands arise from transitions (3←1) from one excited state to another. FTIR is therefore an extremely useful technique for the analysis of individual compounds as it allows to distinguish the different functional groups located in a molecule. The advantages of using a Fourier transform spectrophotometer are various, including sensitivity, rapid acquisition which consequently also allows the determination of multiple spectra improving the signal-to-noise ratio, and smaller spectral resolution.[126, 127]

2.3.5 PL spectroscopy and PLE spectroscopy

Experimentally, photoluminescence can be measured through different spectroscopic techniques, all of which are part of photoluminescent spectroscopy. PL basically uses a laser beam to capture light generated from a material when irradiated by a laser beam. the commercial equipment is called spectrofluorimeter. Depending on the mode of excitation and detection over time, luminescence measurements can be classified as steady-state and time-resolved. Steady-state measurements implement constant illumination and observation, so it is the study of long-term average emission of a material after its irradiation. Whereas time-resolved measurements are performed with pulsed excitation and the emission is monitored as a function of time, they require a complex instrumentation. This thesis work referes only to steady-state measurements.[2, 34, 128]
During an experiment, the sample is excited with a laser beam or with a lamp followed by a monochromator. The emitted light is collected by a focusing lens and analyzed by means of a second monochromator, followed by a suitable detector connected to a computer. In Figure 2.8 is shown a schematic diagram of a photoluminescence experimental setup.

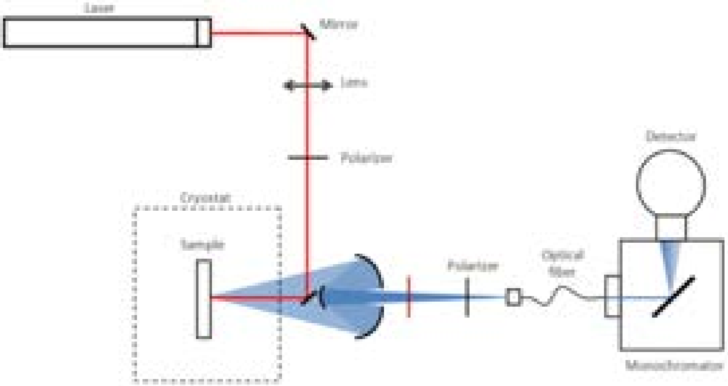

Figure 2.8: A schematic diagram showing the main elements for measuring photoluminescence spectra. The excitation source is a laser beam in this sketch. The emitted light is collected by a mirror system and focused on the entrance hall of an optical fiber.[129]

Two kinds of spectra, excitation and emission, can be registered:

- In excitation spectra, the emission monochromator is fixed at any emission wavelength while the excitation wavelength is scanned in a certain spectral range. It is measured the variation of emission intensity at a fixed energy (wavelength) while changing excitation energy in the desired spectral region. The peaks in the PLE spectra provide a range of wavelengths over which the sample absorbs and emits at the chosen emission wavelength, and thereby essentially supplying a map of the electronic energy structure of the material.
- In emission spectra, the excitation wavelength is fixed and the intensity of the emitted light is measured at different wavelengths by scanning the emission monochromator. The λ_{exc} is established by the PLE spectrum of the material. The wavelength associated with the highest intensity excitation peak in PLE spectrum is the one that will be set as excitation radiation for the sample. The incident radiation influences the intensity of emission peaks, but not the wavelength of the emitted light that is characteristic of the nanophosphor.

Results and Discussion

The research project developed during this thesis was mainly focused on the working out a procedure for the synthesis of undoped Na_3InF_6 nanocrystal (NCs). More than thirty reactions were repeated in order to determine the best conditions for the synthesis of this nanomaterial.

The first group of reactions made it possible to implement changes in the nanoparticle purification process. The samples obtained by the first laboratory experiments showed a heterogeneous population in shape, size and beam sensitivity to electrons in TEM measurements. The samples contained both very small structures (less than 100 nm) and very elongated structures of the order of a few micrometers. When the beam of electrons was focused on a specific area of the TEM grid the sample started to damage showing contamination due to the organic ligands (oleate), as shown in Figure 3.1.

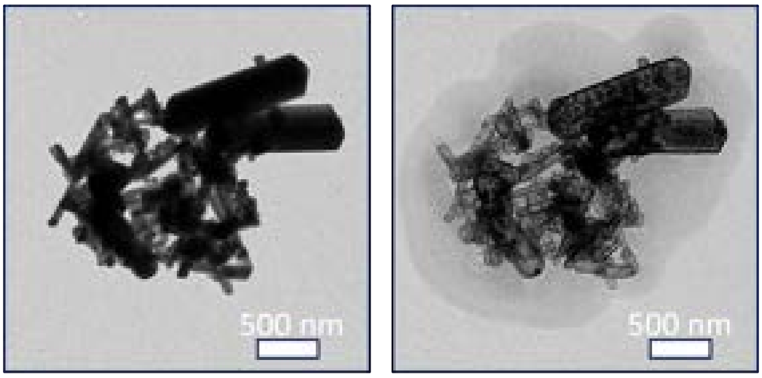

Figure 3.1: TEM images obtained at an accelerating voltage of 100 kV before (rigth) and after (left) focusing the electron beam on the specific area of the TEM grid.

X-ray diffraction patterns of these first samples evidenced the presence of sodium fluoride, a by-product of the synthetic reaction.
The heterogeneity of the sample and the greater intensity of the signal of NaF in XRD pattern suggested some issues related to the purification of the nanoparticles themselves.

The NCs obtained had a high affinity towards apolar solvents since their surface is decorated with hydrophobic organic ligands (oleate). Oleate is a carboxylate made

up of a long carbon chain and therefore has some strong affinity towards apolar organic solvents. Furthermore, the external surface of each nanocrystal has a positive charge due to an excess of indium ions having unsaturated valency. The molecules of oleate, being a negative monodentate ligand, are therefore attracted to the surface of the NCs making a sort of organic shell that surrounds the inner inorganic core.
The experimental procedure carried out in this thesis project was inspired by a protocol for the synthesis of sodium gadolinium fluoride particles. In this protocol, the precipitation of $NaGdF_4$ NPs is performed using a volume ratio 1:1 between the medium in which the NPs are dispersed and the antisolvent. It is reasonable to hypothesize that the affinity of Na_3InF_6 NPS towards the reaction liquid (mixture of 1-octadecene and oleic acid) is greater than the one exhibited by $NaGdF_4$ NPs. Therefore, Na_3InF_6 NCs resided in the supernatant after centrifugation. For these reasons, the first purification step of the nanoparticles consisted in the precipitation of the nanoparticles using a volumetric ratio 1:2 between the final product of the reaction and ethanol. In order to remove the by-product of the reaction (NaF), a further purification step was added: NCs dispersed in cyclohexane were centrifuged for 2 minutes using a low centrifugal force (500 g) to cause the precipitation of the salt, NaF, which should be poorly soluble in a mixture of cyclohexane and oleic acid. Despite this additional purification step, two fingerprint reflections of sodium fluoride were still observed in some XRD patterns of different final samples. The critical issue of this further purification step is probably related to the transfer of the supernatant (containing the Na_3InF_6 NCs) using a Pasteur pipette into a new container. It can be presumed that a small part of NaF is still collected. However, it was possible to overcome this issue by combining the extra purification step with the increasing of the amount of antisolvent (ethanol). In this way, it was possible to obtain the first TEM images of the sought nanoparticles. Figure 3.2 reports two TEM images showing the substantial differences between the samples obtained with or without these variations in the purification procedure.

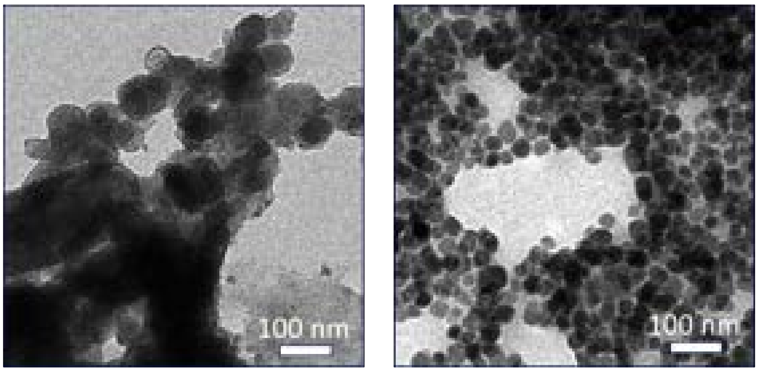

Figure 3.2: TEM images before (rigth, obtained at an accelerating voltage of 100 kV) and after (left, obtained at an accelerating voltage of 100 kV) optimisation of the protocol for the purification of Na_3InF_6 NCs.

Once the purification steps of the nanoparticles were modified, it was possible to focus on optimisation of the growth conditions of the nanoparticles. Various parameters can determine variations in size, shape and crystalline phase of the nanoparticles, such as temperature, quantity of reagents, types of organic ligand, heating rate and reaction time. Three main parameters were explored:

i) Heating rate at which the reaction mixture reached the desired temperature. The heating mantle had a two-level power regulator: 50% and 100%. When it was set to the lowest level the heating rate was approximately 7 °C/min, while approximately 15 °C/min when set to maximum power.

ii) Temperature involved in the growth of nanoparticles. The effects of reaction temperature in the formation and growth of nanoparticles are often explored during optimisation of synthetic procedure as it usually plays a determining role. Three temperatures has been analysed: 270 °C, 280 °C and 290 °C.

iii) Time duration of nanoparticle growth. The reaction time, as the temperature, is often explored during optimisation of synthetic procedure. Four time ranges has been analysed: 30, 60, 90 and 120 minutes.

The heating rate was the first parameter studied. This parameter was determined manually for five different reactions. When the power was set to the minimum level the heating rate varied from 6.6 °C/min to 7.8 °C/min with an arithmetic mean of 6.9 °C/min; in the other case the heating rate varied from 14.0 °C/min to 15.2 °C/min with an arithmetic mean of 14.7 °C/min. Figure 3.3 shows TEM images of two different samples obtained with the same reaction conditions except for the heating rate.

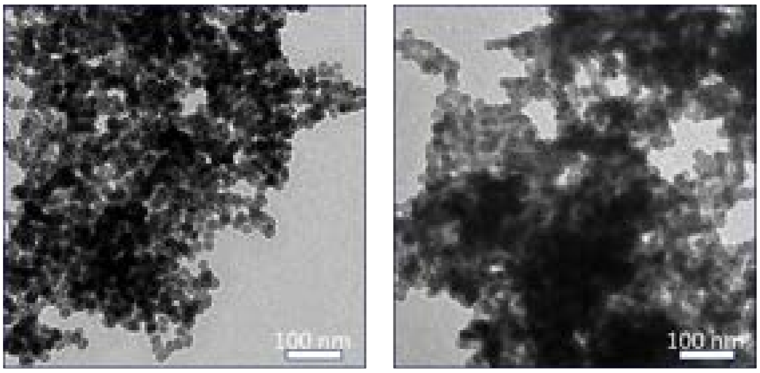

Figure 3.3: TEM images of samples obtained with low (right, accelerating voltage 60kV) and high (left, accelerating voltage 80kV) heating rate. Both samples were obtained with 30 minute growing time rate at 270°C.

There are no significant differences in terms of size of the nanoparticles however it can be noted that the nanostructures appeared more homogeneous using a lower heating rate. The edges of nanoparticles appeared more clearly defined heating at $\sim$ 7 °C/min probably due to an enhanced control in the growth of the nuclei obtained during the nucleation phase. In addition, the nanomaterials obtained with a lower heating rate seemed slightly less sensitive to the electron beam. It should be stressed that from this point onwards all reported TEM images were obtained with an accelerating voltage of 60-80 kV instead of 100 kV as for the previous images in

Figures 3.1 and 3.2. The diffraction patterns of the samples obtained at 270°C and 280°C with two different heating rates, seemed to indicate that using the heating mantle at maximum power resulted in a lower contribution of the amorphous phase, see Figure 3.4.

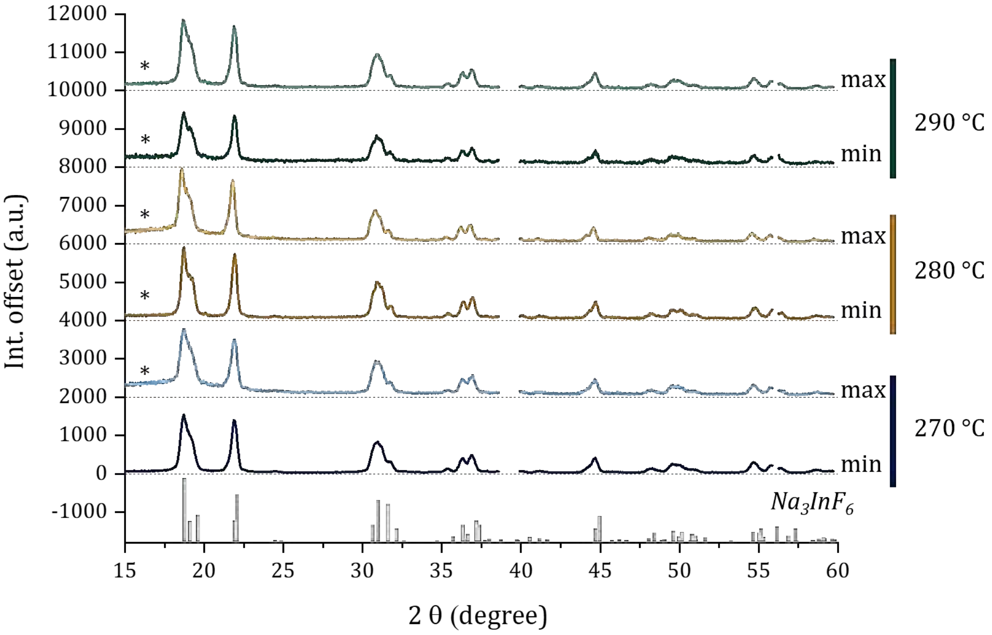

Figure 3.4: XRD patterns of samples obtained at 270 °C, 280 °C and 290 °C after 30 minutes using the same heating mantle set on two distinct power levels. Asterisks mark the broad signal typical for amorphous materials.

Based on these results, it was decided to carry out all the following experiments with the lowest heating rate, partly because the device when set at minimum power allowed less fluctuations of temperature during the chemical reaction. A greater control of the synthesis temperature results also in a greater reproducibility of the synthesis itself.

In order to find the best synthesis temperature, different experiments were performed keeping all the reaction conditions constant except the temperature itself. During each experiment, four aliquots of sample were collected at regular intervals of 30 minutes, up to 120 minutes, to determine also the ideal growth time. Therefore, three different temperatures were studied: 270°C, 280°C and 290°C. For each of them, four different samples were associated depending on the growth time: after 30, 60, 90 and 120 minutes. The volume of the first three aliquots was 1 mL each, while the final aliquot after two hours of reaction was all the remaining reagent mixture, i.e. approximately 7 mL. For each sample, TEM was performed in order to note changes in morphology or size, and XRD to determine the crystalline phases obtained. For each sample, the nanoparticle sizes were determined from the analysis of the TEM images. Using the ImageJ software, the values of the major axis (length) and minor axis (width) were determined. For each sample, about 300 width and length values were obtained. From these data, the distribution of dimensions for each sample was therefore determined.[130]

In Figure 3.5 TEM images of samples obtained at 270 °C after different growth time are shown.

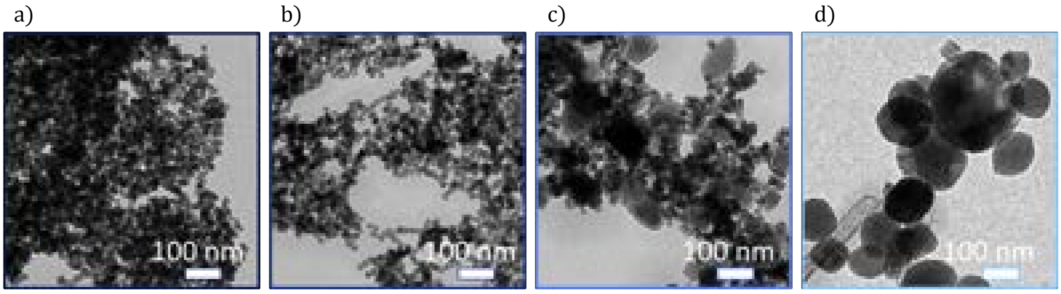

Figure 3.5: TEM images of samples obtained at 270 °C after a) 30 min, b) 60 min, c) 90 min and d) 120 min. Accelerating voltage of 60kV.

In Figure 3.6 and 3.7 size distributions of samples obtained at 270 °C after different growth time are shown.

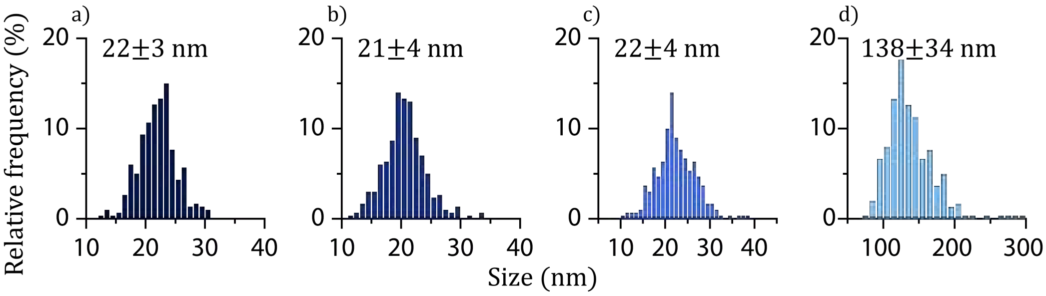

Figure 3.6: Distributions of nanostructures lengths obtained at 270 °C after a) 30 min, b) 60 min, c) 90 min and d) 120 min. Data determined by analysing TEM images.

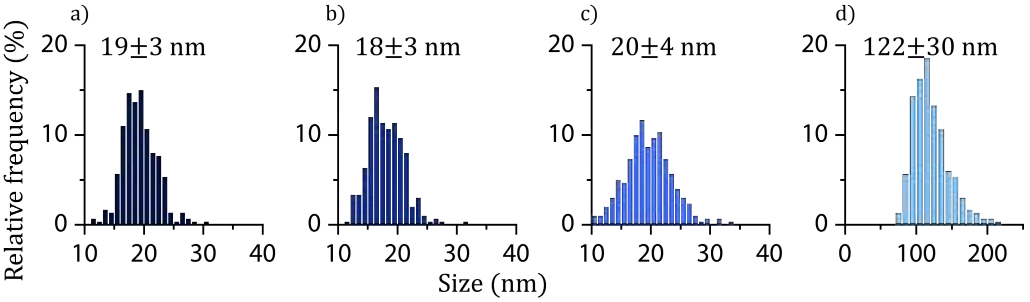

Figure 3.7: Distributions of nanostructures widths obtained at 270 °C after a) 30 min, b) 60 min, c) 90 min and d) 120 min. Data determined by analysing TEM images.

In Figure 3.8 XRD patterns of samples obtained at 270 °C after different growth time are shown.

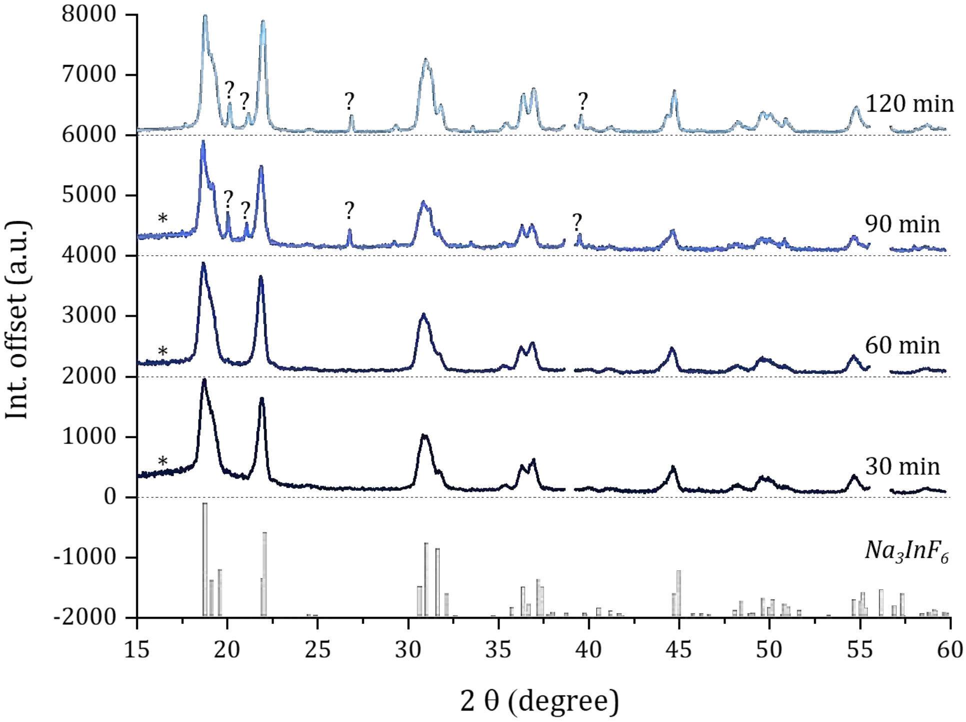

Figure 3.8: XRD patterns of samples obtained at 270 °C after 30 min, 60 min, 90 min and 120 min. Asterisks mark the broad signal typical for amorphous materials. Question marks indicate reflections associated with the unknown phase(s).

On the basis of the results presented for the samples obtained at 270 °C it can be seen that there are no significant changes between samples obtained after 30 and 60 minutes of growth. Exceeding the hour of nanocrystal growth, the presence of large nanoparticles (approximately 150 nm) can be observed in the TEM images and the presence of additional reflections not associated to the monoclinic phase of Na_3InF_6. It should be stressed that in all the diffraction patterns reported in this thesis work, the data for the angles 38.6-39.9°and 55.8-56.2°were removed since two reflections of sodium fluoride are located in these two positions which, as already mentioned, is a byproduct of the reaction. The complete diffraction patterns from 15 °to 60 °are shown in the appendix4.1. The omission of these small angular gaps in the diffraction patterns was done in order to show the clearest possible results by focusing only on determining the ideal temperature and growth time.

In Figure 3.9 TEM images of samples obtained at 280 °C after different growth time are shown.

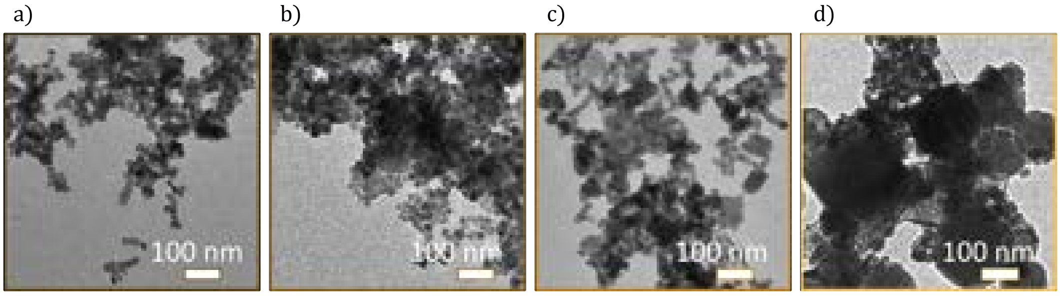

Figure 3.9: TEM images of samples obtained at 280 °C after a) 30 min, b) 60 min, c) 90 min and d) 120 min. Accelerating voltage of 60kV.

In Figure 3.10 and 3.11 size distributions of samples obtained at 280 °C after different growth time are shown.

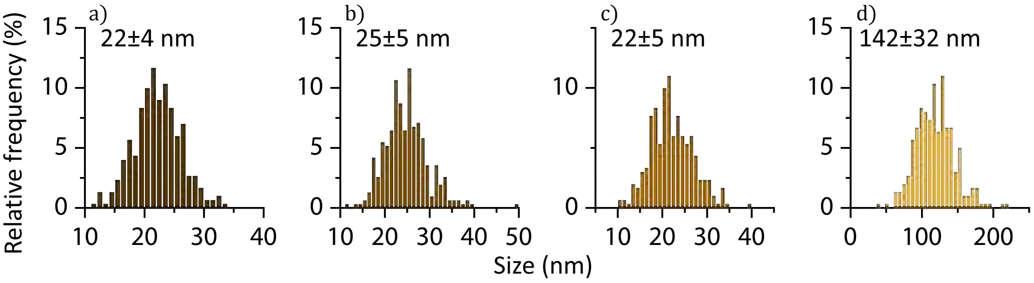

Figure 3.10: Distributions of nanostructures lengths obtained at 280 °C after a) 30 min, b) 60 min, c) 90 min and d) 120 min. Data determined by analysing TEM images.

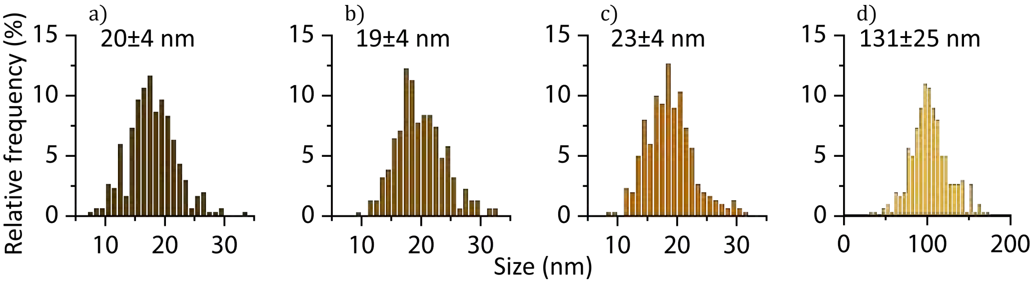

Figure 3.11: Distributions of nanostructures widths obtained at 280 °C after a) 30 min, b) 60 min, c) 90 min and d) 120 min. Data determined by analysing TEM images.

In Figure 3.12 XRD patterns of samples obtained at 280 °C after different growth time are shown.

No significant changes between the samples obtained after 30 and 60 minutes of nanocrystal grown at 280 °C, as for the previous temperature also at 270 °C. However, upon exceeding the hour of nanoparticles growth, the presence of large nanoparticles can be observed again in the TEM images and, above all, the presence of

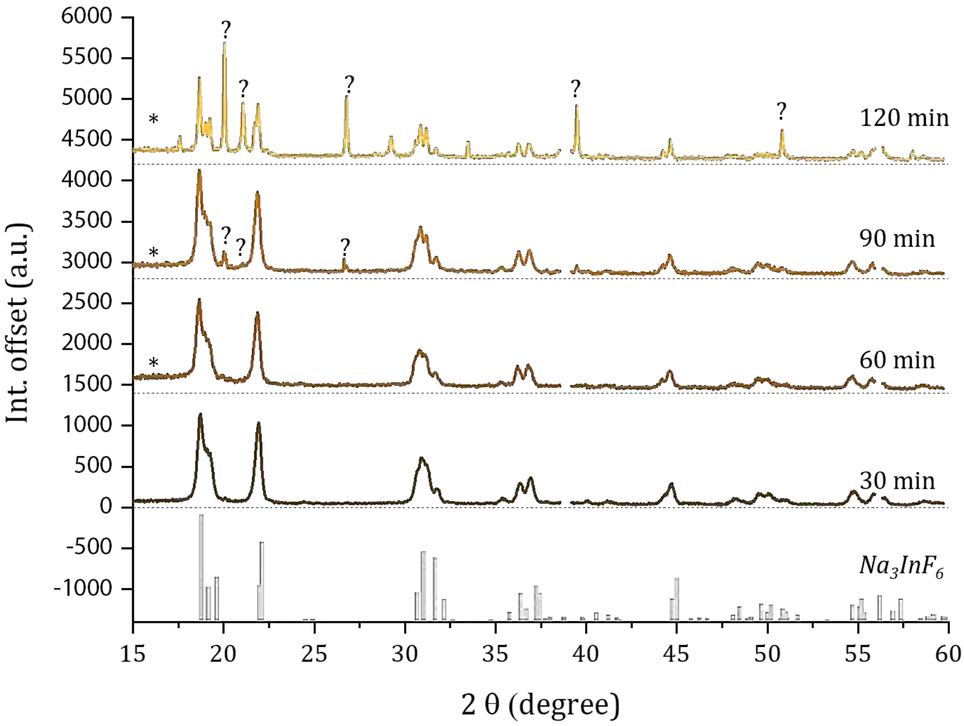

Figure 3.12: XRD patterns of samples obtained at 280 °C after 30 min, 60 min, 90 min and 120 min. Asterisks mark the broad signal typical for amorphous materials. Question marks indicate reflections associated with the unknown phase(s).

additional reflections not associated with the monoclinic phase of Na_3InF_6 are still detected. In particular, after two hours of growth of the NCs, it can be seen that the intensity of the additional reflections is greater than the one observed at 270 °C. This can suggest that the formation of the new phase (or new phases) formed after at least one hour of reaction is favored at higher temperatures.

In Figure 3.13 TEM images of samples obtained at 290 °C after different growth time are shown.

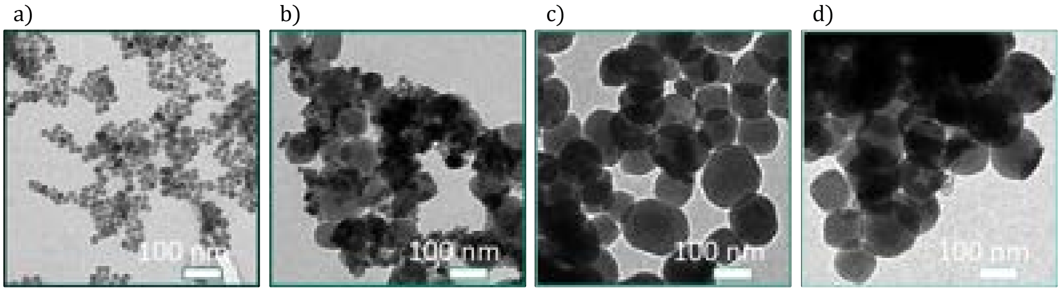

Figure 3.13: TEM images of samples obtained at 290 °C after a) 30 min, b) 60 min, c) 90 min and d) 120 min. Accelerating voltage of 60kV.

In Figure 3.14 and 3.15 size distributions of samples obtained at 290 °C after different growth time are shown.

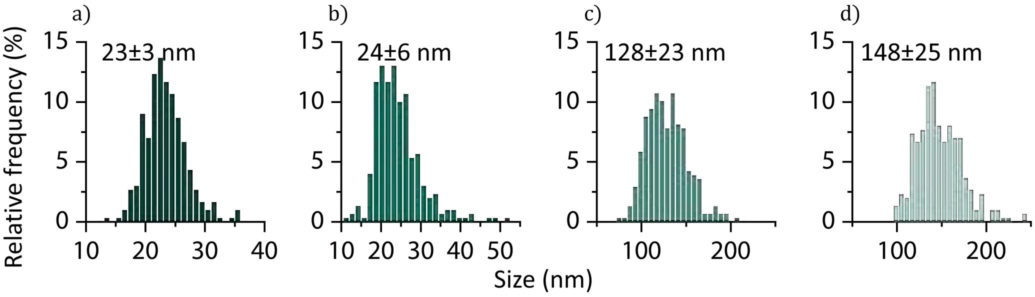

Figure 3.14: Distributions of nanostructures lengths obtained at 290 °C after a) 30 min, b) 60 min, c) 90 min and d) 120 min. Data determined by analysing TEM images.

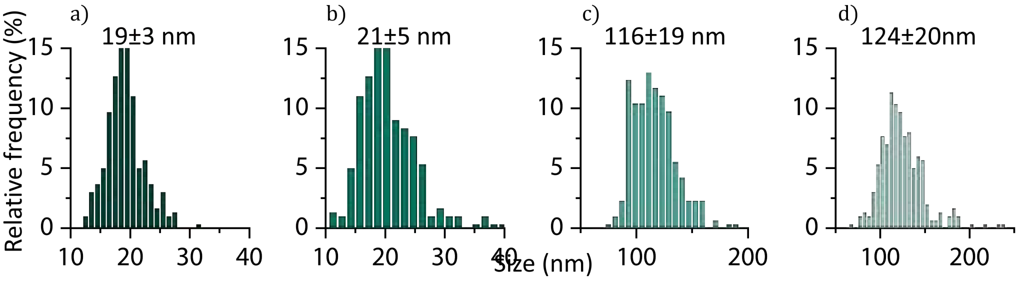

Figure 3.15: Distributions of nanostructures widths obtained at 290 °C after a) 30 min, b) 60 min, c) 90 min and d) 120 min. Data determined by analysing TEM images.

The trend noted at the previous two temperatures of no significant change between samples obtained after 30 and 60 minutes of nanocrystal growth was also maintained at 290 °C. Once again, extending the time of nanoparticle growth, the presence of large nanoparticles can be observed in the TEM images. At the 90-minute mark, almost only large-sized nanoparticles (around 130-150 nm) were visible from the TEM images. The diffraction patterns demonstrate how Na_3InF_6 in the monoclinic phase is obtained at 290 °C and short reaction times. From the comparison at short growth times it can be seen that the amorphous component at 290 °C is lower than at lower temperatures. It is probable that at higher growth temperatures, as a greater quantity of thermal energy is supplied during the formation of the crystalline lattices, a reduction in intrinsic structural defects may occur and therefore in all respects a better crystalline structure.

Regarding the additional phase(s) found after one hour of growth, XRD patterns of the samples obtained at 290 °C after 90 and 120 minutes appeared rather noisy, indicating a significant contribution of amorphous materials. While in XRD pattern, shown in Figure 3.12, the reflections associated to the monoclinic Na_3InF_6 can still be observed, they were almost imperceptible in XRD pattern of sample after two hours, Figure 3.16. The reflections with greater intensity in this last XRD pattern were associated with unknown phase(s). The diffraction patterns of

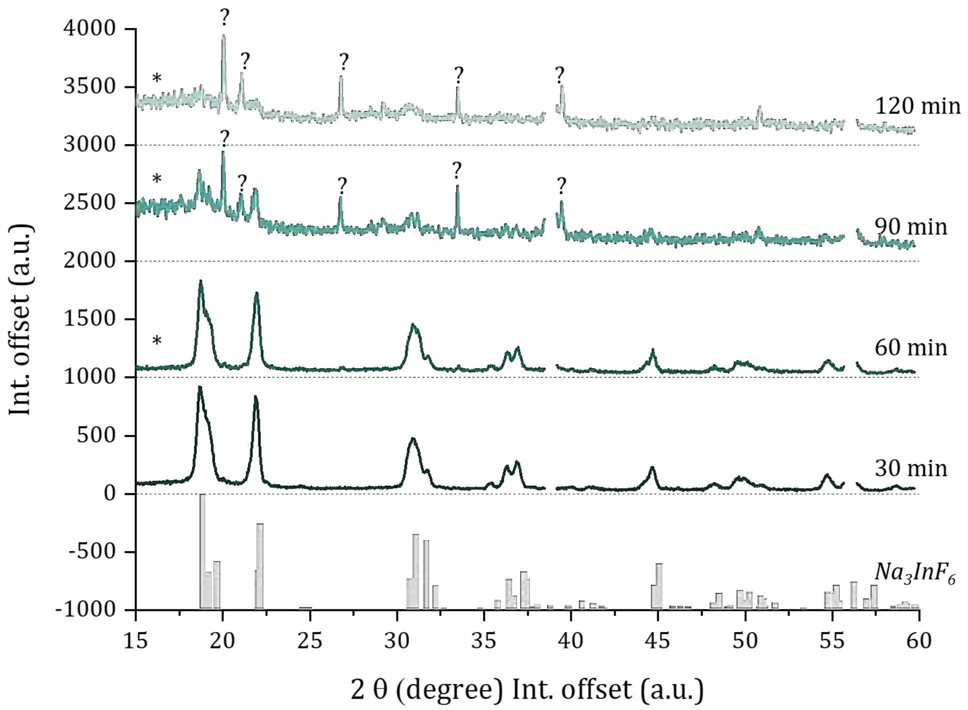

Figure 3.16: XRD patterns of samples obtained at 290 °C after 30 min, 60 min, 90 min and 120 min. Asterisks mark the broad signal typical for amorphous materials. Question marks indicate reflections associated with the unknown phase(s).

samples obtained at long nanoparticle growth times were compared in order to determine the unknown phase(s) with approximately 30 possible materials: NaF (cubic phase), InF_3 (trigonal phase), Na_3InF_6 (cubic phase), NaF_3 (tetragonal phase), Na_5InO_4 (both orthorombic phases), $Na_{21}In_5O_{15}$ (monoclinic phase), $Na_{24}In_5O_{15}$ (cubic phase), $NaInO_2$ (trigonal phase), $NaInO_3$ (cubic), In_2O_3 (one cubic, one hexagonal, two monoclinic and four orthorombic phases), InO (two monoclinic and one orthorombic phase), orthorombic InO_3, Na_2O (one cubic and two trigonal phases), Na_2O_2 (cubic and trigonal phases), NaO_2 (trigonal and cubic phases), InOF (orthorombic and triclinic phases) and $InOF_2$ (monoclinic phase). Despite this research, the exact unknown crystalline phase has not been identified yet. It is possible that the unassigned signals are a superposition of reflections deriving from different materials, probably metal oxides but, again, unambiguous determination of the phase(s) was not possible. In the future, a reaction can be carried out at very long times and then examine the resulting diffraction pattern. It is possible that by further extending the times we may notice a prevalence of one crystalline phase rather than another, thus favoring the identification of the materials obtained. Figure 3.17 shows a qualitative diagram that illustrates the transition from having only the reflections of the monoclinic phase of sodium indium fluoride (short reaction times) to have instead essentially those reflections associated with unknown phase(s) (long reaction times and higher temperature).

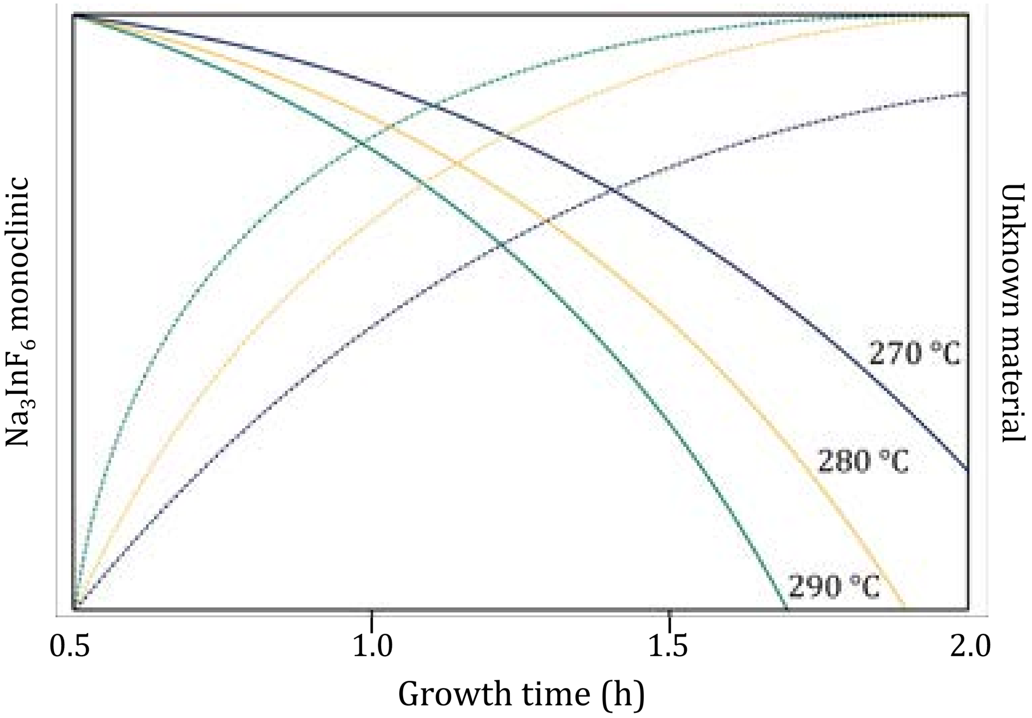

Figure 3.17: Qualitative schematic representation of the change in the crystalline phases contained in the samples. The diagram refers to the XRD patterns of samples obtained at different temperatures and reaction times. The solid lines represent the trend of the monoclinic Na_3InF_6, while the dashed lines represent that of the unknown phase(s). Blue, yellow and green lines mark temperatures 270, 280 and 290 °C respectively.

Concerning the optimal parameters for the preparation of Na_3InF_6 NCs in light of all the reported results, the synthesis temperature was selected at 290 °C since the contribution due to amorphous phases was less visible on XRD patterns compared to those at lower temperatures and 30 minutes was chosen as ideal growth time. In the diffraction pattern of the sample obtained at 290 °C after an hour of growth the peak of the unknown phase was visible (slightly), while at short growth times the only material obtained was Na_3InF_6 in the monoclinic phase (and the by-product not totally removed, cubic NaF).

As previously described, the main by-product formed during the synthesis of oleate-capped Na_3InF_6 NCs is sodium fluoride. This salt is difficult to remove as it is poorly soluble in both alcohol and water at room temperature. For this reason, during the washing steps of the nanoparticles with ethanol and/or methanol, most of the sodium fluoride precipitates together with the NCs. The separation between the nanoparticles and sodium fluoride was achieved immediately after the first re-dispersion of the sample in cyclohexane and oleic acid. The sample was centrifuged at low speed and the white pellet was discarded. However, as mentioned, two rather intense reflections associated with NaF were still observed in the diffraction patterns of some samples. With the aim of definitively separating the oleate-capped Na_3InF_6

nanoparticles from sodium fluoride, an additional purification procedure was determined in case the samples were not completely pure. The final sample containing also sodium fluoride was dispersed in a mixture of oleic acid and cylohexane (1:7) and it was centrifuged for five minutes at 2'000 g. After the centrifugation a certain quantity of white precipitate was visible on the bottom of the falcon tube, the supernatant was collected and subsequently analysed with X-ray diffraction. The patterns of two samples before and after this additional purification step are shown in Figure 3.18. The intensity of reflections due to sodium fluoride after precipitation is profoundly decreased (more than halved). However, even in the purified sample the sodium fluoride reflections remain observable. To remove completely sodium fluoride is probably required, besides this additional centrifugation step (NCs dispersed in oleic acid and cyclohexane), a purification of NCs in water (precipitation of NCs and removal of NaF dissolved in H_2O). The presence of such reflections is not diagnostic for quantitative assumptions given that the intensity of the signal in the diffraction patterns is not only dependent on the amount of crystalline phase, but also depends on the number of crystallites oriented along a specific direction.

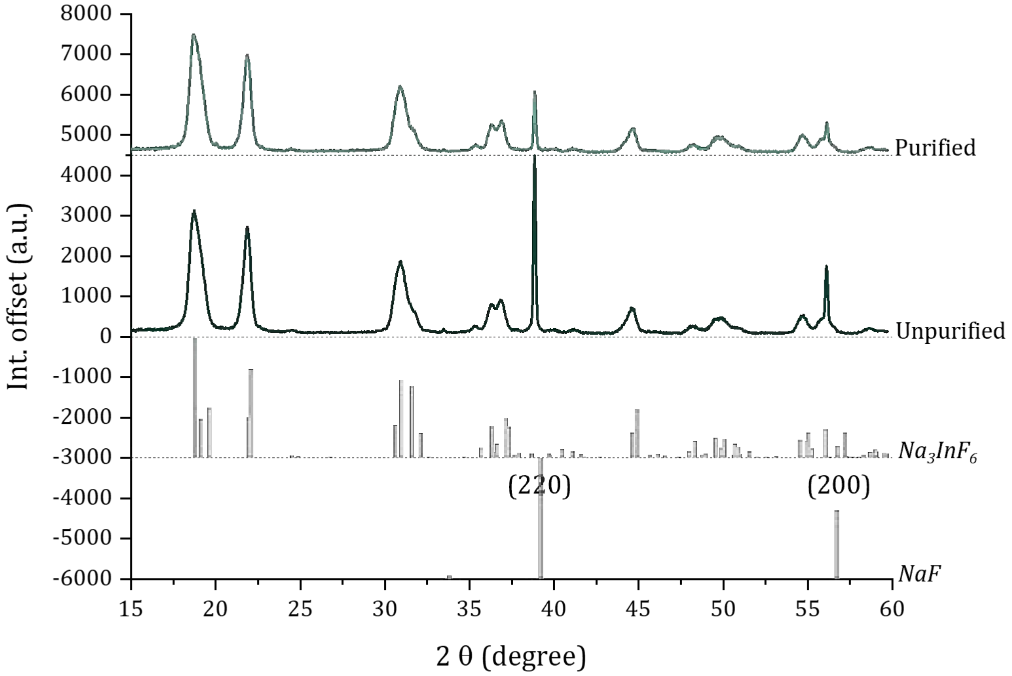

Figure 3.18: XRD patterns of oleate-capped NCs samples before (dark green) and after (light green) the addition purification step. Sodium fluoride (on the bottom of the graph) shows in the angular range 15-60°only two reflections associated to the family of planes [220] (tabulated value of 2 θ=39.38°) and [200] (tabulated value of 2 θ=56.94°). In the middle is also shown in grey the reference pattern of Na_3InF_6.

As explained in Chapter 1, Na_3InF_6 has all the ideal characteristics to act as an excellent and versatile host material for luminescent ions. To prove this ambivalent

ability of Na_3InF_6 as host for both lanthanide ions and transition metals, NCs were doped with Cr(III) and Nd(III) with concentrations of 2% or 5%. These concentrations were chosen arbitrarily. Doping ion concentrations in luminescent NCs less than 10% are preferable to reduce concentration quenching.
In Figure 3.20 TEM images of samples obtained at 290 °C and 30 minutes of reaction time with different percentages of dopant ions are shown. The TEM image of sample doped with 2% of Cr(III) is not reported given that the sample probably contained a great amount of NaF (by-product) preventing the view of Na_3InF_6 NCs through the TEM.

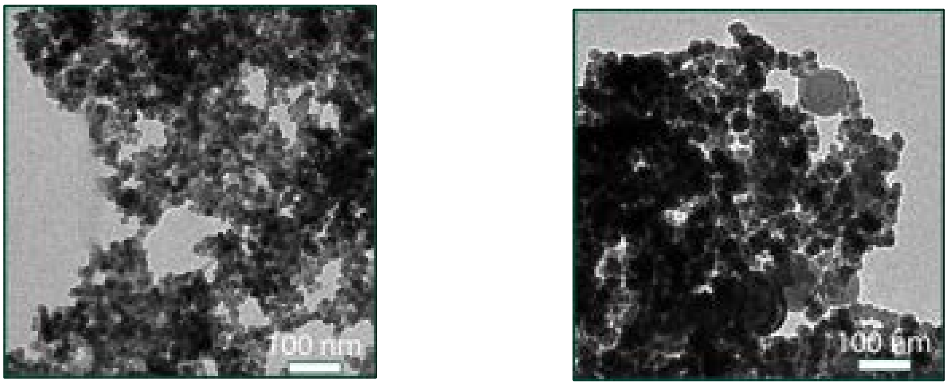

(a) 5% Cr(III) oleate-capped Na_3InF_6 NCs.

(b) 5% Nd(III) oleate-capped Na_3InF_6 NCs.

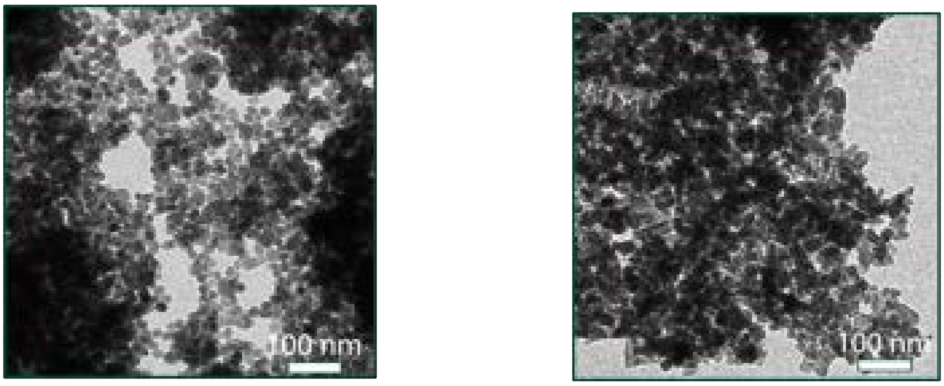

(a) 2% Nd(III) oleate-capped Na_3InF_6 NCs.

(b) 2% Nd(III) 5% Cr(III) oleate-capped Na_3InF_6 NCs

Figure 3.20: TEM images of doped and codoped samples obtained at 290 °C and 30 minutes of reaction time. Images obtained at 60kV of accelerating voltage.

In Figure 3.21 XRD patterns of undoped, doped –either with chromium (III) or neodymium(III)–and co-doped are shown.[1]

It can be seen that diffraction patterns resemble each other visually, especially those doped and undoped. There is a slight difference in terms of signal width when

---

[1] The doping percentages are referred to the molar ratio between Indium(III) and dopant ions and not in terms of number of dopant ions.

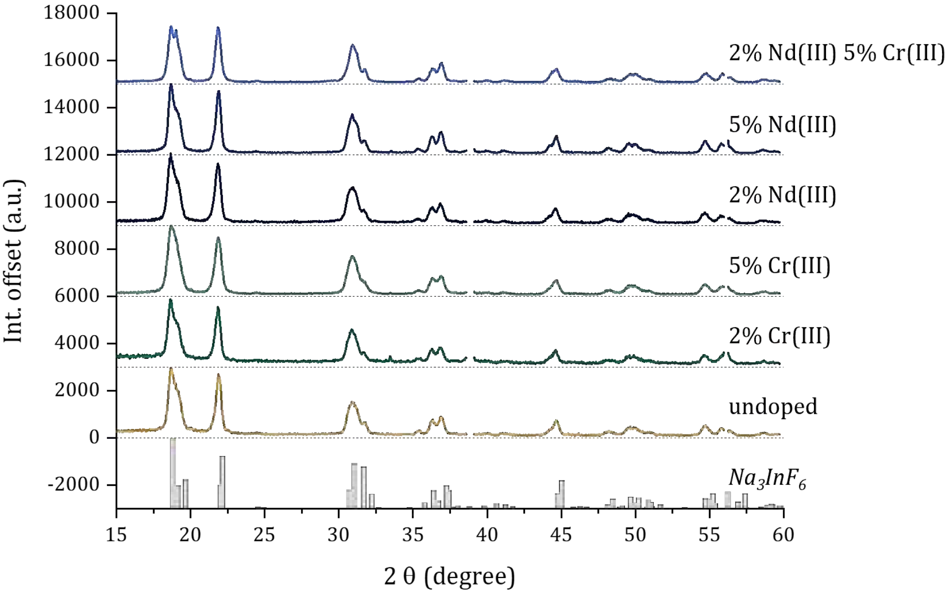

Figure 3.21: XRD pattern of undoped, doped and co-doped oleate-capped Na_3InF_6 NCs obtained with heating rate ∼ 7 °C/min, at 290 °C after 30 minutes of growth.

comparing the pattern of the undoped sample with the doped samples, except for the sample doped with 2% neodymium where the broadening of the reflections is comparable to that derived from the undoped sample. The broadening of the signals in diffraction patterns is a hallmark of nanomaterials. As can be seen in Figure 3.18, the difference in terms of signal width between the Na_3InF_6 and sodium fluoride signals is appreciable. The reflections associated with sodium fluoride are very narrow, in fact the crystallites had dimensions varying from hundreds of nanometers to a few micrometres. While the sizes of the Na_3InF_6 NCs are certainly much smaller and in fact the signals are much broader. A further broadening of the reflections in the doped samples compared to the undoped one is therefore indicative of a smaller size of the NCs themselves.

In addition, it is possible to observe a clear difference between the co-doped sample and all the other undoped or doped samples in the 2 θ range from 18°to 23°of the XRD patterns, shown in Figure 3.22. The relative intensity between the reflection planes (011) and (100) differs in the co-doped oleate-capped Na_3InF_6 NCs compared to the others. This can suggest the presence of a preferential growth axis parallel with (100) crystallographic orientation for this nanomaterials.

It would be interesting in the future to further analyze the diffraction patterns to determine whether there are variations in the cell parameters due to the replacement of indium with larger (trivalent neodymium) or smaller (trivalent chromium) ions. In addition, it should be also possible to estimate the size of the crystallites from the analysis of the broadening of the signals in diffraction patterns.

As it can be seen, however, the synthesis conditions chosen during the optimization of the procedure (heating rate, temperature and growth time) appear to be optimal.

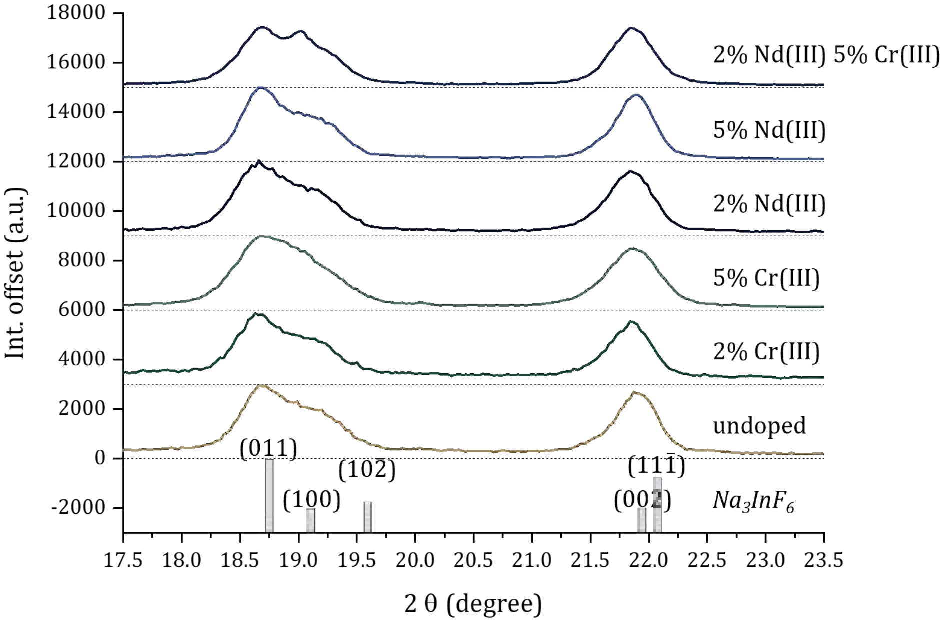

Figure 3.22: Zoom of the reflections in XRD patterns of undoped, doped and codoped oleate-capped Na_3InF_6 NCs obtained with heating rate ∼ 7 °C/min, at 290 °C after 30 minutes of growth.

There is a negligible contribution from amorphous phases and no signals of the unknown phase(s) in the diffraction patterns of doped or codoped materials. In the case of the sample doped with 2% with Cr(III) compared to XRD pattern of other samples, a more marked (but still not very intense) presence of amorphous can be detected. However, this sample was made with a different heating mantle so it is possible that the growth conditions were not the same (in particular heating rate and temperature fluctuations during sample preparation).

Surface functionalization and phase transfer of colloidal NCs were also explored while trying to preserve the size and shape of the NCs. The procedure was inspired by two protocols already available in the literature.[131, 132] As illustrated in Chapter 1, Na_3InF_6 NCs have been studied in this thesis work presuming a future application purpose in the biomedical field. Therefore, it was necessary to transfer these nanoparticles into a dispersing medium more similar to biological applications, i.e. water.

Indium(III) ions on the surface of the nanoparticles interact electrostatically with oleate molecules. Oleate is a ligand with a high affinity towards apolar dispersing media, thus oleate-capped Na_3InF_6 NCs were dispersed in cyclohexane. In order to transfer the various samples to an aqueous milieu, the organi hydrophobic ligad should be removed from the surface of the NCs and they should be replaced with ligands with affinity towards polar media.

Experimentally, oleate molecules were removed with the use of triethyloxonium tetrafluoroborate $EtO_3{}^+BF_4{}^-$. This reagent is made up of a strong cation $EtO_3{}^+$ and

an anion BF_4^-,which is able to replace the original organic ligands attached to the surface of the NCs while maintaining neutrality of the NCs surface and thus also their stability. EtO_3^+ cations stabilise the carboxylate ion of the oleate molecules. Therefore, Na_3InF_6 NCs after the reaction results capped with various BF_4^- ions enabling the dispersions of NCs in hydrophilic media such as N,N-dimethylformamide. Conversely, the various free oleate molecules neutralised by the ions EtO_3^+ remain dissolved in the hydrophobic medium (cyclohexane).
Once these BF_4^--capped Na_3InF_6 NCs were obtained, it was possible to replace the BF_4^- ions with ligands with affinity towards aqueous media. The binding affinity between In(III) ions on the NCs surface and BF_4^- is weak so the replacement of these anions with a different polar ligand usually happens without issues. Citrate was chosen as hydrophilic ligands for the transfer of the BF_4^--capped Na_3InF_6 NCs into aqueous media. Citrate ion has three COO^- groups, so it can act as tridentate ligands, although it can also act as bidentate due to steric hindrance. DLS was used in order to obtain information on the aggregation state of nanoparticles in different dispersion media. In order to optimise the transfer of oleate-capped Na_3InF_6 NCs into the aqueous phase, different attempts were carried out. Both the ideal amounts of Meerwein's salt for oleate stripping and methods of treating the sample were studied. In Figure 3.24, four DLS spectra are shown, for each sample are reported three repeated intensity-based and numeric-based size distributions. In Figure 3.24a, the DLS spectra of citrate-capped Na_3InF_6 NCs in DI water obtained by the stripping of oleate molecules using nitrosonium tetrafluoroborate, $NOBF_4$ is shown. This was the first attempt to transfer the oleate-capped Na_3InF_6 NCs into water, however, as can also be seen from the TEM images shown in Figure 3.23, the surface of NCs seemed almost abraded and NCs appeared shrunken after the treatment.

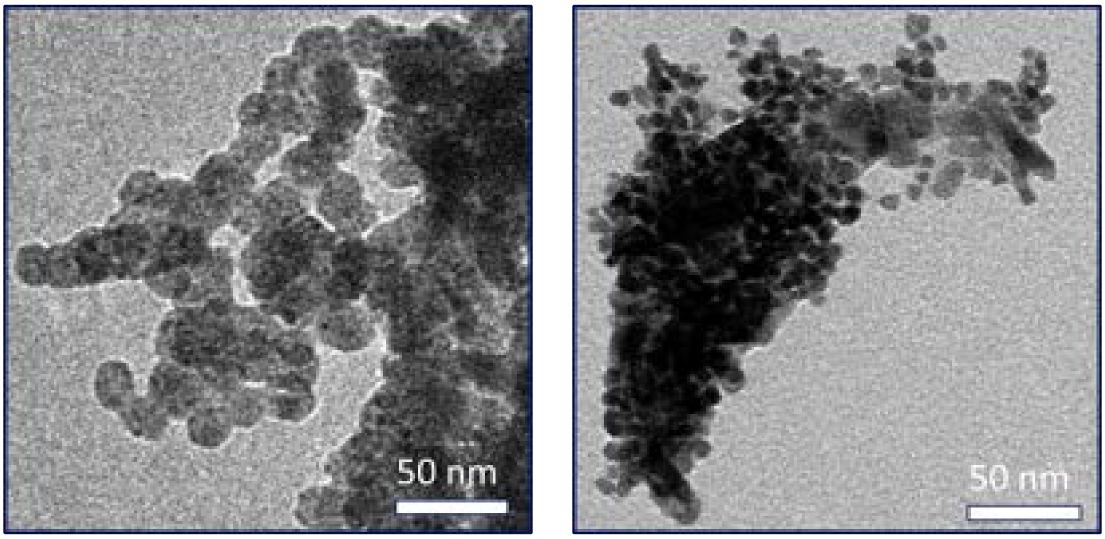

(a) Oleate-capped Na_3InF_6 NCs obtained after 30 min at 270 °C.

(b) Citrate-capped Na_3InF_6 NCs obtained by oleate stripping with $NOBF_4$.

Figure 3.23: TEM images obtained at an accelerating voltage of 60 kV.

In addition, the relative frequency of objects with great size ($>$ 100 nm) is higher for the sample with chNa3InF6 NCs coated with citrate in water (treated with

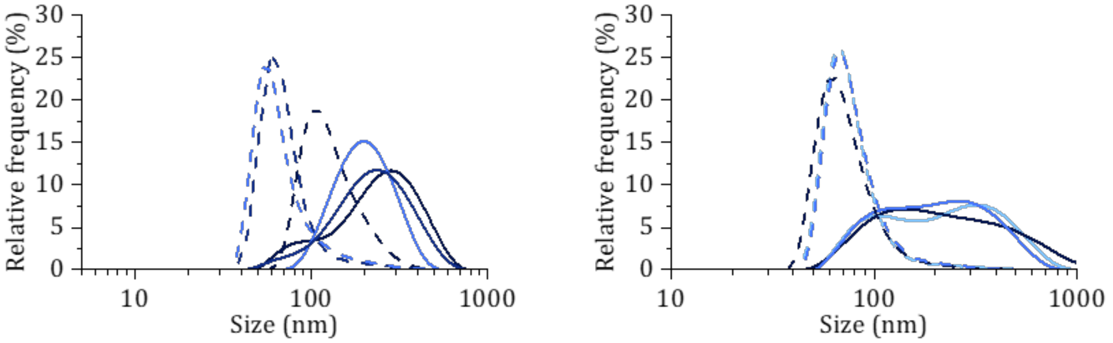

(a) Citrate-capped Na$_3$InF$_6$ NCs in water, oleate stripping with NOBF$_4$.

(b) Oleate-capped Na$_3$InF$_6$ NCs in cyclohexane and oleic acid.

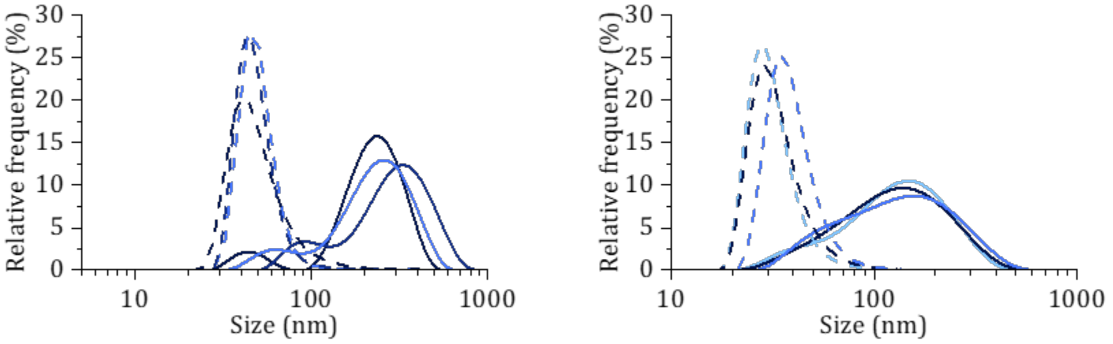

(c) Citrate-capped Na$_3$InF$_6$ NCs in water obtained by oleate stripping with EtO$_3$BF$_4$(10 minutes of reaction under stirring and 5x excess of reagent).

(d) Citrate-capped Na$_3$InF$_6$ NCs in water obtained by oleate stripping with EtO$_3$BF$_4$ (1 minute of reaction and 6x excess of reagent).

Figure 3.24: DLS intensity size distributions (solid lines) and number size distributions (dashed lines) of different Na$_3$InF$_6$ NCs.

chNOBF4, Figure 3.24a) compared to the sample containing chNa3InF6 NCs coated with oleate dispersed in cyclohexane, Figure 3.24b. This can indicate a more significant presence of aggregates in dispersion. In conclusion, the NCs after this first water transfer attempt appeared with a less homogeneous surface and more aggregated. These results suggested that the reagent (NOBF$_4$) used was too strong and caused abrasion of the NCs surface. For this reason it was then decided to use Meerwein's salt for the oleate stripping instead of NOBF$_4$. DLS spectra of citrate-capped Na$_3$InF$_6$ NCs obtained with different amount of EtO$_3$BF$_4$ and different contact time with the reagent are shown in Figure 3.24c and 3.24d. Even in these two samples in water the intensity size distributions showed a greater relative frequency suggesting the presence of aggregates within dispersions.

In order to find the optimal transfer conditions in water, 12 different samples were made by varying the quantities of reagent (excess of 2.5, 1.25 and 0.75 times) and the reaction time (0, 3, 6, 9 minutes). The intensity and number size distributions of the sample obtained with higher excess of reagent and longer reaction time are reported below, see Figure 3.25. As it can be seen from the intensity size distributions, there is also in this case the presence of aggregates with a hydrodynamic diameter of about 110 nm, while the number size distributions suggested the presence of NCs between 14 and 19 nm, similar to the data obtained from the TEM images, see Figure 3.6 and 3.7. The DLS results of the other samples are not reported as they are not very conclusive. The water transfer of the NCs was certainly carried out however the optimal parameters were not definitively determined. However, so far the best results have been obtained with a 2.5x excess of reagent compared to the theoretical quantity of NCs and 9 minutes of reaction.

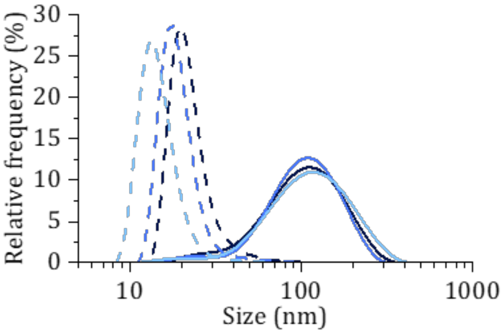

Figure 3.25: DLS intensity size distributions (solid lines) and number size distributions (dashed lines) of citrate-capped Na_3InF_6 NCs in water after stripping with EtO_3BF_4, reaction time of 9 minutes.

FTIR spectroscopy was used to verify that the crystals were capped with oleate when dispersed in cyclohexane and with citrate when in aqueous phase. The FTIR spectra of the free ligands, oleic acid and citrate respectively, and of the (dried) samples of oleate-capped and citrate-capped NCs are shown in Figure 3.26. The FTIR spectrum of the oleate-capped NCs compared with that of the free oleic acid indicated that the surface of the NCs in cyclohexane were surrounded by many molecules of oleate through the COO^- group. As it can be seen from Figure 3.26 the typical peak associated with the stretching of the C=O bond usually located at 1720 - 1680 cm^{-1} was observable in the spectrum of oleic acid, while it was absent in the spectrum of the experimental sample. While the asymmetric and symmetric stretching which usually give rise to peaks at ∼1'500 cm^{-1} and ∼1'400 cm^{-1} were observable in both FTIR spectra. In the region 3'000-2'800 cm^{-1} of both spectra, the stretching of the C-H bond, close to the double bond along the unsaturated chain, the symmetric and asymmetric stretching of the C-H bond in methylene group were visible. Finally, peaks associated with the bending of the C-H bonds appeared to be less intense in the case of oleate bound to the surface of NCs. These results suggested that the surface of the nanoparticles was decorated with oleate molecules through the COO^- group and that these molecules have less degrees of freedom when attached to the NC surface.

The FTIR spectrum of the citrate-capped NCs compared with that of the free trisodium citrate suggested that the surface of the NCs in water were surrounded by citrate through the COO^- groups, shown in Figure 3.26. In both FTIR spectra the typical broadened and rounded signal at approximately 3450 cm–1 generated by O-H stretching is clearly visible. However, the signal appeared broader in the FTIR spectrum of citrate-capped Na_3InF_6 NCs probably due to traces of water in the sample. The characteristic peaks at 1'400 cm^{-1} and 1'440 cm^{-1} correspond

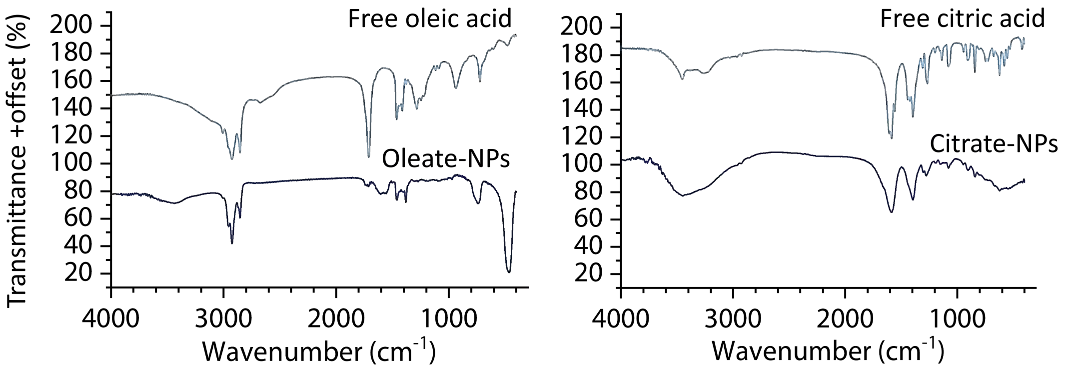

(a) Free oleic acid and oleate-capped Na_3InF_6 NCs.

(b) Free trisodium citrate and citrate-capped Na_3InF_6 NCs.

Figure 3.26: FTIR spectra of the same samples before and after the surface functionalization, and of two associated free ligands.

to the symmetric and asymmetric stretching of COO^- confirming the electrostatic interaction between citrate and nanoparticles. The presence of fewer signals in the spectrum of the nanoparticles compared to that of the free trisodium citrate, as in the case of oleate-capped NCs, was also ascribed to the limited mobility of the molecules when bound to the surface of the NC. In conclusion, the surface functionalisation of Na_3InF_6 NCs by oleate and by citrate ions was proven by FT-IR measurements.

The luminescent properties were explored by examining the excitation and emission spectra of the singly doped and co-doped samples at room temperature, see Figure ??. The luminescent properties of the sample doped with 5% chromium were the first to be evaluated. Since Cr(III) is very sensitive to the crystalline surroundings there was the possibility of not obtaining any signal. Figure 3.27a shows the PLE (dashed line) and PL (solid line) spectrum for this sample. The 5% Cr(III) oleate-capped Na_3InF_6 NCs exhibited three broad excitation bands (300-690 nm) and one emission band in the red-NIR range (700-850 nm). The excitation bands peaking at 333, 436 and 650 nm were ascribed to the ${}^4A_{2g} \rightarrow {}^4T_{1g}(P)$, ${}^4A_{2g} \rightarrow {}^4T_{1g}(F)$ and ${}^4A_{2g} \rightarrow {}^4T_{2g}(F)$ transitions of the Cr(III) ions, respectively. Upon excitation at 630 nm,5% Cr(III) oleate-capped Na_3InF_6 NCs displayed a NIR emission peaking at 772 and 788 nm which derived from the ${}^4T_2 \rightarrow^4 A_{2g}$ transitions of Cr(III).

The oleate-capped Na_3InF_6 NCs were thus found to be an effective host material for Cr(III). To assess if the co-doped sample also exhibited Cr(III) luminescence, the PLE and PL spectra were recorded for this sample under the same conditions used above. As it can be seen in Figure 3.27b, the 2% Nd(III)/5% Cr(III) oleate-capped Na_3InF_6 NCs exhibited three broad excitation bands (300-690 nm) and one emission band in the red-NIR range like for the doped sample. Therefore, the luminescent properties of the co-doped sample were proven for Cr(III).

Subsequently, the PL spectra of the 2% Nd(III) and codoped sample were also recorded to evaluate the emission of the lanthanide ion when incorporated into the oleate-capped Na_3InF_6 NCs. As mentioned in chapter 1, Nd(III) is usually excited

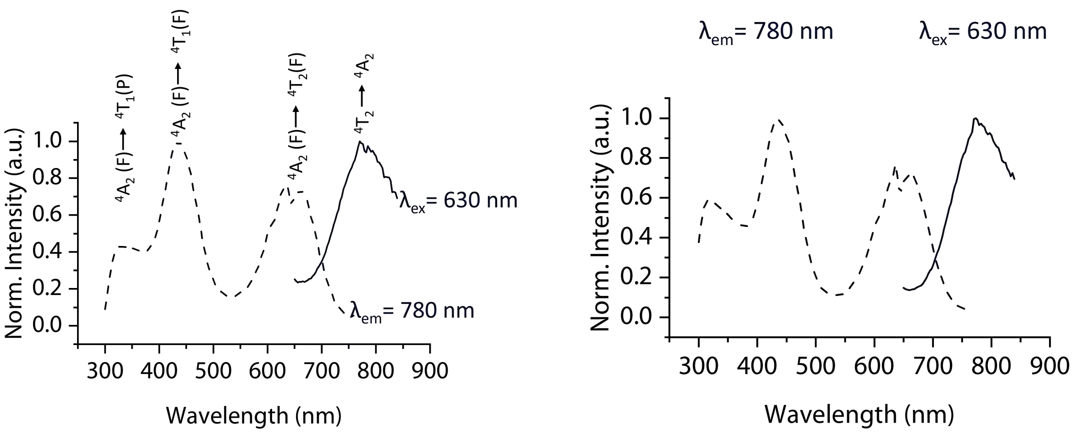

(a) 5% Cr(III) oleate-capped Na_3InF_6 NCs. The normalised PL spectrum was recorded with 630 nm excitation. The normalised PLE was monitored at a fixed wavelength of 780 nm.

(b) 2% Nd(III) 5% Cr(III) oleate-capped Na_3InF_6 NCs. The normalised PL spectrum was recorded with 630 nm excitation. The normalised PLE was monitored at a fixed wavelength of 780 nm.

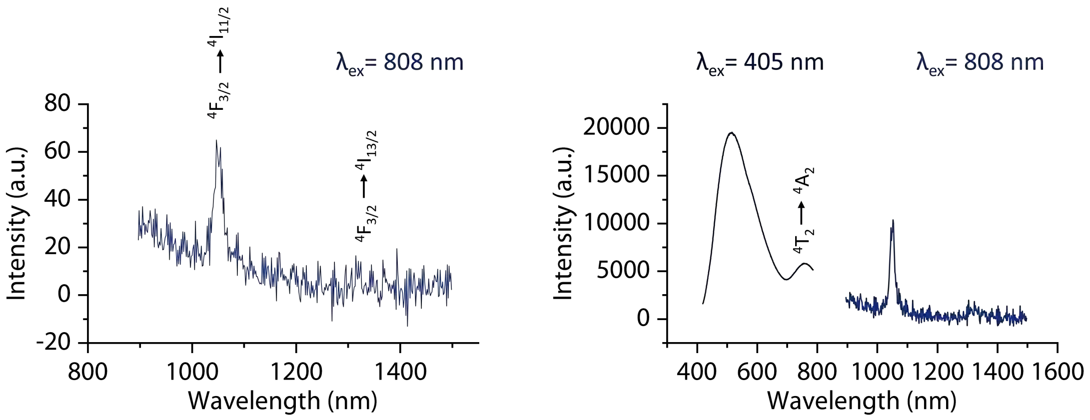

(c) 2% Nd(III) oleate-capped Na_3InF_6 NCs. PL spectrum obtained upon excitation at 808 nm.

(d) 2% Nd(III) 5% Cr(III) oleate-capped Na_3InF_6 NCs. PL spectra obtained upon excitation at 405 nm (left) and 808 nm (right).

Figure 3.27: PL (solid lines) and PLE (dashed lines) spectra of doped and co-doped samples obtained with FS5 spectrofluorometer (spectra on the top) or Ocean Optics Spectrometer (spectra on the bottom).

with lasers with a wavelength of 750-850 nm. Here, the laser used had a wavelength of 808 nm. 2% Nd(III) oleate-capped Na_3InF_6 NCs exhibited three narrow emission bands peaking at 1048 and 1395 nm were ascribed to the $^4F_{3/2} \rightarrow ^4 I_{11/2}$ and $^4F_{3/2} \rightarrow ^4 I_{13/2}$ transitions of Nd(III), respectively as can be seen in Figure 3.27c.
Finally, the PL spectra of 2% Nd(III) 5% Cr(III) oleate-capped Na_3InF_6 NCs in Figure 3.27d obtained upon excitation at 405 nm, to excite Cr(III), and at 808 nm, to excite Nd(III), proved the incorporation of both doping ions. The same sample, depending on the excitation wavelength used, showed emission in the red-NIR (700-

850 nm) or in the NIR range (1000-1100 and 1300-1400).
These results in terms of luminescence prove the versatility of Na_3InF_6 NCs as host nanomaterial for the incorporation of both transition metals and lanthanides.

Doped and co-doped oleate-capped Na_3InF_6 NCs were further analysed through high-resolution transmission electron microscopy (HR-TEM) and selected area electron diffraction (SAED). HRTEM micrograph were obtained using a JEOL HRTEM operated at 200 kV.

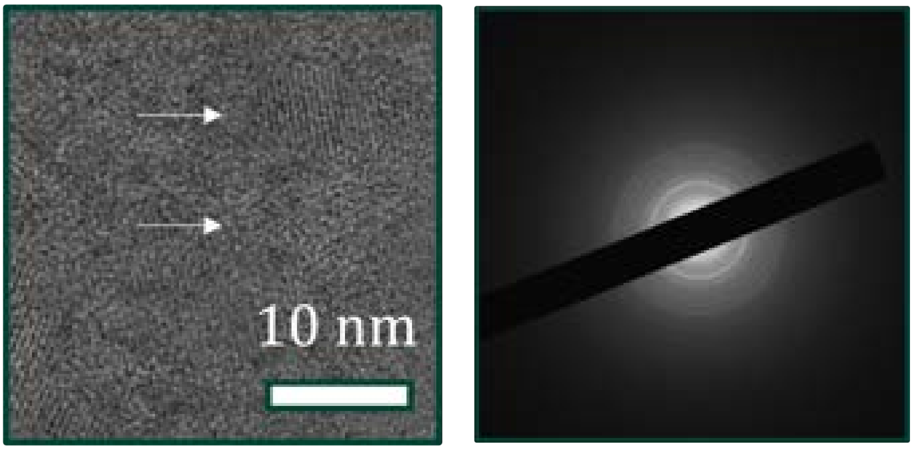

Figure 3.28: HRTEM micrograph (left) and SAED pattern of 5% Cr(III) oleate-capped Na_3InF_6 NCs. The white arrow marks NC.

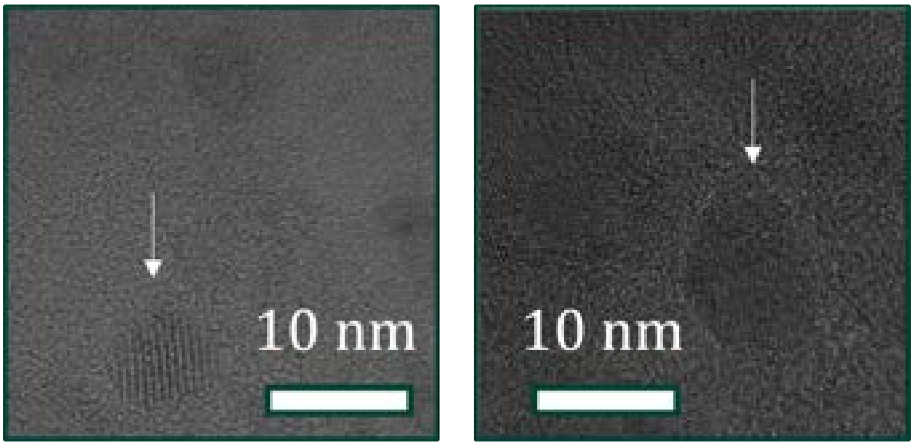

Figure 3.29: HRTEM micrographs 2% Nd(III) oleate-capped Na_3InF_6 NCs. The white arrow marks NC.

Both HRTEM images and SAED pattern of doped and co-doped NCs further proved that the obtained samples were crystalline. The SAED pattern showed several rings made up of numerous bright points, each of them originated by a Bragg plane in a single crystallite, indicating the poly-nanocrystalline nature of samples. The SAED pattern for 5% Cr(III) oleate-capped Na_3InF_6 NCs is reported in Figure 3.28. From the HRTEM micrographs show in Figure 3.29 and 3.30 can be observed as the sizes of the Na_3InF_6 NCs appeared smaller than those obtained from the TEM images

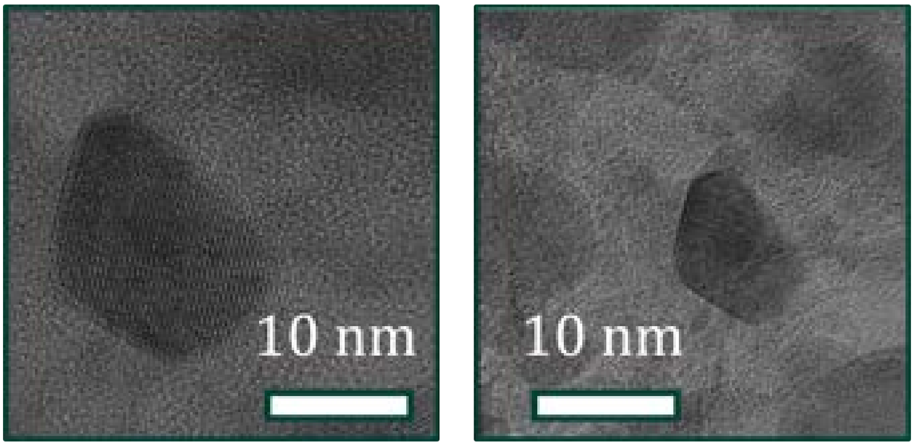

Figure 3.30: HRTEM micrographs 2% Nd(III) 5% Cr(III) oleate-capped Na_3InF_6 NCs. The white arrow marks NC.

and DLS spectra. However, the number size distributions obtained through DLS referred to hydrodynamic diameters and it is not uncommon that these sizes are slightly larger than the diameters of dried NCs. The presence of organic ligands (oleate) on the surface of the Na_3InF_6 NCs might have caused the measurement of sizes that do not refer to the individual nanocrystallite, but rather to the oleate-capped NC. In the future, to uniquely measure the sizes of Na_3InF_6 NCs, HRTEM analyses might be carried out on samples containing NCs without oleate molecules on the surface (after having optimised the conditions for the transfer of NCs into water). Otherwise, as mentioned, the sizes of the Na_3InF_6 NCs might be estimated by refining and analysing the reflections on XRD patterns.

Conclusion

In this thesis work, the experimental procedure to synthesize undoped, doped and codoped Na_3InF_6 nanocrystals has been illustrated in detail. The Na_3InF_6 NCs were grown by co-precipitation in a binary solvent mixture of oleic acid and 1-octadecene. The oleic acid played a dual role: as solvent and capping ligand stabilising the synthesised NCs in organic solvents. The surface of the synthesized NCs was also functionalized to make them water-compatible through a ligand exchange approach (from oleate to citrate). The results obtained by TEM, HR-TEM, SAED and XRD proved that the experimentally obtained samples consisted of nanometric monoclinic Na_3InF_6 crystallites. Furthermore, after preparing the appropriate precursors of the chosen lanthanide ion and transition metal (Nd(III) and Cr(III)), doping of the NCs with variable concentrations of luminescent dopants was performed. The suitable size, charge, and crystal size occupied by indium ions make the incorporation of both these ions in Na_3InF_6 nanocrystals possible. Succesful doping was demonstrated for doped and co-doped samples through PLE and PL measurements. These results proved the versatility of Na_3InF_6 in terms of possibility to dope simultaneously Nd(III) and Cr(III). This ability of dual doping may allow in the future to obtain innovative and intriguing optical properties from the synergistic effect of different ions. From the standpoint of future prospects, the surface of such NCs may be functionalized with an epitaxial layer of Na_3InF_6, other inorganic materials, or with biocompatible ligands to enhance the NCs' luminescent properties and make them amenable to biomedical applications. Future studies will also entail the exploration of different Cr(III) and Nd(III) concentrations, the incorporation of other luminescent lanthanide and transition metal ions, as well as the study of the luminescence of these NCs as a function of temperature to extract quantitative information about the physical mechanisms underpinning their optical properties. Upon optimization of these nanomaterials, future possible applications include their use as luminescent probes in biological samples, in 3D visualizations, and in solar energy conversion.

Bibliography

[1] E. Wiedemann, *Annalen der Physik* **1888**, *270*, 446–463.

[2] B. Henderson, G. F. Imbusch, *Optical spectroscopy of inorganic solids*, Oxford University Press, **1989**.

[3] N. W. Ashcroft, N. D. Mermin, *Solid State Physics*, Saunders College Publishing, **1976**.

[4] S. Jacquemoud, S. Ustin, *Leaf Optical Properties*, Cambridge University Press, **2019**.

[5] J. M. Hollas, *Modern Spectroscopy*, 4th edition, Wiley, **2004**.

[6] R. Hilborn, *Am. J. Phys.* **2002**, *50*, Revision of: Hilborn, R.C. Am. J. Phys. 50, 982–986 (1982), DOI `10.1119/1.12937`.

[7] A. Tokmakoff, Class Lecture - 4.4 Rate of Absorption and Stimulated Emission, **2005**.

[8] R. P. P. Encyclopedia, Absorption coefficient, 2023-09-16.

[9] J. A. DeLuca, *Journal of Chemical Education* **1980**, *57*, 541.

[10] K.-L. Wong, J.-C. G. Bünzli, P. A. Tanner, *Journal of Luminescence* **2020**, *224*, 117256.

[11] Q. Li, R. Jin, *Nanotechnology Reviews* **2017**, *6*, 601–612.

[12] T.-Q. Yang, B. Peng, B.-Q. Shan, Y.-X. Zong, J.-G. Jiang, P. Wu, K. Zhang, *Nanomaterials (Basel)* **2020**, *10*, 261.

[13] X. Li, X. Gao, X. Zhang, X. Shen, M. Lu, J. Wu, Z. Shi, V. L. Colvin, J. Hu, X. Bai, W. W. Yu, Y. Zhang, *Advanced Science* **2021**, *8*, 2003334.

[14] A. Sternig, J. Bernardi, K. Mckenna, O. Diwald, *Journal of Materials Science* **2015**, *50*, DOI `10.1007/s10853-015-9393-2`.

[15] Y. Yamada, Y. Kanemitsu, *Journal of Luminescence* **2013**, *133*, 16th International Conference on Luminescence ICL'11, 30–34.

[16] X. Cao, C. Ding, C. Zhang, W. Gu, Y. Yan, X. Shi, Y. Xian, *J. Mater. Chem. B* **2018**, *6*, 8011–8036.

[17] R. Marin, A. Skripka, L. V. Besteiro, A. Benayas, Z. Wang, A. O. Govorov, P. Canton, F. Vetrone, *Small* **2018**, *14*, 1803282.

[18] R. Marin, A. Benayas, N. Garcia, J. Lifante, J. Yao, D. Mendez-Gonzalez, F. Sanz-Rodriguez, J. Rubio-Retama, L. Vazquez Besteiro, D. Jaque, *Advanced Photonics Research* **2021**, *3*, 2100260.

[19] M. Parvizian, J. De Roo, *Nanoscale* **2021**, *13*, 18865–18882.

[20] X. Peng, Y. Lv, L. Fu, F. Chen, W. Su, J. Li, Q. Zhang, S. Zhao, *RSC Adv.* **2021**, *11*, 34095–34100.

[21] J. Liu, R. Li, B. Yang, *ACS Central Science* **2020**, *6*, 2179–2195.

[22] C. Loubna, D. Hamana, M. Manso-Silván, S. Achour, *Applied Physics A* **2022**, *128*, DOI `10.1007/s00339-022-05731-6`.

[23] N. Shiran, I. Boiaryntseva, A. Gektin, S. Gridin, V. Shlyakhturov, S. Vasyukov, *Materials Research Bulletin* **2014**, *59*, 13–17.

[24] V. Vaněček, J. Páterek, R. Král, R. Kučerková, V. Babin, J. Rohlíček, R. Cala', N. Kratochwil, E. Auffray, M. Nikl, *Optical Materials: X* **2021**, *12*, 100103.

[25] M. Dramićanin, *Luminescence Thermometry*, Woodhead Publishing, **2018**.

[26] A. D. McNaught, A. Wilkinson, *Blackwell Scientific Publications* **1997**, *2nd ed. (the "Gold Book")*, DOI `https://doi.org/10.1351/goldbook`.

[27] W. H. R.A. Mackay, K.M.Mackay, *Introduction to Modern Inorganic Chemistry, 6th edition*, CRC Press, **2017**.

[28] A. G. Housecroft, Catherine E.; Sharpe, *Inorganic Chemistry*, 5th edition, **2018**.

[29] R. M. Eisberg, *Quantum physics of atoms solids, molecules, nuclei and particles*, 2nd edition, John Wiley and Sons (WIE), Brisbane, QLD, Australia, **2007**.

[30] J.-B. Lu, X.-L. Jiang, H.-S. Hu, J. Li, *Journal of Chemical Theory and Computation* **2023**, *19*, 82–96.

[31] G. H. Dieke, H. M. Crosswhite, *Appl. Opt.* **1963**, *2*, 675–686.

[32] P. Peijzel, A. Meijerink, R. Wegh, M. Reid, G. Burdick, *Journal of Solid State Chemistry* **2005**, *178*, f-element Spectroscopy and Coordination Chemistry, 448–453.

[33] 23-09-2023.

[34] D. J. Jose Solé, Luisa Bausa, *An Introduction to the Optical Spectroscopy of Inorganic Solids*, Wiley, **2005**.

[35] L. Marciniak, K. Kniec, K. Elżbieciak-Piecka, K. Trejgis, J. Stefanska, M. Dramićanin, *Coordination Chemistry Reviews* **2022**, *469*, 214671.

[36] R. Marin, D. Jaque, *Chemical Reviews* **2021**, *121*, 1425–1462.

[37] C. Lee, Z. Bao, M.-H. Fang, T. Lesniewski, S. Mahlik, M. Grinberg, G. Leniec, S. M. Kaczmarek, M. G. Brik, Y.-T. Tsai, T.-L. Tsai, R.-S. Liu, *Inorganic Chemistry* **2020**, *59*, 376–385.

[38] K. Nchimi Nono, **2012**.

[39] 21-09-2023.

[40] H.-W. Chen, J.-H. Lee, B.-Y. Lin, S. Chen, S.-T. Wu, *Light: Science Applications* **2017**, *7*, 17168.

[41] A. K. Soni, B. P. Singh in *Luminescence*, (Ed.: S. Pyshkin), IntechOpen, Rijeka, **2019**, Chapter 1.

[42] K. Khanafer, K. Vafai in (Eds.: E. M. Sparrow, Y. I. Cho, J. P. Abraham, J. M. Gorman), Advances in Heat Transfer, Elsevier, **2013**, pp. 303–329.

[43] T.-Z. Ang, M. Salem, M. Kamarol, H. S. Das, M. A. Nazari, N. Prabaharan, *Energy Strategy Reviews* **2022**, *43*, 100939.

[44] 21-09-2023.

[45] Y. Hasegawa, Y. Kitagawa, *Journal of Photochemistry and Photobiology C: Photochemistry Reviews* **2022**, *51*, 100485.

[46] M. Jia, X. Chen, R. Sun, D. Wu, X. Li, Z. Shi, G. Chen, C. Shan, *Nano Research* **2023**, *16*, 2949–2967.

[47] C. Zhong, M. He, K. Lou, F. Gao in *Neurotoxicity of Nanomaterials and Nanomedicine*, (Eds.: X. Jiang, H. Gao), Academic Press, **2017**, pp. 227–257.

[48] J.-H. Kim, K. Park, H. Y. Nam, S. Lee, K. Kim, I. C. Kwon, *Progress in Polymer Science* **2007**, *32*, Polymers in Biomedical Applications, 1031–1053.

[49] S. Premcheska, M. Lederer, A. Kaczmarek, *Chemical Communications* **2022**, *58*, DOI `10.1039/D1CC07164E`.

[50] M. Nimbalkar, M. Yawalkar, N. Mahajan, S. Dhoble, *Photodiagnosis and Photodynamic Therapy* **2021**, *33*, 102082.

[51] G. Eskiizmir, Y. Baskın, K. Yapıcı in *Fullerens, Graphenes and Nanotubes*, (Ed.: A. M. Grumezescu), William Andrew Publishing, **2018**, pp. 331–374.

[52] S. Gai, C. Li, P. Yang, J. Lin, *Chemical Reviews* **2014**, *114*, 2343–2389.

[53] J. Żmojda, P. Miluski, A. Baranowska, R. Szal, M. Kochanowicz, *Photonics Letters of Poland* **2017**, *9*, 107.

[54] A. Beeby, S. Faulkner, D. Parker, J. A. G. Williams, *J. Chem. Soc., Perkin Trans. 2* **2001**, 1268–1273.

[55] H. Pham, L. W. Miller in *Rare-Earth Element Biochemistry: Characterization and Applications of Lanthanide-Binding Biomolecules*, (Ed.: J. A. Cotruvo), Methods in Enzymology, Academic Press, **2021**, pp. 291–311.

[56] J. A. Deluca, *Journal of Chemical Education* **1980**, *57*, 541.

[57] A. Ito, T. J. Meyer, *Phys. Chem. Chem. Phys.* **2012**, *14*, 13731–13745.

[58] C. Ash, M. Dubec, K. Donne, T. Bashford, *Lasers in Medical Science* **2017**, *32*, DOI `10.1007/s10103-017-2317-4`.

[59] R.D. Shannon, "Revised Effective Ionic Radii and Systematic Studies of Interatomic Distances in Halides and Chalcogenides", Acta Cryst. A32 751-767 (1976).

[60] A. Galstyan, S.-H. Messaddeq, I. Skripachev, T. Galstian, Y. Messaddeq, *Optical Materials Express* **2016**, *6*, 230.

[61] K. P. Piyachat Meejitpaisan, J. Kaewkhao, *Journal of Thai Interdisciplinary Research* **2019**, *14*, 54–59.

[62] G. Gao, A. Turshatov, I. Howard, D. Busko, R. E. Joseph, D. Hudry, B. Richards, *Advanced Sustainable Systems* **2017**, *1*, 1600033.

[63] A. De Pablos-Martín, A. Duran, M. Pascual, *International Materials Reviews* **2012**, *57*, 165–186.

[64] E. Brown, Z. D. Fleischman, J. McKay, M. Dubinskii, *Opt. Mater. Express* **2021**, *11*, 575–584.

[65] A. Gee, D. C. O'Shea, H. Z. Cummins, *Solid State Communications* **1966**, *4*, 43–46.

[66] *Journal of Luminescence* **2006**, *117*, 1–12.

[67] S. K. Saroj, P. Rawat, M. Gupta, G. Vijaya Prakash, R. Nagarajan, *European Journal of Inorganic Chemistry* **2018**, 4826–4833.

[68] M. Leblanc, V. Maisonneuve, A. Tressaud, *Chemical Reviews* **2015**, *115*, 1191–1254.

[69] O. Knop, T. Cameron, D. Adhikesavalu, B. Vincent, J. Jenkins, *Canadian Journal of Chemistry* **1986**, *65*, 1527–1556.

[70] J. A. J. Pardoe, A. J. Downs, *Chem. Rev.* **2007**, 2–45.

[71] R. L. Davidovich, P. P. Fedorov, A. I. Popov, *Reviews in Inorganic Chemistry* **2016**, *36*, 105–133.

[72] M. Gaudon, I. Andron, A. Demourgues, V. Rodriguez, A. Fargues, E. Durand, A. Chiron, C. Frayret, V. Jubera, *Mater. Adv.* **2022**, *3*, 7061–7071.

[73] R. Lösch, C. Hebecker, *Zeitschrift für Naturforschung B* **1979**, *34*, 1765–1766.

[74] F. He, E. Song, Y. Zhou, H. Ming, Z. Chen, J. Wu, P. Shao, X. Yang, Z. Xia, Q. Zhang, *Advanced Functional Materials* **2021**, *31*, 2103743.

[75] Y. Mei, W.-C. Zheng, L. Zhang, *Physica B: Condensed Matter* **2013**, *431*, 94–96.

[76] *Journal of Solid State Chemistry* **1987**, *71*, 109–114.

[77] D. de Viry, M. Casalboni, M. Palummo, N. Zema, *Solid State Commun.* **1990**, *76*, 1051–1054.

[78] A. Caramanian, J. Souron, P. Gredin, A. de Kozak, J. Derouet, B. Viana, *Journal of Luminescence* **2003**, *104*, 161–173.

[79] *Materials Letters* **1996**, *27*, 33–39.

[80] H. M., A. Guehria-Laïdoudi, J. Grannec, *GetInfo Platinfluoride 14 WorldwideSciences* **2006**, *2006-01-01*, DOI `10.1007/s10870-005-9003-2`.

[81] M. Kotecha, S. Chaudhuri, C. P. Grey, L. Frydman, *Journal of the American Chemical Society* **2005**, *127*, 16701–16712.

[82] D. W. Litchfield, D. G. Baird, *Rheology reviews* **2006**, *2006*, 1.

[83] P. P. Fedorov, A. A. Luginina, S. V. Kuznetsov, V. V. Osiko, *Journal of Fluorine Chemistry* **2011**, *132*, Special Issue: 2011 ACS Award Issue "For Creative Work in Fluorine Chemistry" Alain Tressaud, Part 2, 1012–1039.

[84] B. L. Cushing, V. L. Kolesnichenko, C. J. O'Connor, *Chemical Reviews* **2004**, *104*, 3893–3946.

[85] V. Kumar, A. Potdevin, P. Boutinaud, D. Boyer, *Materials Letters* **2020**, *261*, 127123.

[86] R. Wu, S. Zhang, Q. Zhang, C. Liu, J. Song, L. Hao, G. Tian, J. Lü, *Journal of Wuhan University of Technology-Mater. Sci. Ed.* **2019**, *34*, 558–562.

[87] J. Khan, H. Ullah, M. Sajjad, A. Bahadar, Z. Bhatti, F. Soomro, F. Hussain Memon, M. Iqbal, F. Rehman, K. Hussain Thebo, *Inorganic Chemistry Communications* **2021**, *130*, 108751.

[88] J. Li, Q. Wu, J. Wu in **2016**, pp. 295–328.

[89] M. Smida, J. Lhôste, M. Dammak, S. Garcia-Granda, *Arabian Journal of Chemistry* **2019**, *12*, 2519–2523.

[90] R. Hua, C. Zang, C. Shao, D. Xie, C. Shi, *Nanotechnology* **2003**, *14*, 588.

[91] M. A. Malik, M. Y. Wani, M. A. Hashim, *Arabian Journal of Chemistry* **2012**, *5*, 397–417.

[92] C. Xu, H. Luo, W. Liu, T. Ying, *Ceramics International* **2009**, *35*, 917–919.

[93] A. D. Lipchak, PhD thesis, **2019**.

[94] S. P. Thanh, F. Gaslain, M. Leblanc, V. Maisonneuve, *Journal of Fluorine Chemistry* **2000**, *101*, 161–163.

[95] P. Serna-Gallén, H. Beltrán-Mir, E. Cordoncillo, *Ultrasonics Sonochemistry* **2022**, *87*, 106059.

[96] R. Velmurugan, B. Krishnakumar, M. Swaminathan, *Materials Science in Semiconductor Processing* **2014**, *27*, 654–664.

[97] S. S. Low, M. Yew, C. N. Lim, W. S. Chai, L. E. Low, S. Manickam, B. T. Tey, P. L. Show, *Ultrasonics Sonochemistry* **2022**, *82*, 105887.

[98] A. Heuer-Jungemann, N. Feliu, I. Bakaimi, M. Hamaly, A. Alkilany, I. Chakraborty, A. Masood, M. F. Casula, A. Kostopoulou, E. Oh, K. Susumu, M. H. Stewart, I. L. Medintz, E. Stratakis, W. J. Parak, A. G. Kanaras, *Chemical Reviews* **2019**, *119*, 4819–4880.

[99] *Progress in Polymer Science* **2013**, *38*, Topical Issue on Polymer Hybrids, 1232–1261.

[100] S. Kilina, S. Ivanov, S. Tretiak, *Journal of the American Chemical Society* **2009**, *131*, 7717–7726.

[101] M. R. Dewi, G. Laufersky, T. Nann, *RSC Adv.* **2014**, *4*, 34217–34220.

[102] A. Caragheorgheopol, V. Chechik, *Phys. Chem. Chem. Phys.* **2008**, *10*, 5029–5041.

[103] C. Sun, J. R. J. Simke, M. Gradzielski, *Mater. Adv.* **2020**, *1*, 1602–1607.

[104] A. Dong, X. Ye, J. Chen, Y. Kang, T. Gordon, J. M. Kikkawa, C. B. Murray, *Journal of the American Chemical Society* **2011**, *133*, 998–1006.

[105] R. Sperling, W. Parak, *Philosophical transactions. Series A Mathematical physical and engineering sciences* **2010**, *368*, 1333–83.

[106] M. Kakihana, *Journal of Sol-Gel Science and Technology* **1996**, *6*, 7–55.

[107] A. Issa et al., *Polymers* **2019**, *11*, DOI `10.3390/polym11030537`.

[108] B. Wei, L. Li, L. Shao, J. Wang, *Materials* **2023**, *16*.

[109] W. Stöber et al., *Journal of Colloid and Interface Science* **1968**, *26*, 62–69.

[110] C.-Y. Qin, J.-H. Gao, X.-B. Xie, Zhai, *Chem. Synth.* **2023**, *3*, 29.

[111] P. Mélinon, S. Begin-Colin, J. L. Duvail, F. Gauffre, N. H. Boime, G. Ledoux, J. Plain, P. Reiss, F. Silly, B. Warot-Fonrose, *Physics Reports* **2014**, *543*, Engineered inorganic core/shell nanoparticles, 163–197.

[112] H. K. Drozdick, R. Weiss, C. M. Sullivan, S. Wieghold, L. Nienhaus, *Matter* **2022**, *5*, 1645–1669.

[113] G. H. Ahmed, J. Yin, O. M. Bakr, O. F. Mohammed, *ACS Energy Letters* **2021**, *6*, 1340–1357.

[114] F. Wang, R. Deng, X. Liu, *Nat. Protoc.* **2014**, *9*, 1634–1644.

[115] E. L. Rosen, R. Buonsanti, A. Llordes, A. M. Sawvel, D. J. Milliron, B. A. Helms, *Angewandte Chemie International Edition* **2012**, *51*, 684–689.

[116] J. Zuo, J. C. H. Spence, *MRS Bulletin* **2016**, *43*, 310.

[117] S. Amelinckx, J. Van Landuyt in *Encyclopedia of Physical Science and Technology (Third Edition)*, (Ed.: R. A. Meyers), Academic Press, New York, **2003**, pp. 53–87.

[118] S. Bonnamy, A. Oberlin in *Materials Science and Engineering of Carbon*, (Eds.: M. Inagaki, F. Kang), Butterworth-Heinemann, **2016**, pp. 45–70.

[119] 29-09-2023.

[120] N. Bajaj, R. Joshi in *Energy Materials*, Elsevier, **2021**, pp. 61–82.

[121] J. A. Kaduk et al., *Nature Reviews Methods Primers* **2021**, *1*, 608.

[122] 25-09-2023.

[123] C. Hammond, *The Basics of Crystallography and Diffraction*, Oxford University Press, **2015**.

[124] S. University, Class Lecture - Properties of X-rays.

[125] In *Basic Fundamentals of Drug Delivery*, (Ed.: R. K. Tekade), Advances in Pharmaceutical Product Development and Research, Academic Press, **2019**, pp. 369–400.

[126] N. Daéid in *Encyclopedia of Analytical Science (Second Edition)*, (Eds.: P. Worsfold, A. Townshend, C. Poole), Elsevier, Oxford, **2005**, pp. 471–480.

[127] A. GAVEZZOTTI in *Molecular Aggregation: Structure analysis and molecular simulation of crystals and liquids*, Oxford University Press, **2006**.

[128] M. Dramicanin, *Luminescence Thermometry Methods, Materials, and Applications*, 1st edition, **2017**.

[129] R. Anufriev, PhD thesis, **2013**.

[130] C. Schneider, W. Rasband, K. Eliceiri, *Nature Methods* **2012**, *9*, DOI `10.1038/nmeth.2089`.

[131] E. L. Rosen, R. Buonsanti, A. Llordes, A. M. Sawvel, D. J. Milliron, B. A. Helms, *Angewandte Chemie International Edition* **2012**, *51*, 684–689.

[132] A. Dong, X. Ye, J. Chen, Y. Kang, T. Gordon, J. M. Kikkawa, C. B. Murray, *Journal of the American Chemical Society* **2011**, *133*, 998–1006.

[133] D. L. Junze LI, Haizhen WANG, *Frontiers of Optoelectronics* **2020**, *13*, 225.

[134] F. Pan, J. Li, X. Ma, Y. Nie, B. Liu, H. Ye, *RSC Adv.* **2022**, *12*, 1035–1042.

[135] C. D. S. Brites, P. P. Lima, N. J. O. Silva, A. Millán, V. S. Amaral, F. Palacio, L. D. Carlos, *Nanoscale* **2012**, *4*, 4799–4829.

[136] S. Li, J. Luo, J. Liu, J. Tang, *The Journal of Physical Chemistry Letters* **2019**, *10*, 1999–2007.

[137] *Physica E: Low-dimensional Systems and Nanostructures* **2017**, *90*, 175–182.

[138] J. Weiner, F. Nunes, *Light-Matter Interaction. Physics and Engineering at the Nanoscale*, 2nd edition, Oxford U. Press, **2017**.

[139] W. Piotrowski, R. Marin, M. Szymczak, E. Martín Rodríguez, D. Ortgies, P. Rodríguez, M. Dramicanin, D. Jaque, L. Marciniak, *Advanced Optical Materials* **2022**, *11*, DOI `10.1002/adom.202202366`.

[140] Q. Akkerman, PhD thesis, **2019**.

[141] Y. Kayanuma, *Phys. Rev. B* **1988**, *38*, 9797–9805.

[142] P. J. Havel, *Diabetes Educ.* **2004**, *Suppl*, 2–14.

[143] J. Mohan, P. .G, K. Chennazhi, R. Jayakumar, S. Nair, *Journal of Experimental Nanoscience - J EXP NANOSCI* **2013**, *8*, 32–45.

[144] S. Fischer, R. D. Mehlenbacher, A. Lay, C. Siefe, A. P. Alivisatos, J. A. Dionne, *Nano Letters* **2019**, *19*, 3878–3885.

[145] K. Lunstroot, L. Baeten, P. Nockemann, J. Martens, P. Verlooy, X. Ye, C. Görller-Walrand, K. Binnemans, K. Driesen, *The Journal of Physical Chemistry C* **2009**, *113*, 13532–13538.

[146] J. Liu, A. M. Kaczmarek, F. Artizzu, R. Van Deun, *ACS Photonics* **2019**, *6*, 659–666.

[147] S. Hao, G. Chen, C. Yang, *Theranostics* **2013**, *3(5)*, 331–345.

[148] J.-H. Lee, K. K. Cho, J. R. Lee, J. C. Park, H. Jang, B. K. Cho, T.-W. Kim, *Crystal Growth & Design* **2021**, *21*, 1406–1412.

4.1 Appendix

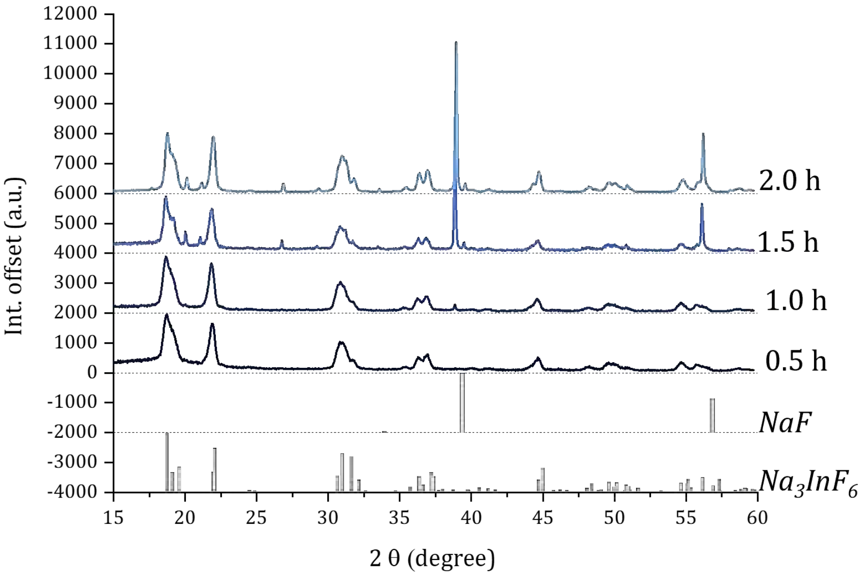

Figure 4.1: XRD patterns of samples obtained at 270 °C after 30 min, 60 min, 90 min and 120 min.

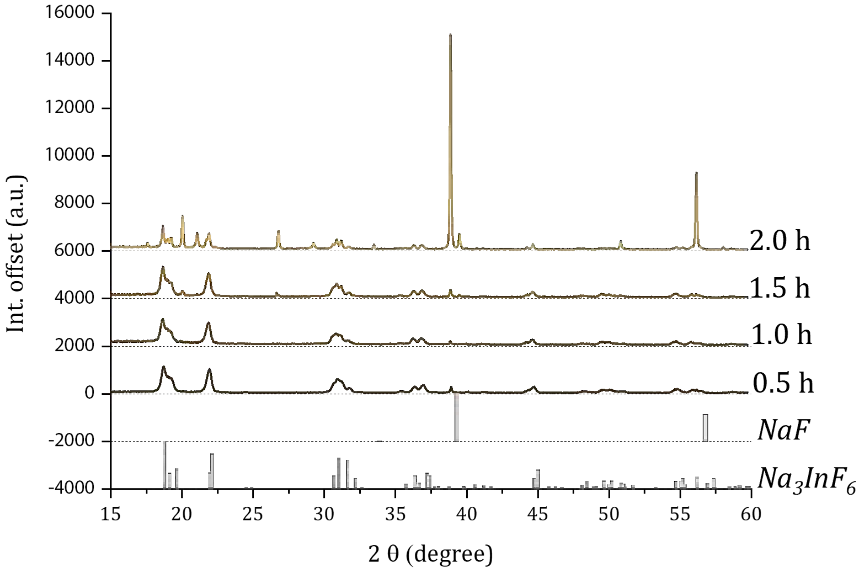

Figure 4.2: XRD patterns of samples obtained at 280 °C after 30 min, 60 min, 90 min and 120 min.

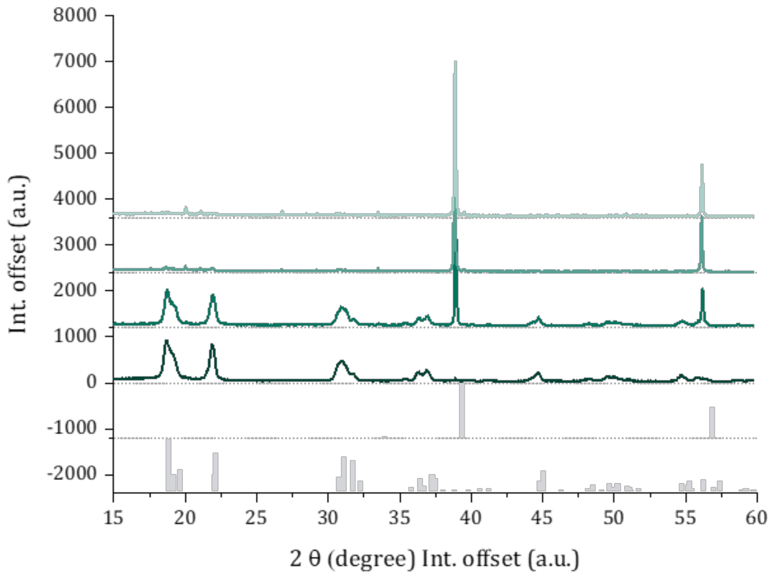

Figure 4.3: XRD patterns of samples obtained at 290 °C after 30 min, 60 min, 90 min and 120 min.

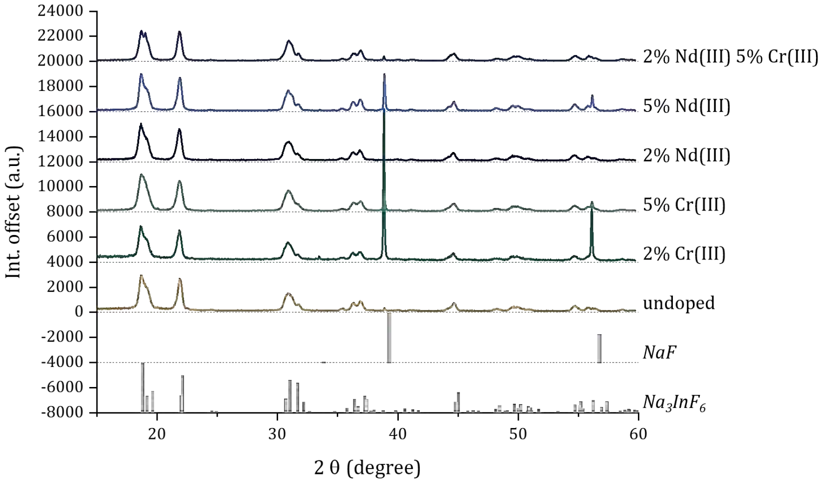

Figure 4.4: XRD pattern of undoped, doped and co-doped oleate-capped Na_3InF_6 NCs obtained with heating rate ∼ 7 °C/min, at 290 °C after 30 minutes of growth.